

# Biaxial nanomagnets as building block for balanced half-adders

Jonathan Maes

Student number: 01605865

Supervisors: Prof. dr. Bartel Van Waeyenberge, Dr. Jonathan Leliaert  
Counsellors: Pieter Gypens, Dr. Jonathan Leliaert

Master's dissertation submitted in order to obtain the academic degree of  
Master of Science in Engineering Physics

Academic year 2020-2021



# Biaxial nanomagnets as building block for balanced half-adders

Jonathan Maes

Student number: 01605865

Supervisors: Prof. dr. Bartel Van Waeyenberge, Dr. Jonathan Leliaert  
Counsellors: Pieter Gypens, Dr. Jonathan Leliaert

Master's dissertation submitted in order to obtain the academic degree of  
Master of Science in Engineering Physics

Academic year 2020-2021

The author(s) gives (give) permission to make this master dissertation available for consultation and to copy parts of this master dissertation for personal use. In all cases of other use, the copyright terms have to be respected, in particular with regard to the obligation to state explicitly the source when quoting results from this master dissertation.

## **Acknowledgements**

I would like to thank dr. Jonathan Leliaert and Pieter Gypens, as well as prof. dr. Bartel Van Waeyenberge, for their regular suggestions and supervision, which was indispensable to achieve a sufficient understanding of nanomagnetic logic.

# Biaxial nanomagnets as building block for balanced half-adders

Jonathan Maes

Supervisor(s): Pieter Gypens, Jonathan Leliaert, Bartel Van Waeyenbergh

## Abstract

Nanomagnetic logic makes use of magnetostatic interactions to implement logic gates. These logic gates are constructed by placing several nanomagnetic islands in close vicinity. The magnetization direction of a single island can be used to represent information. Nanomagnetic islands with biaxial anisotropy have four stable directions, such that each island can represent exactly two bits. This allows for a higher integration density compared to uniaxial islands, which have two stable directions and therefore can only represent one bit. Since each nanomagnet influences every other nanomagnet, and vice versa, there exists a two-way flow of information between the input and output. This allows for reverse calculations, but only if the ground states of all possible inputs have equal energy, in which case the gate is termed ‘balanced’.

First, the anisotropy of a specific biaxial geometry consisting of two ellipses was examined. It was found that the energy barrier between the easy axes depends on the eccentricity of these ellipses. The thermal switching accompanying a given energy barrier was found to have an attempt frequency  $f_0 \approx 10^{10} \text{ s}^{-1}$ , though this does not agree with theory.

A balanced biaxial chain is proposed, which can be used to transmit biaxial information between different logic gates. A way to convert biaxial information into uniaxial bits is proposed.

A geometry is proposed which can function as a half adder in a forward calculation. It consists of two free islands aligned along their easy axes, and one fixed island to break the symmetry and to realize the correct quaternary half adder truth table. A forward calculation with multiple half adders is possible with this geometry. For this geometry, there is a correct state with higher energy than an incorrect state, though these states correspond to different input values such that this does not matter for a forward calculation. It does, however, prevent a reverse calculation. A slightly different geometry is then proposed for which all the correct states have lower energy than any of the incorrect states. To chain multiple gates together for a larger reverse calculation, the gate must be perfectly balanced, which is not fulfilled for these geometries and remains a challenge for future work.

Keywords: biaxial nanomagnets, nanomagnetic logic, half adder, balanced logic gates



# Biaxial nanomagnets as building block for balanced half-adders

Jonathan Maes

Supervisor(s): Pieter Gypens, Jonathan Leliaert, Bartel Van Waeyenbergh

**Abstract**—Nanomagnetic logic implements logic gates through magnetostatic interactions between closely spaced single-domain nanomagnets. A biaxial nanomagnet has four stable magnetization directions, and can therefore represent two bits of information. Because a half adder takes two bits as input and yields two bits as output, a half adder can naturally be implemented using biaxial nanomagnets. Since each nanomagnet influences every other nanomagnet, and vice versa, there exists a two-way flow of information between in- and output. This allows for reverse calculations, but only if the ground states of all possible inputs have equal energy, in which case the gate is termed ‘balanced’. Here, a geometry is proposed which can function as a half adder in a forward calculation, consisting of two free biaxial islands aligned along their easy axes, and one fixed bias-island to break the symmetry and to realize the correct logical behavior. A slight modification to this geometry allows for a single reverse step, but makes it less suitable for forward calculation.

**Keywords**—biaxial nanomagnets, nanomagnetic logic, half adder, balanced logic gates

## I. INTRODUCTION

INSIDE a ferromagnetic material, the magnetic moments of neighboring atoms prefer a parallel alignment. As such, a lithographically etched ferromagnetic island of small size, on the order of a hundred nanometers, will have a nearly uniform magnetization, close to saturation [1–3], but with small deviations from this uniformity to accommodate for the geometry of the island. For a given geometry, the magnetization will prefer to align itself along the longest axis of the geometry, then called the easy axis. By choosing a thin geometry with four-fold rotational symmetry, the island can be made to exhibit biaxial shape anisotropy, hence creating two easy axes. As such, the magnetization prefers to point along any of four in-plane directions, allowing the island to represent exactly two bits of information. These nanomagnetic islands can then be used to create a digital logic circuit, which is called nanomagnetic logic (NML). This computing architecture propagates information through dipolar field coupling between the magnetization of closely spaced nanomagnets [4]. NML can be used to perform forward logic operations, which propagate information from an input to an output, much like traditional digital logic technologies. Such traditional architectures, however, use field-effect transistors to control the flow of electrons, which only allows information to flow in one direction. In NML, all islands influence each other, such that there is a two-way flow of information. This allows a fundamentally different way of thinking about logic [5], provided by ‘terminal-agnostic’ logic [6]. A terminal-agnostic gate is able to self-organize into its logically correct states, such that it does not matter whether the information is fed at what would traditionally be considered the input or output. To achieve this

using NML, one has to make use of ‘balanced’ gates. These are gates for which the ground states corresponding to all possible inputs have equal energy [7]. A necessary condition for a gate to be balanced, is that the number of distinguished configurations with minimum energy is equal to the number of input combinations the gate handles [8]. If this condition is fulfilled, all logically correct states will occur with equal probability. Conversely, when applying the desired output, all the correct inputs which should yield that output will be equally likely to occur, thus allowing reversible logic operations. There have been examples in literature where majority logic gates and balanced NAND gates have been created using uniaxial nanomagnets [7].

NML is also promising for its extremely low energy dissipation per operation [2, 4, 9]. By using biaxial nanomagnets, smaller logic gates can be created due to the increased integration density as compared to uniaxial islands. It can also be necessary to include chains of nanomagnets, to propagate the information between different gates in a circuit. Biaxial chains are possible, but in order to couple multiple half adders together in a useful manner, also uniaxial chains are required to separate the two bits represented by a biaxial island [7, 10–12].

Our goal here is to realize a nanomagnetic half adder. Because a half adder takes two input bits and yields two output bits, it can be advantageous to use biaxial nanomagnets for this purpose.

## II. MICROMAGNETIC THEORY

A theoretical framework suitable for investigating nanomagnetic logic is provided by the micromagnetic theory. In this formalism, instead of considering all individual atomic magnetic moments, the magnetization is represented by the continuous magnetization field  $\mathbf{M}(\mathbf{r})$ . This is the magnetic moment per unit volume, averaged over a small region of space. Its norm is the saturation magnetization  $M_{\text{sat}}$  of the material. This continuum approximation is only applicable locally in ferromagnets, over scales smaller than the exchange length  $\lambda$ . The time evolution of the magnetization is described by the Landau-Lifshitz equation [13], which states that the magnetization  $\mathbf{m}$  precesses around the effective field  $\mathbf{H}_{\text{eff}}$  while simultaneously being damped toward this effective field. The strength of this damping is determined by the damping constant  $\alpha$ .

This theory can be discretized and solved using a finite difference approach, with cell sizes on the order of  $\lambda$ , allowing efficient calculation of nanomagnetic problems. Here, the GPU-accelerated mumax<sup>3</sup> software is used [14]. It calculates the space-and time-dependent magnetization dynamics in nano- to micro-sized ferromagnets, which is well suited for the problems considered here.

J. Maes is a student in the 2<sup>nd</sup> year of the Master of Science in Engineering Physics (2020-2021), Ghent University (UGent), Ghent, Belgium. E-mail: Jonathan.Maes@UGent.be.



Fig. 1

TYPICAL GEOMETRY OF THE BIAXIAL ISLAND, THE UNION OF TWO PERPENDICULAR ELLIPSES.

### III. BIAXIAL ISLAND

Before considering half adders, we must first examine the characteristics of the biaxial nanomagnets themselves. The energy barrier is one of the main factors influencing the thermal switching between stable states, and is mainly determined by the shape of the island. Here, we consider the geometry shown in Fig. 1, which is the union of two identical perpendicular ellipses. This was chosen because it should be reasonably easy to manufacture due to the lack of sharp corners.

This geometry is uniquely defined by the length of the long and short axes of the ellipse. The *roundness*  $\rho$  is defined as the ratio of the short over the long axis, and the overall *size*  $L$  as the length of the long axis. For example, the geometry in Fig. 1 corresponds to  $(\rho, L) = (0.55, 100 \text{ nm})$ . The angle  $0^\circ$  is defined as the direction pointing to the right, with positive angles corresponding to the anticlockwise direction. Furthermore, the in-plane angles of several quantities will be used:  $\Theta$  denotes the instantaneous average magnetization angle, and its counterpart  $\tilde{\Theta}$  the magnetization angle after relaxation to a local energy minimum. The angle of an external bias field is denoted by  $\chi$ , while its counterpart  $\tilde{\chi}$  indicates a probing field.

#### A. Energy barrier

All of  $E(\tilde{\Theta} = n45^\circ), n \in \mathbb{Z}$  are equilibria, due to the symmetry of the geometry. Of these, 4 are energy minima, and 4 are maxima. The energy difference between these minima and maxima is the *energy barrier* between stable states. To determine the energy barrier, the energy landscape  $E(\tilde{\Theta})$  is calculated. For an accurate calculation, one has to allow the magnetization to relax, i.e. to settle itself to the geometry. This is mainly because, for a perfectly uniform magnetization, all magnetization angles have equal energy, resulting in a flat energy landscape, from which the energy barrier can not be determined. To prevent the magnetization from relaxing all the way to an anisotropic energy minimum, a probing field is applied at the desired angle. The Zeeman energy term due to the probing field is then subtracted, to reveal the energy landscape of a single biaxial island. This energy landscape is shown for  $\rho = 0.65$  in Fig. 2 (top), for various probing field magnitudes. For very high magnitudes, the energy landscape is nearly flat, because for such high fields the magnetization is nearly uniform. The relaxation towards the energy minimum (which the probing field should prevent) is clearest

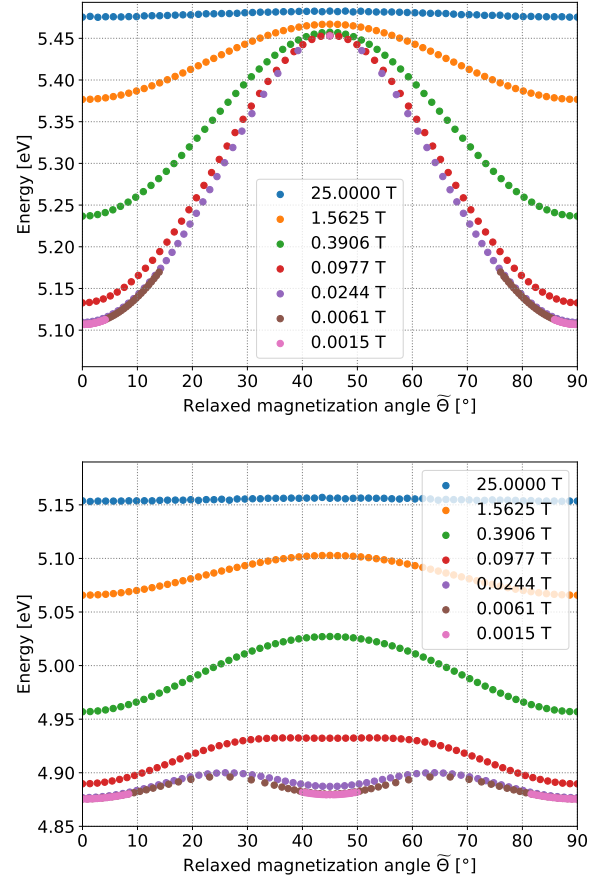


Fig. 2

ENERGY LANDSCAPE FOR VARIOUS PROBING FIELD MAGNITUDES, AS LISTED IN THE LEGEND.  $\tilde{\chi}$  IS VARIED UNIFORMLY IN 64 STEPS FROM  $0^\circ$  TO  $90^\circ$ . THE HORIZONTAL AXIS DENOTES THE AVERAGE MAGNETIZATION ANGLE  $\tilde{\Theta}$  AFTER RELAXATION. **TOP:**  $\rho = 0.65$ . **BOTTOM:**  $\rho = 0.49$ .

for low field magnitudes. Note that, even for very small fields, the energy maximum at  $\tilde{\Theta} = 45^\circ$  is stable, such that the probing field is not strictly necessary if one is only interested in the energy barrier, rather than the whole energy landscape.

The energy barrier  $E_{\text{barrier}}$  strongly depends on the roundness, as shown in Fig. 3. It is observed that, for large  $\rho$ , the easy axes are the long axes of the ellipses, while the hard axes are the diagonals in between them. For  $\rho < 0.48$ , the opposite is true. This is understood by looking at the detailed magnetization profile for both large and small  $\rho$ , shown in Fig. 4. For small  $\rho$ , the geometry consists of four elongated arms. In each of these arms, the magnetization prefers to be aligned along the length of that arm. The combination of those horizontal and vertical magnetizations, with a domain wall in the center, is on average diagonal, such that it appears as if the easy axes are diagonal. This is no longer a single-domain nanomagnet, so care must be taken when using low- $\rho$  islands, as the magnetization can differ significantly between the arms.

In between the regimes of small and large  $\rho$ , the energy barrier is very low, and for  $\rho \approx 0.49$  the energy difference



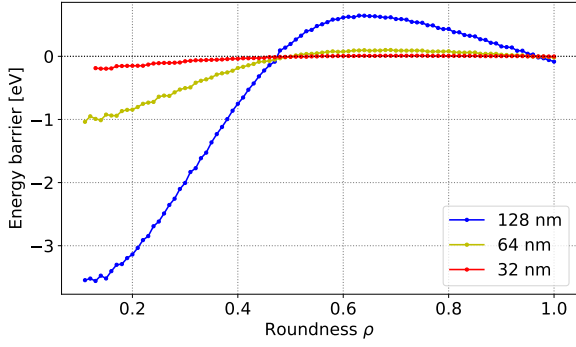


Fig. 3

ENERGY BARRIER AS A FUNCTION OF ROUNDNESS  $\rho$ , FOR DIFFERENT TOTAL SIZES  $L$  AS LISTED IN THE LEGEND. A POSITIVE VALUE INDICATES THAT  $E(\Theta = 45^\circ) > E(\Theta = 0^\circ)$ , I.E. THE HARD AXES ARE DIAGONAL.

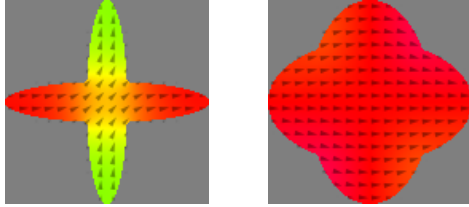


Fig. 4

RELAXED MAGNETIZATION FOR TWO DIFFERENT GEOMETRIES WITH  $L = 100$  nm. THE COLOR HUE AND THE ARROWS REPRESENT THE IN-PLANE MAGNETIZATION ANGLE. **LEFT:**  $\rho = 0.2$ . **RIGHT:**  $\rho = 0.6$ .

$\Delta E_{45^\circ-0^\circ} = E(\Theta = 45^\circ) - E(\Theta = 0^\circ)$  becomes zero. The energy landscape for  $\rho = 0.49$  is shown in Fig. 2 (bottom). Even though  $\Delta E_{45^\circ-0^\circ} = 0$ , the energy landscape is not entirely flat. Instead, there are now 8 local minima instead of 4, with a low energy barrier in between them all.

### B. Thermal switching

At nonzero temperatures, random thermal fluctuations can allow the magnetization to overcome the energy barrier and switch between stable states. Due to the thermal nature of this process, the magnetization reorientation rate is assumed to follow an Arrhenius form [15]. The thermal switching can then be modeled as driven by a jump-noise process [16]. As such, in the regime where  $E_{\text{barrier}} \gg k_B T$ , the time  $t_i$  between two consecutive switches is given by

$$t_i = -\frac{1}{f_0} \exp\left(\frac{E_{\text{barrier}}}{k_B T}\right) \ln(1 - P_i), \quad (1)$$

with  $P_i$  a uniformly distributed random number between 0 and 1. A theoretical equation [14, 17, 18] for  $f_0$  (in  $\text{rad s}^{-1}$ ) is given by

$$f_0 = \gamma \frac{\alpha}{1 + \alpha^2} \frac{2}{M_{\text{sat}} V} \sqrt{\frac{E_{\text{barrier}}^3}{\pi k_B T}}, \quad (2)$$

with  $\gamma$  the gyromagnetic ratio,  $M_{\text{sat}}$  the saturation magnetization, and  $\alpha$  the damping constant. For a biaxial island with

TABLE I

VALUES OF THE ATTEMPT FREQUENCY  $f_0$  FOR DIFFERENT ENERGY BARRIERS AND TEMPERATURES.  $M_{\text{sat}} = 8 \times 10^5 \text{ A m}^{-1}$  AND  $\alpha = 0.01$  FOR ALL ENTRIES.

Barrier [meV]	T [K]	$t_{\text{max}}$ [ns]	$N$	$f_0 [\text{s}^{-1}]$
27.8 <sup>a</sup>	300	100	37	$1.50 \times 10^9$
154.7	273	1000	13	$1.29 \times 10^{10}$
154.7	300	1000	11	$6.05 \times 10^9$
154.7	350	1000	41	$9.60 \times 10^9$
207.9	350	1000	9	$1.23 \times 10^{10}$
240.7	350	1000	5	$2.03 \times 10^{10}$

<sup>a</sup> This energy barrier is comparable to the thermal energy  $k_B T$ . Hence, the switching rate ( $\approx 2$  ns) is on the same timescale as the LLG dynamics, which causes the estimate for  $f_0$  using Eq. (2) to be inaccurate.

$E_{\text{barrier}} = 154.7 \text{ meV}$ , volume  $V \approx 4 \times 10^{-23} \text{ m}^3$ ,  $M_{\text{sat}} = 8 \times 10^5 \text{ A m}^{-1}$  and  $\alpha = 0.01$ , at  $T = 300 \text{ K}$ , this yields  $f_0 = 6 \times 10^5 \text{ s}^{-1}$ .

One can also estimate  $f_0$  by rewriting Eq. (1), given  $N$  switches during a time interval  $t_{\text{max}}$ :

$$f_0 = \frac{N \ln(4)}{t_{\text{max}}} \exp\left(\frac{E_{\text{barrier}}}{k_B T}\right). \quad (3)$$

Simulations were carried out for various temperatures and energy barriers, the results of which are given in Table I. The values for  $N$  were obtained by counting every monotone rotation of the magnetization over an angle greater than  $90^\circ$  as a single switch. These values are on the order of  $f_0 = 10^{10} \text{ s}^{-1}$ , which does not agree with the theoretical value. It is hypothesized that this is because the magnetization of the islands is not perfectly uniform, which is one of the assumptions underlying the theoretical equation. The values obtained through simulations are, however, on the same order of magnitude as the resonance frequency of the magnetization in a local energy minimum of the energy landscape from Fig. 2. The oscillation in this energy minimum can be interpreted as an attempt to switch to another stable state, once every half-period.

## IV. HALF ADDER

A half adder is a logic gate which adds two binary input bits, and therefore yields two bits as output. The truth table of a binary half adder is given in the left half of Table II. Since both input and output are represented by two bits, they can also each be represented by a biaxial island, because a single biaxial is-

TABLE II

TRUTH TABLE FOR A HALF ADDER, BOTH IN BINARY AND QUATERNARY NUMERAL SYSTEMS.

Binary		Quaternary	
Input	Output	Input	Output
00	00	0	0
01	01	1	1
10	01	2	1
11	10	3	2

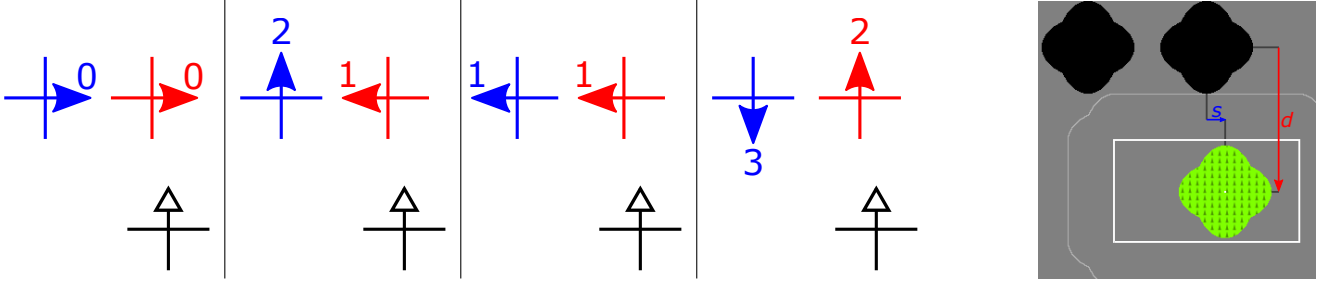


Fig. 5

**LEFT:** LOWEST ENERGY CONFIGURATIONS FOR ALL FOUR POSSIBLE INPUT MAGNETIZATIONS. THIS FUNCTIONS AS A HALF ADDER WITH QUATERNARY CONVENTION  $(0, 2, 1, 3)$ . ISLANDS WITH A FILLED ARROWHEAD CAN MOVE THEIR MAGNETIZATION FREELY TO ACHIEVE THE LOWEST ENERGY. ISLANDS WITH AN OPEN ARROWHEAD HAVE THEIR MAGNETIZATION PERMANENTLY FIXED IN THE DIRECTION OF THE ARROW. THE BLUE ISLAND IS THE INPUT ISLAND, THE RED ISLAND FUNCTIONS AS THE OUTPUT. **RIGHT:** GEOMETRY TO SCALE, DEFINING THE QUANTITIES  $s$  AND  $d$ . THE WHITE RECTANGLE INDICATES THE RANGE IN FIG. 6.

land has 4 stable states and can thus represent exactly two bits of information. As such, a half adder realized with biaxial nanomagnets only has one input island and one output island. The truth table of a half adder represented in the quaternary numeral system inherent to biaxial nanomagnets is given in the right half of Table II.

#### A. Nanomagnetic half adders

When designing a nanomagnetic logic gate, one has to define the meaning of each stable magnetization direction. For biaxial nanomagnets, there are four such directions, which have to be assigned a number from 0 to 3. There are 24 possible ways to do this. We will refer to such a choice as the ‘*quaternary convention*’, and will always list the quaternary convention in the form  $(0^\circ, 90^\circ, 180^\circ, 270^\circ)$ , for the island geometry from Fig. 1. A given geometry of nanomagnets, with given input and output islands, will only behave as a half adder for at most one quaternary convention. When choosing a different input or output island, the relevant quaternary convention may be different, or nonexistent. Thus, given a geometry with  $N$  free islands, one can try  $N$  choices for the input island,  $N - 1$  for the output, and 24 possible quaternary conventions (if one uses the same convention for input and output). Only a select few, if any, of these  $24N(N - 1)$  choices will yield the logically correct behavior of a half adder.

A given geometry can work as a half adder in a forward calculation if there exists such a choice where, for each of the 4 possible input magnetization angles, the lowest energy state has the logically correct output magnetization angle.

Also, note that in any NML system it is necessary to include at least one island whose magnetization direction is permanently fixed, in order to break the symmetry. This is because a nanomagnetic system is invariant under a global magnetization reversal [7]. Such fixation can for example be realized using exchange bias [19–21].

#### B. Gate design

A schematic representation of the half adder proposed here is shown in Fig. 5, where the ground states for all four possible

input magnetization directions are shown. The reasoning behind this geometry is as follows.

From the truth table of the half adder, it can be noted that there must be two inputs for which input and output are equal:  $0 \rightarrow 0$  and  $1 \rightarrow 1$ . This condition is readily fulfilled for two biaxial islands aligned along their easy axes in a ‘++’ geometry. The lowest energy state of such a geometry has both islands with a parallel magnetization along their common axis ( $\rightarrow\rightarrow$  or  $\leftarrow\leftarrow$ ). The anti-parallel configuration perpendicular to the common axis ( $\uparrow\downarrow$  or  $\downarrow\uparrow$ ) is another equilibrium with slightly higher energy, and is stable if the islands have a nonzero energy barrier.

As such, two of the four inputs are already mapped to a correct output, if one identifies the horizontal directions with 0 and 1 in the quaternary convention. Also  $3 \rightarrow 2$  is fulfilled, as this corresponds to the anti-parallel configuration if one identifies the vertical directions with 2 and 3. The only rule which is not yet fulfilled is  $2 \rightarrow 1$ , which then requires a vertical input to be mapped to a horizontal output. This can be fulfilled by adding a permanently fixed island, in the manner shown in Fig. 5, with its magnetization pointing towards the output island. Hence, this fixed island prevents the output island magnetization from pointing toward the fixed island. Hence, if one identifies the ‘up’ direction with the quaternary number 2, the output will have horizontal magnetization, and this horizontal direction is then identified with the number 1.

In order to assess the balancedness of the half adder, two metrics are introduced:  $B_1 = \min_\alpha(E_{\alpha,1}) - \max_\alpha(E_{\alpha,0})$  and  $B_2 = \max_\alpha(E_{\alpha,0}) - \min_\alpha(E_{\alpha,0})$ . Here,  $E_{\alpha,i}$  represents the  $i$ -th lowest energy level for which the input magnetization angle is near  $\alpha$ . The four ground states corresponding to the four possible inputs are hence represented by  $E_{\alpha,0}$ . The first metric  $B_1$  represents the energy difference between the highest ground state and the lowest first excited state. If the gate is to be used in a reverse calculation,  $B_1$  should at least be positive, because then, in thermal operation, the correct states will occur with higher probability than the incorrect states. The second metric  $B_2$  gives the energy difference between the highest and lowest of the 4 ground states, and is exactly zero for a perfectly balanced gate. If it is nonzero, one of the ground states is lower

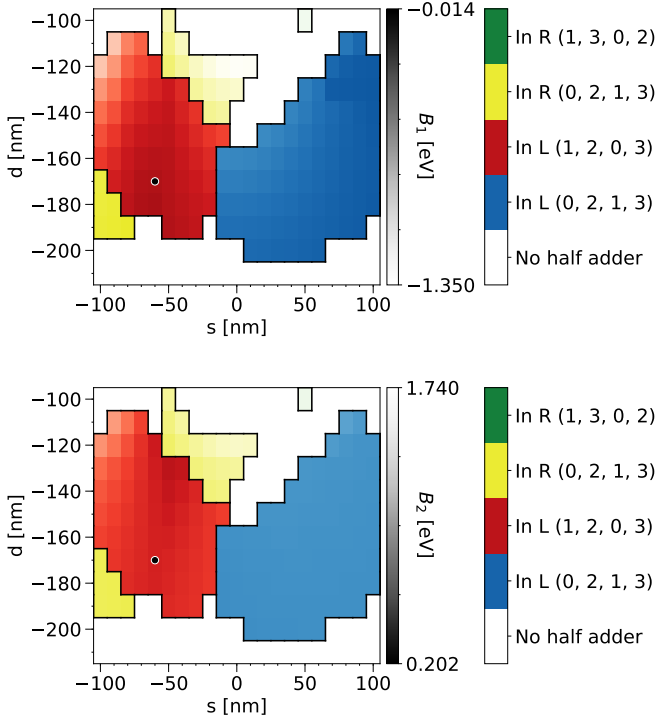


Fig. 6

REGIONS WHERE THE GEOMETRY FUNCTIONS AS A HALF ADDER, ACCORDING TO THE QUATERNARY CONVENTION INDICATED BY THE COLOR. THE BRIGHTNESS REPRESENTS THE BALANCEDNESS METRICS (DARKER IS BETTER). 'IN L' OR 'IN R' INDICATE THAT THE INPUT IS THE LEFTMOST OR RIGHTMOST FREE ISLAND, RESPECTIVELY. THE BLACK DOT INDICATES THE POSITION OF THE FIXED ISLAND FOR FIGS. 7 AND 8.

in energy than another, such that there is a chance that this particular logical state will be favored when multiple half adders are put in series. Hence, for a large forward calculation,  $B_2$  is preferably as small as possible.

### C. Varying fixed island position

We will now vary the position of the fixed island, to look for optimal values of  $B_1$  and  $B_2$ . This position is determined by the parameters  $s$  and  $d$ , as defined in the rightmost part of Fig. 5, where the range over which they were varied is represented by the white rectangle. The results of varying these parameters are shown in Fig. 6. It is observed that there are several regions where the geometry can be interpreted as a half adder. This interpretation is given by the quaternary convention, as indicated by the color. The brightness of these colors represents the balancedness metrics. In the blue region, the geometry functions as initially conceived, as was shown schematically in Fig. 5. The red and yellow regions overlap, because the yellow region is the mirrored counterpart of the red region over the  $s = -64$  nm axis. Unfortunately, the first metric  $B_1$  is negative everywhere in this range of  $s$  and  $d$ , preventing a reverse calculation. An example of the energy levels, grouped by input, is shown in Fig. 7 for  $d = -170$  nm and  $s = -60$  nm, which has one of the best, i.e. least negative, values for  $B_1$  in the examined range.

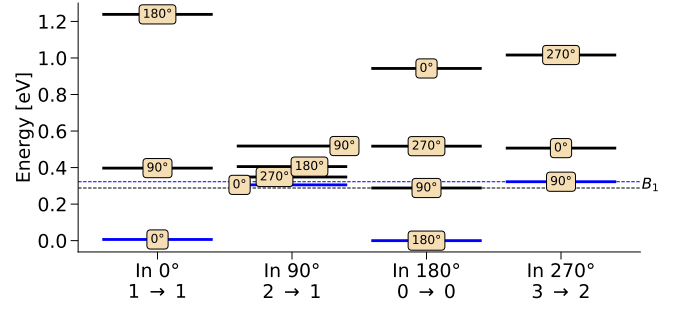


Fig. 7

ENERGIES OF DIFFERENT MAGNETIZATION CONFIGURATIONS, GROUPED BY INPUT MAGNETIZATION ANGLE, FOR  $d = -170$  nm AND  $s = -60$  nm. BLUE STATES ARE LOGICALLY CORRECT. THE TEXT BOX ON EACH ENERGY LEVEL SHOWS THE OUTPUT MAGNETIZATION ANGLE FOR THAT STATE.

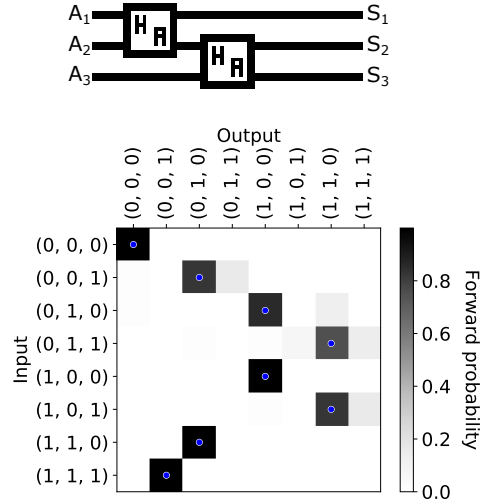


Fig. 8

**TOP:** SCHEMATIC REPRESENTATION OF THE LOGIC CIRCUIT. **BOTTOM:** PROBABILITY OF EACH OUTPUT, WHEN FIXING THE INPUT (I.E. FORWARD CALCULATION), AT 298 K. HENCE, EACH ROW ADDS UP TO A TOTAL OF 1.

BLUE DOTS INDICATE THE CORRECT OUTPUT. INPUTS ARE IN  $(A_1, A_2, A_3)$  FORMAT, OUTPUTS  $(S_1, S_2, S_3)$ .

The second metric shows how well-suited a certain choice of  $s$  and  $d$  is for forward calculation.  $B_2$  does not become exactly zero for this type of geometry. As such, only a limited number of half adders can be placed in a forward-calculating circuit.

An example of such a circuit is shown in Fig. 8 (top), where the half adders are represented in binary form. The bottom part of Fig. 8 shows the probability of each output for a forward calculation, i.e. when fixing the global input  $A_1$ ,  $A_2$  and  $A_3$ , at room temperature (298 K). It is observed that the logically correct output states are the most likely to occur. Some incorrect states also have nonzero probability, which can be explained with the energy levels from Fig. 7. For example, the energies for input 10 (quaternary 2) are closely spaced, which in this circuit

is the main cause of incorrect results with nonzero probability. An issue for larger circuits, is that the ground states for inputs 1 and 0 have significantly lower energy than for inputs 2 and 3. As such, it can be energetically favorable for a half adder inside a circuit to have input 1 or 0, which can yield incorrect results with appreciable probability.

There also exists a different range for  $s$  and  $d$  where  $B_1$  is positive, hence allowing at least one reverse calculation. This range has the fixed island closer to the common axis of the free islands, around  $(s, d) = (130 \text{ nm}, -50 \text{ nm})$ . Unfortunately, the values of  $B_2$  in this range are higher, thus making half adders in this range less suitable for forward calculation. Because in this case the fixed island is closer to the output island, it can also be more difficult to connect nanomagnetic wires to the input and output without significantly disturbing the system.

## V. CONCLUSION

Before considering half adders, the energy landscape of a single biaxial island was examined. It was noted that for a uniform magnetization, all in-plane magnetization angles have equal energy. The energy barrier depends significantly on the roundness  $\rho$  of the ellipses constituting the biaxial island. For large  $\rho$ , the easy axes are equal to the long axes of these ellipses. For small  $\rho$ , the easy and hard axes appear to be swapped, because the geometry more clearly consists of four perpendicular arms, which on average yield a diagonal magnetization. At  $\rho \approx 0.49$ , the energy difference between an average magnetization angle of  $0^\circ$  and  $45^\circ$  becomes zero. However, the energy landscape is not entirely flat; due to the relaxation along the edges of the geometry, there are 8 stable states instead of 4.

The thermal switching of different biaxial islands and for different temperatures and damping constants was also examined. No agreement between theoretical and simulated values for the attempt frequency  $f_0$  was found. It was hypothesized that this is because the magnetization of the islands is not perfectly uniform, which is one of the assumptions underlying the theory. The value obtained through simulations is approximately  $f_0 = 10^{10} \text{ s}^{-1}$ , which is on the same order of magnitude as the intrinsic resonance frequency of the magnetization in the local minima of the energy landscape.

Two similar half adder geometries were proposed, which can perform a forward calculation. One of these geometries has the fixed island far from the common axis, while for the second geometry the fixed island was placed near the common axis. The first geometry is more suitable for forward calculation, because its ground state energies are closer together than for the second geometry. It is not perfectly balanced, so the size of a forward calculating circuit is limited. The second geometry is less suitable for forward calculation, but can be used for a single reverse calculation, since all of its logically incorrect states have higher energy than any of the correct states.

## REFERENCES

- [1] D. Carlton, *Nanomagnetic Logic*, Ph.D. thesis, EECS Department, University of California, Berkeley, 2012.
- [2] R. P. Cowburn and M. E. Welland, "Room temperature magnetic quantum cellular automata," *Science*, vol. 287, pp. 1466–1468, 2000.
- [3] J. Leliaert, M. Dvornik, J. Mulders, J. De Clercq, M. V. Milošević, and B. Van Waeyenberge, "Fast micromagnetic simulations on GPU—recent advances made with mumax<sup>3</sup>," *Journal of Physics D: Applied Physics*, vol. 51, pp. 123002, 2018.
- [4] Z. Gu, M. E. Nowakowski, D. B. Carlton, R. Storz, M. Im, J. Hong, W. Chao, B. Lambson, P. Bennett, M. T. Alam, M. A. Marcus, A. Doran, A. Young, A. Scholl, P. Fischer, and J. Bokor, "Sub-nanosecond signal propagation in anisotropy-engineered nanomagnetic logic chains," *Nature Communications*, vol. 6, pp. 6466, 2015.
- [5] P. Gypens, J. Leliaert, M. Di Ventra, B. Van Waeyenberge, and D. Pinna, "Nanomagnetic self-organizing logic gates," 2020, arXiv:2012.12721.
- [6] F. L. Traversa and M. Di Ventra, "Polynomial-time solution of prime factorization and np-complete problems with digital memcomputing machines," *Chaos: An Interdisciplinary Journal of Nonlinear Science*, vol. 27, pp. 023107, 2017.
- [7] P. Gypens, J. Leliaert, and B. Van Waeyenberge, "Balanced magnetic logic gates in a kagome spin ice," *Physical Review Applied*, vol. 9, pp. 034004, 2018.
- [8] J. C. Lusth and B. Dixon, "A characterization of important algorithms for quantum-dot cellular automata," *Information Sciences*, vol. 113, pp. 193 – 204, 1999.
- [9] N. D'Souza, J. Atulasimha, and S. Bandyopadhyay, "Four-state nanomagnetic logic using multiferroics," *Journal of Physics D: Applied Physics*, vol. 44, pp. 265001, 2011.
- [10] A. Imre, G. Csaba, L. Ji, A. Orlov, G. H. Bernstein, and W. Porod, "Majority logic gate for magnetic quantum-dot cellular automata," *Science*, vol. 311, pp. 205–208, 2006.
- [11] N. D'Souza, A. Biswas, H. Ahmad, M. S. Fashami, M. M. Al-Rashid, V. Sampath, D. Bhattacharya, M. A. Abeed, J. Atulasimha, and S. Bandyopadhyay, "Energy-efficient switching of nanomagnets for computing: straintronics and other methodologies," *Nanotechnology*, vol. 29, pp. 442001, 2018.
- [12] N. D'Souza, J. Atulasimha, and S. Bandyopadhyay, "An ultrafast image recovery and recognition system implemented with nanomagnets possessing biaxial magnetocrystalline anisotropy," *IEEE Transactions on Nanotechnology*, vol. 11, pp. 896–901, 2012.
- [13] L. Landau and E. Lifshitz, "Theory of the dispersion of magnetic permeability in ferromagnetic bodies," *Physikalische Zeitschrift Sowjetunion*, vol. 8, pp. 153, 1935.
- [14] A. Vansteenkiste, J. Leliaert, M. Dvornik, M. Helsen, F. Garcia-Sanchez, and B. Van Waeyenberge, "The design and verification of Mumax3," *AIP Advances*, vol. 4, pp. 107133, 2014.
- [15] A. Farhan, P.M. Derlet, A. Kleibert, A. Balan, R.V. Chopdekar, M. Wyss, L. Anghinolfi, F. Nolting, and L. J. Heyderman, "Exploring hyper-cubic energy landscapes in thermally active finite artificial spin-ice systems," *Nature Physics*, vol. 9, pp. 375–382, 2013.
- [16] I. Mayergoyz, G. Bertotti, and C. Serpico, "Magnetization dynamics driven by a jump-noise process," *Physical Review B*, vol. 83, 2011.
- [17] J. Leliaert, J. Mulders, J. De Clercq, A. Coene, M. Dvornik, and B. Van Waeyenberge, "Adaptively time stepping the stochastic landaulifshitz-gilbert equation at nonzero temperature: Implementation and validation in mumax<sup>3</sup>," *AIP Advances*, vol. 7, pp. 125010, 2017.
- [18] L. Breth, D. Suess, C. Vogler, B. Bergmair, M. Fuger, R. Heer, and H. Brueckl, "Thermal switching field distribution of a single domain particle for field-dependent attempt frequency," *Journal of Applied Physics*, vol. 112, pp. 023903, 2012.
- [19] J. Nogués and I. K. Schuller, "Exchange bias," *Journal of Magnetism and Magnetic Materials*, vol. 192, pp. 203 – 232, 1999.
- [20] J. Nogués, J. Sort, V. Langlais, V. Skumryev, S. Suriñach, J.S. Muñoz, and M.D. Baró, "Exchange bias in nanostructures," *Physics Reports*, vol. 422, pp. 65 – 117, 2005.
- [21] R. L. Stamps, "Mechanisms for exchange bias," *Journal of Physics D: Applied Physics*, vol. 33, pp. R247–R268, 2000.

# Contents

<b>1</b>	<b>Introduction</b>	<b>1</b>
1.1	Nanomagnetic island . . . . .	2
1.2	Quantum Cellular Automata . . . . .	2
1.3	Nanomagnetic islands . . . . .	4
1.4	Signal Propagation . . . . .	6
1.5	Imaging the magnetization . . . . .	9
<b>2</b>	<b>Theoretical framework</b>	<b>13</b>
2.1	Energy contributions . . . . .	13
2.2	Magnetization dynamics . . . . .	16
<b>3</b>	<b>Biaxial nanomagnetic island</b>	<b>21</b>
3.1	Energy barrier . . . . .	22
3.2	Energy landscape . . . . .	24
3.3	Thermal switching . . . . .	29
<b>4</b>	<b>Interaction between two islands</b>	<b>35</b>
4.1	Interaction energy . . . . .	35
4.2	Distance dependence . . . . .	38
<b>5</b>	<b>Half adder</b>	<b>39</b>
5.1	Nanomagnetic half adders . . . . .	39
5.2	Gate design . . . . .	41
5.3	Simulation methods . . . . .	43
5.4	Varying fixed island parameters . . . . .	44
5.5	Additional considerations . . . . .	56
<b>6</b>	<b>Conclusion and outlook</b>	<b>59</b>
	<b>Bibliography</b>	<b>61</b>

## List of constants

Symbol	Name	Value
$k_B$	Boltzmann constant	$1.380\,649 \times 10^{-23} \text{ J K}^{-1}$
$\gamma$	Gyromagnetic ratio	$1.7595 \times 10^{11} \text{ rad T}^{-1} \text{ s}^{-1}$
$\gamma_0$	$\mu_0 \gamma$	$2.2111 \times 10^5 \text{ m A}^{-1} \text{ s}^{-1}$
$\mu_0$	Vacuum permeability	$4\pi 10^{-7} \text{ T m A}^{-1}$

## List of abbreviations

Abbreviation	Full name
AFM	Anti-ferromagnetic
BCC	Body-centered cubic
CMOS	Complementary metal-oxide-semiconductor
EQCA	Electronic quantum cellular automata
FCC	Face-centered cubic
FD	Finite difference
FM	Ferromagnetic
FSAL	First-same-as-last
GPU	Graphics processing unit
LL	Landau-Lifshitz
LLG	Landau-Lifshitz-Gilbert
MFM	Magnetic force microscopy
MOKE	Magneto-optical Kerr effect
MQCA	Magnetic quantum cellular automata
MTJ	Magnetic tunnel junction
MTXM	Magnetic transmission X-ray microscopy
NML	Nanomagnetic logic
PEEM	Photoelectron emission microscopy
QCA	Quantum cellular automata
XMCD	X-ray magnetic circular dichroism

## List of symbols

A bold symbol indicates a vector.

Symbol	Name	Unit
<b>a</b>	Unit vector	
$A_{\text{ex}}$	Exchange stiffness constant	$\text{J m}^{-1}$
$B_1$	First balancedness metric	J
$B_2$	Second balancedness metric	J

Symbol	Name	Unit
$\mathbf{B}$	Magnetic flux density	T
$\mathbf{B}_{\text{ext}}$	External bias field flux density	T
$\mathbf{B}_{\text{ext,p}}$	Probing field flux density	T
$d$	Distance between centers of two islands	m
$\mathbf{e}_i$	Unit vectors along the axes of cubic anisotropy	
$E$	Energy	J
$E_{\alpha,i}$	$i$ -th energy level for which the input magnetization angle is near $\alpha$	J
$E_{\text{anis}}$	Anisotropy energy	J
$E_{\text{barrier}}$	Energy barrier between stable states	J
$E_{\text{demag}}$	Demagnetization energy	J
$E_{\text{exch}}$	Exchange energy	J
$E_{\text{Zeeman}}$	Zeeman energy	J
$f_0$	Attempt frequency	Hz
$\mathbf{H}$	Magnetic field strength	A m <sup>-1</sup>
$\mathbf{H}_{\text{demag}}$	Demagnetizing field	A m <sup>-1</sup>
$\mathbf{H}_{\text{eff}}$	Effective field	A m <sup>-1</sup>
$\mathbf{H}_{\text{ex}}$	Exchange field	A m <sup>-1</sup>
$\mathbf{H}_{\text{ext}}$	External field	A m <sup>-1</sup>
$\mathbf{H}_{\text{therm}}$	Stochastic thermal field	A m <sup>-1</sup>
$I_{\text{XMCD}}$	Intensity of XMCD signal	W m <sup>-2</sup>
$J_{ij}$	Exchange integral for spins $i$ and $j$	J
$K_{\text{c1}}$	First order cubic anisotropy constant	J m <sup>-3</sup>
$K_{\text{c2}}$	Second order cubic anisotropy constant	J m <sup>-3</sup>
$K_{\text{u1}}$	First order uniaxial anisotropy constant	J m <sup>-3</sup>
$K_{\text{u2}}$	Second order uniaxial anisotropy constant	J m <sup>-3</sup>
$L$	Ellipse major axis	m
$\mathbf{m}$	Reduced magnetization $\mathbf{M}/M_{\text{sat}}$	
$\mathbf{m}_i$	Magnetic moment of atom $i$	A m <sup>2</sup>
$\mathbf{M}$	Magnetization	A m <sup>-1</sup>
$M_{\text{sat}}$	Saturation magnetization	A m <sup>-1</sup>
$\mathbf{n}_i$	Unit vector in the direction of $\mathbf{S}_i$	
$N$	Number of switches during a time interval $t_{\text{max}}$	
$P_i$	Uniformly distributed random number between 0 and 1	
$\mathbf{r}$	Position vector	m
$\mathbf{S}_i$	Spin of atom $i$	
$t$	Time	s
$t_i$	Time between thermal switch $i$ and $i + 1$	s
$t_{\text{max}}$	Total simulation time	s
$T$	Temperature	K
$T_{\text{C}}$	Curie temperature	K
$T_{\text{N}}$	Néel temperature	K

Symbol	Name	Unit
$\mathbf{u}$	Unit vector along the axis of uniaxial anisotropy	
$V$	Volume of single-domain particle	$\text{m}^3$
$\alpha$	Gilbert damping constant	
$\alpha'$	$\frac{\alpha\gamma_0}{1+\alpha^2}$	
$\gamma'_0$	$\frac{\gamma_0}{1+\alpha^2}$	$\text{rad m C}^{-1}$
$\Gamma$	Scattering rate in jump-noise process	$\text{s}^{-1}$
$\Delta t$	Time step of numerical update scheme	s
$\theta$	Inclination in spherical coordinates	rad
$\Theta_i$	Instantaneous magnetization angle in the horizontal plane of island $i$	rad
$\tilde{\Theta}_i$	Relaxed magnetization angle in the horizontal plane of island $i$	rad
$\lambda$	Exchange length	m
$\rho$	Ellipse roundness: ratio between major and minor axes	
$\sigma$	Photon spin	
$\mathfrak{z}$	Random vector from standard normal distribution	
$\phi$	Azimuth in spherical coordinates	rad
$\Phi_i$	Rotation of island $i$ geometry	rad
$\chi$	Angle of external bias field in the horizontal plane	rad
$\tilde{\chi}_i$	Angle of probing field in the horizontal plane for island $i$	rad
$\psi$	Vector potential	
$\Omega_i$	Geometry of ferromagnetic region $i$ in the finite-difference grid	



# 1 Introduction

The goal of this thesis is to design a nanomagnetic logic gate that can function as a half adder. This gate will be built from biaxial nanomagnets, whose dipolar interaction will ensure that the gate self-organizes into the logically correct states. Ideally, this gate should also be balanced, meaning that all its ground state energies are equal, such that a reverse calculation is possible. Let us first break down the different concepts underlying nanomagnetic logic from the ground up.

An atom may display what is called a **magnetic dipole moment**, on one hand due to the angular momentum of electrons around the nucleus, and on the other hand due to the intrinsic spin of the elementary particles which make up the atom. The magnetic moment can be defined using the torque the atom experiences in a magnetic field [1]. In a material, many atoms are together, and the macroscopic sum of all their magnetic moments is called the magnetization of the material.

Some materials display specific long-range order of the magnetic moments, like for example ferromagnetism where all individual magnetic moments of neighboring atoms try to align themselves in the same direction. As such, by fabricating a very small ferromagnetic island of several hundred nanometers, the island will have a nearly uniform magnetization. If this island has one or another form of anisotropy, be it due to the crystal structure or the shape of the island, the magnetization will have minimal energy if it lies along a certain axis, called the ‘*easy axis*’. **Shape anisotropy** originates from the observation that the magnetization preferably orients itself along the long axis of a microscopic structure. To make sure the magnetization lies in a single plane, the island is very thin, such that its shape is nearly two-dimensional. An example that is often used is a 2D ellipse, for which the easy axis is equal to the long axis of the ellipse. In general, if a structure has one easy axis (and thus two stable directions), we speak of uniaxial anisotropy. In the case of two easy axes (and thus four stable directions), as will be the main topic of this thesis, this is called **biaxial anisotropy**. Biaxial shape anisotropy can be achieved with a geometry that is invariant under rotation over  $90^\circ$ .

In the uniaxial case, there are two stable directions, which can be related to a ‘0’ or ‘1’ bit. Hence, these nanomagnetic islands can be used to create a **digital logic circuit**. Nanomagnetic logic (NML) computing architectures propagate binary information through dipolar field coupling between the magnetization of closely spaced nanoscale magnets [2]. This architecture is promising for its extremely low energy dissipation per operation [2, 3, 4]. One can use nanomagnetic logic to perform normal logic operations, which propagate information from an input to an output. However, this does not give NML an edge over CMOS-based technologies, as one still needs clocking to perform such logic operations.

A fundamentally different way of thinking about logic, which can give NML an edge over CMOS, is provided by ‘terminal-agnostic’ logic [5]. A terminal-agnostic gate is able to self-organize into its logically correct states, such that it does not matter whether the information is fed at what would traditionally be considered the input or output. A way of achieving this using NML, is by making use of ‘**balanced**’ gates. These are gates for which the ground states corresponding to all possible inputs have the same energy [6]. As such, at nonzero temperatures there is an equal chance that the gate is in any of the logically correct states, irrespective of

whether the information was fed at the traditional input or output [7]. Because of this, one can perform reversible logic operations, as by applying the desired output one can recover the corresponding input.

There have been examples in literature where majority logic gates and balanced NAND gates have been created using uniaxial nanomagnets [6].

Biaxial nanomagnets can be used to encode two bits in one island, because they have 4 stable magnetization directions. This allows for smaller logic gates due to the increased integration density as compared to uniaxial islands. The main goal of this thesis is to realize a half adder using biaxial nanomagnets. A half adder takes two bits as input and yields two bits as output, so it feels almost natural to design it using biaxial nanomagnets instead of uniaxial ones.

In the following sections, the nature of nanomagnetic islands, the concept of quantum cellular automata, signal propagation and techniques for imaging the magnetization will be explained in more detail.

## 1.1 Nanomagnetic island

A lithographically etched ferromagnetic island of small size, on the order of a hundred nanometers, will have a nearly uniform magnetization, with a magnitude equal to the saturation magnetization of the material [4, 8]. This uniform alignment is due to the quantum mechanical Heisenberg-Dirac exchange interaction [9, 10], which tends to align neighboring moments in the same direction. A competing effect is caused by the magnetostatic energy, which makes a uniform magnetization unfavorable on larger length scales. The combination of these two effects causes the magnetization of such a small ferromagnetic island to be nearly uniform, but with small deviations from this uniformity to accommodate for the geometry of the island.

By introducing anisotropy in the material, one or more axes can be made energetically favorable for the magnetization. This anisotropy can either be of magnetocrystalline origin, or due to the shape of the nanomagnet. Shape anisotropy can be realized by giving the nanomagnet an elongated shape, for example an ellipse instead of a perfect circle. In the uniaxial case, there is one stable magnetization axis, so the two directions ‘up’ and ‘down’ along this axis can be related to the bits ‘0’ and ‘1’ [4]. This is not to be confused with unidirectional anisotropy, which only has one stable magnetization direction, and can be achieved using exchange bias [11, 12, 13]. A lot of research has been conducted to use uniaxial anisotropy for computation, and logic gates and chains have been proposed, which use classical magnetostatic interactions to propagate the information [6, 14, 15]. The use of two favorable axes, i.e. biaxial anisotropy, allows for a higher logic density, as the four stable directions ‘up’, ‘down’, ‘right’ and ‘left’ can be related to ‘00’, ‘01’, ‘10’ and ‘11’ [16]. This can occur for cubic crystals, and can also be realized by choosing the geometry of the island such that it exhibits a four-fold rotational symmetry. An example of such a geometry, is the union of two perpendicular ellipses.

## 1.2 Quantum Cellular Automata

Traditional digital logic technologies like CMOS use field-effect transistors to control the flow of electrons. This kind of architecture fundamentally only allows information to flow in one direction. Other architectures allowing communication between the output and input in both

ways could allow certain types of computations to be executed faster. One approach to realize such an architecture are the Quantum Cellular Automata (QCA), which use quantum effects, in a broad sense, to make logic gates. A cellular automaton is a mathematical concept, proposed by Von Neumann [17], in which the universe is divided into a regular grid of cells, where each cell is influenced by its direct neighbors. The most famous example of such a mathematical cellular automaton is Conway’s Game of Life, which has been shown to be universal for computation, as any Turing machine can be encoded in it [18]. Apart from the universality in the Turing sense, cellular automata provide an additional benefit because they are able to process algorithms in a distributed manner due to their inherent spatial parallelism [18]. From a practical point of view, QCA can be orders of magnitude smaller and more energy efficient than traditional CMOS technology [4].

There are several possibilities to realize QCA, which can generally be classified as either electronic or magnetic QCA. Electronic QCA (EQCA) make use of the forces between electrons, while magnetic QCA (MQCA) leverage the magnetic moments of atoms. EQCA are “quantum” because they use quantum mechanical tunneling of charge between quantum dots, while MQCA are “quantum” because of the exchange interaction between individual atomic magnetic moments [4]. Apart from this quantum mechanical nature of the building blocks, QCA are essentially classical devices switching through either Coulombic or magnetic interactions [19]. What all these QCA have in common, is that their fundamental building blocks (electrons, magnetic moments...) influence each other in either direction, thus allowing the aforementioned two-way flow of information between what would traditionally be referred to as input and output. The MQCA are the main topic of this paper, but it is interesting to take a short look at EQCA as well, for both share some ideas and problems.

One specific implementation of EQCA makes use of square cells, each with four quantum dots at the vertices of a square, as shown in Fig. 1 (left). These quantum dots can accommodate an electron, and each square cell is made such that there are always two excess electrons present. It is then energetically favorable for these electrons to occupy two diagonally opposite quantum dots [20]. The two possible diagonal configurations are then the ‘0’ and ‘1’ states. An extensively studied logic gate using this architecture is the three-input majority logic gate, also shown in Fig. 1 (right). It consists of five cells arranged in a plus-shape, with three inputs and one output. Just like the familiar NAND gate, the majority gate is universal for computation [8].

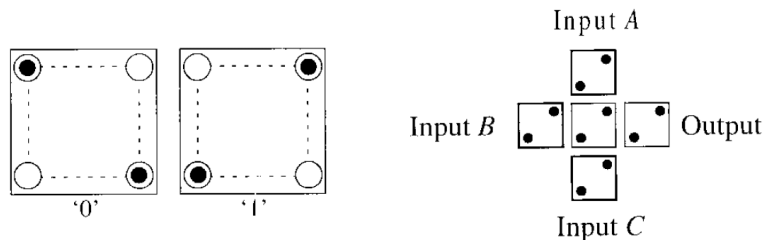


**Figure 1** – Implementation of EQCA using quantum dots arranged in square cells. **Left:** definition of ‘0’ and ‘1’ in this system. **Right:** majority logic gate in this system. Figure reproduced from [20].

By fixing one of the inputs to 0 or 1, the majority gate can realize an AND or an OR operation, respectively. A drawback of these EQCA is that they require low electron temperatures in order to work reliably, as otherwise thermal smearing of the charge states of the dots becomes an issue [20].

QCA compute by relaxing to a configuration of minimal energy [19]. It is important that all these relaxed configurations are equal in energy level. This is what is meant by ‘balanced’ QCA. A necessary condition for an automaton to be balanced is that the number of distinguished configurations with minimum energy is equal to the number of input combinations the automaton handles [19].

### 1.3 Nanomagnetic islands

As was mentioned before, the magnetization of a nanomagnetic island tends to align itself along the longest axis of a given geometry. This can intuitively be understood by thinking in terms of magnetic charges, as in Fig. 2. Because we are dealing with ferromagnetic materials and small geometries, the magnetization will be nearly uniform throughout the island. At places along the edge of the geometry, where the magnetization is pointing outward, a positive magnetic charge is placed, and vice versa for negative charges. The most favorable magnetization angle is then the one which maximizes the distance between the magnetic charges. Another way of interpreting this, is that a minimal amount of magnetic charges is also preferred [21]. Where the magnetization is parallel to the edge, no magnetic charge is present. As such, the magnetization prefers to be parallel to the edges of a given geometry.

In the figure, this is the situation shown on the right. Both of the interpretations explain the tendency for ferromagnetic materials to be magnetized along the **long axis of a microscopic geometry**. In case of higher symmetry, for example with biaxial shape anisotropy, it is no longer as clear which symmetry axes will be the easy axes, and which the hard ones, as will be

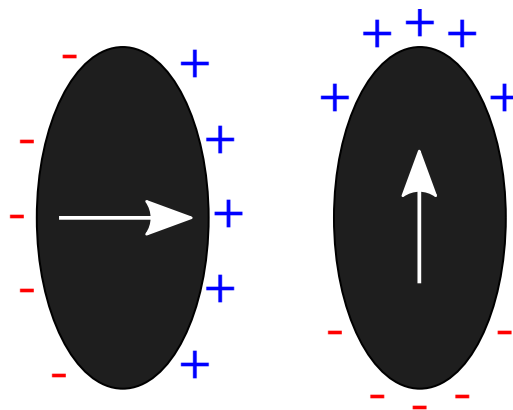


**Figure 2** – Illustration of magnetic charges for two uniform magnetization directions, explaining the tendency for ferromagnetic materials to be magnetized along the long axis of a microscopic geometric structure. **Left:** magnetization along the short axis; highest energy configuration. **Right:** magnetization along the long axis; lowest energy configuration.

examined in more detail in Section 3.

When constructing a logic gate, it can be useful to include islands whose magnetization direction is permanently fixed, as opposed to the freely switching islands discussed before. One way to realize such a fixed island is through a phenomenon called ‘exchange bias’ [11, 12, 13, 22]. This phenomenon arises at the interface between an anti-ferromagnetic (AFM) and a ferromagnetic (FM) material as illustrated in Fig. 3.

An AFM material consists of magnetic moments which alternate direction in each atomic plane, while in a FM material all these moments point in the same direction. In the situation as illustrated in the figure, the top layer of the AFM material thus also wants the bottom layer of the FM material to align anti-parallel, while the FM layer on the contrary prefers a parallel alignment. One of these two competing effects will be stronger than the other, which oftentimes results in an anti-parallel alignment of the magnetic moments at the FM/AFM interface, as shown in the right hand side of Fig. 3. The AFM material is not affected by external fields, since it consists of alternating magnetic moments leading to a zero net magnetization. The AFM layer will thus remain fixed at temperatures below its Néel temperature  $T_N$ . One can define the fixation direction by choosing the materials such that  $T_N$  is lower than the Curie temperature  $T_C$  of the FM layer, and first operating at a temperature  $T$  for which  $T_N < T < T_C$ . In this regime, the FM layer will follow an applied magnetic field, while the AFM layer is paramagnetic due to the high temperature. When the temperature is then lowered below  $T_N$ , the AFM material will settle in such a way that its top layer is correctly aligned as to fix the FM layer [11].

At sufficiently strong fields, however, the FM layer will follow the external field anyway, though this will occur at significantly higher fields than for the case where there would be no AFM material. Thus, by manufacturing a FM island on top of an AFM material, the island can be made to have a single preferential direction, instead of a preferential axis.

In general, it will be required to fix different islands in different directions. This can not be achieved by heating the whole substrate and applying an external field, so one has to use a local heating process, for example a focused laser beam. By separately heating each island above  $T_N$  and allowing it to cool below  $T_N$  before heating the next island, one can still make use of an external field, synchronized with the heat source, to control the orientation of each fixed island

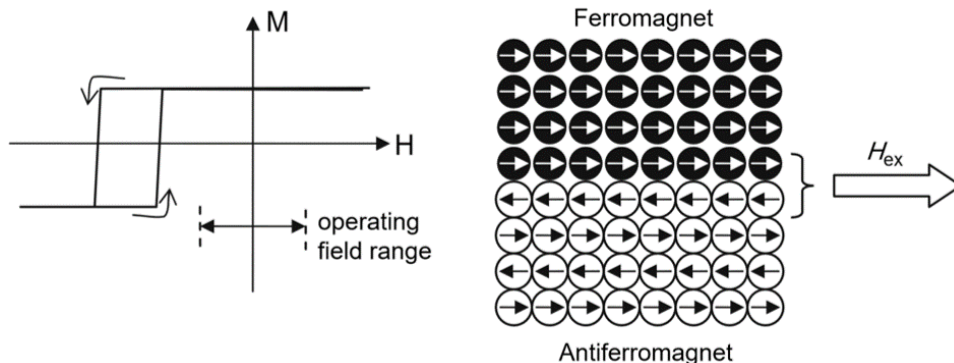


**Figure 3** – Exchange bias in ferromagnet/antiferromagnet bilayers with exchange field on the ferromagnetic layer,  $\mathbf{H}_{\text{ex}}$ , originating from the interface. Figure reproduced from Ref. [22, 23]

separately.

One can think of exchange bias in terms of a hysteresis loop, as in Fig. 3. First consider the case in absence of exchange bias, corresponding to a hysteresis loop around the origin. Applying an external magnetic field  $\mathbf{H}$  along the direction of the magnetization will cause the magnetization to point in the same direction as this magnetic field. When removing this magnetic field, the magnetization will remain as it is due to the anisotropy of the island. When increasing the magnetic field in the opposite direction, there will be a critical field magnitude where the magnetization will reverse as a whole. Hence, there exists a hysteresis loop in the  $(\mathbf{H}, \mathbf{M})$ -plane. Now one can also understand the case including exchange bias. The magnetization of the FM layer will have a strong preference to orient itself in the direction dictated by the AFM layer. Hence, exchange bias shifts the hysteresis loop along the  $\mathbf{H}$ -axis, as shown in Fig. 3.

## 1.4 Signal Propagation

Nanomagnetic logic gates need to be able to communicate with each other in order to form a larger and more useful circuit. For this, nanomagnets are placed next to each other, such that they form a sort of chain. Signal propagation through chains of nanomagnets does however come with some large complications. One of the advantages of nanomagnetic logic is that different islands influence each other, but this bidirectional interaction causes problems when trying to propagate signals. Let us start with examining the uniaxial case, as this has been studied most intensively, and then extend our knowledge to biaxial signal propagation.

### 1.4.1 Uniaxial

For islands with uniaxial anisotropy, a chain can be formed by placing elliptical islands next to each other, either along their hard axes (Fig. 4, left) or along their easy axes (Fig. 4, right). In the first case, nearest-neighbour dipolar field coupling imparts a preference for these islands to align anti-parallel, while in the second case the preferential orientation is parallel. Let us consider the first case now, as the second case is very similar.

Suppose an initial situation as shown at the top of Fig. 5, where the chain has been initialized in a ‘1’ state. Then all subsequent islands will prefer to be magnetized in alternating directions. Now the input bit is forcibly switched, so its magnetization points down, and we wish to propagate this signal through the chain, as shown on the second row of Fig. 5. The second magnetic moment then wants to align itself up due to its left neighbor (the input bit), but also wants to align itself down due to its right neighbor. As such, no net force acts on the second bit and it will randomly switch. Such a ‘defect’ in the chain is called a magnetic

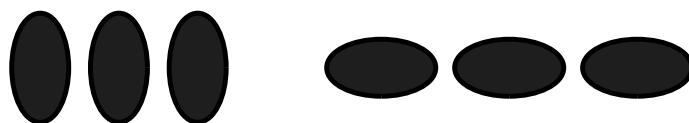


**Figure 4** – Two possible chain geometries for uniaxial islands. **Left:** chain along the islands’ hard axis. **Right:** chain along the islands’ easy axis.

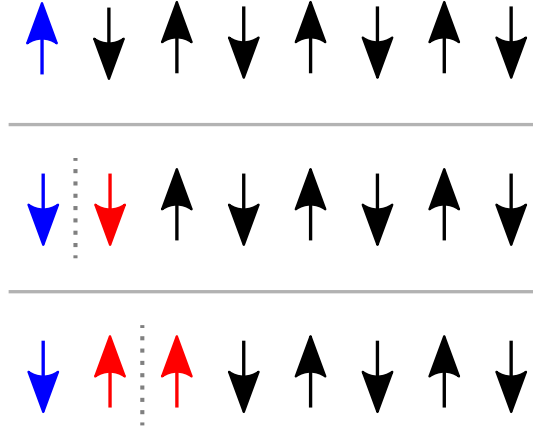


**Figure 5** – Blue arrows are the input bits. Red arrows have no preferred direction due to competing interactions of their neighbors. A dotted line indicates the location of a magnetic soliton. **Top:** initial ordering of the chain for a ‘1’ (up) input. **Middle:** input bit changes to ‘0’ (down), causing no net force to act on the second island. **Bottom:** second island randomly switches, causing no net force to act on the third island anymore either.

soliton [4]. As soon as this second bit randomly changes to the ‘up’ direction, the third bit is now in a similar situation, as shown at the bottom of Fig. 5, and the soliton has moved one island to the right. Now both the second and third bit have an equal chance of switching, and thus the signal has an equal chance of propagating forward to the output (third bit switches) or backward to the input (second bit switches). Thus, the signal (or, equivalently, the soliton) will perform a random walk along the chain. If the input bit is forced to remain ‘0’, the signal will thus reach the output after a time proportional to the square of the number of nanomagnets in the chain, which is clearly not ideal [24].

A possible solution to force the signal to propagate in one direction, makes use of additional biaxial anisotropy and an external magnetic field. The biaxial anisotropy is used to create a shallow energy minimum along the uniaxial anisotropy’s hard axis. The biaxial anisotropy can be realized either by choosing a material with intrinsic magnetocrystalline biaxial anisotropy, or by modifying the shape of the island such that it exhibits biaxial anisotropy. The latter gives great control over the relative strength of the biaxial versus uniaxial anisotropy [2, 25]. The external field is used to initialize each island in this new shallow energy minimum, along the hard axis of the uniaxial anisotropy, whenever a new bit needs to be propagated, which can be seen as a form of clocking. Due to the shallow energy minimum, the magnetization will first stay along this hard axis until it is disturbed by any of its neighbors. The first island is initialized in either the ‘0’ or ‘1’ state and functions as the input bit. When the external field is removed, the second island will feel the input bit’s dipole field, which will cause it to leave the shallow energy minimum and fall onto the easy axis. The third island then feels the second island falling in place, and so on. Thus, the signal successfully propagates in one direction [8, 25].

The use of an external magnetic field to reset the chain is not very ‘clean’, because a global

external field will affect all the chains in a given circuit. One possible solution is to manufacture the nanomagnetic islands such that each has a piezoelectric layer underneath, which can induce strain in the island, thus exerting a force on the magnetization. Each nanomagnet can then be controlled electronically. Another possibility is to place the nanomagnetic islands between electrodes which produce a spin-polarized current. Through the spin transfer torque, these electrons can then exert a torque on the magnetization [15, 22].

The case for a chain along the easy axes (Fig. 4, right) is very similar. The only difference is that, to perform the initialization procedure described above, the islands must now be initialized in an anti-parallel configuration, as a parallel configuration perpendicular to the length of the chain would be energetically unfavorable.

### 1.4.2 Biaxial

The most straightforward way to transmit biaxial information is to use a chain in a similar manner as in the uniaxial case, where the biaxial islands are placed with their easy axes in an ‘ $\times$ ’ configuration. The lowest energy configuration of such an ‘ $\times$ ’ chain is shown in Fig. 6, where the blue island is once again the input. Because of the biaxial anisotropy, there are four possible directions for the magnetization of this input island. Due to the high degree of symmetry of this chain geometry, all four possible inputs have equal ground state energy, so the chain is perfectly balanced. This balancedness will be explained in Section 4.1 using the energy landscape from Fig. 21.

This type of chain does, however, also hit the same problems with random walks. Unlike the uniaxial case, this can now no longer be resolved by initializing the islands in-plane in between the stable states such that they fall adiabatically to the energy minimum, because there are now four perpendicular stable states and there is hence no in-plane direction that does not favor any of these four directions. Initializing the islands out-of-plane can be a possible solution to this, but because the islands are typically very thin this will be an energetically very unfavorable situation, making such an initialization difficult.

Note that, if one connects a chain to a logic gate, the logic gate will influence the chain as much as the chain will influence the logic gate. If the input or output nanomagnets of a logic gate are close to the nanomagnets responsible for the logic operation, adding a chain can cause the logic gate to stop functioning correctly. Hence, it can be advantageous to design logic gates in such a way that their inputs and outputs are already at the end of a short chain, such that increasing the chain length to connect it to another logic gate does not significantly influence their functioning.



**Figure 6** – Minimal energy configuration of a balanced chain of biaxial nanomagnets. Blue arrow indicates the input island.



## 1.5 Imaging the magnetization

If one wishes to not only perform theoretical, but also practical studies on nanomagnetic islands, it can be useful to employ specialized microscopy techniques to image the magnetization direction. A small selection of often encountered techniques are presented in this section, each with certain advantages and disadvantages. Many other techniques besides those discussed below exist, like scanning electron microscopy with polarization analysis (SEMPA) [26], Lorentz microscopy [27], spin polarized scanning tunneling microscopies (SP-STM), superconducting quantum interference devices (SQUID) ...

### 1.5.1 Magnetic Force Microscopy

Magnetic Force Microscopy (MFM) is a form of scanning probe microscopy that can measure out-of-plane magnetic fields. For this, a cantilever with a magnetic tip is used which is scanned across the sample at a very low height. Typically, this magnetic tip is sensitive to out-of-plane magnetic fields, but by tilting the tip one can also measure in-plane components of the magnetic field [28], though these results might be more difficult to interpret as this tilt mixes different components of the magnetic field. If the tip were to simply scan over the surface without keeping a small distance to the sample, both the magnetic forces as well as the atomic forces would be measured. To remedy this, the topography of the sample is first determined using conventional atomic force microscopy [8, 29]. Once the topography is known, the magnetic tip can scan the sample while maintaining a constant distance above it at any point using the now known topography. This decouples the measurement of magnetic forces from the atomic forces and allows one to determine only the magnetic field. Important to note is that the force measured is only the out-of-plane component of the magnetic field, because the cantilever can only move vertically and is thus only sensitive to the vertical component of the magnetic field [8]. One must also take care that the magnetic tip does not significantly influence the magnetization of the sample itself [30].

When imaging a nanomagnet, it will manifest itself in the output as the combination of a region with positive and a region with negative out-of-plane magnetic field, because the stray magnetic field of a dipole curls back on itself [8]. An example of an MFM image of a chain of nanomagnets is shown at the top of Fig. 7.

The main disadvantage of MFM is that it does not image the magnetization directly, but rather the stray out-of-plane magnetic fields, which can make the results more difficult to interpret. It can however achieve a very high resolution due to its close resemblance to atomic force microscopy. Furthermore, it is a relatively cheap and commonly available technique compared to X-ray based techniques, which are discussed in the next section.

### 1.5.2 X-ray based magnetic imaging

Both Photoelectron Emission Microscopy (PEEM) and Magnetic Transmission X-ray Microscopy (MTXM) are techniques which rely on a physical phenomenon called X-ray Magnetic Circular Dichroism (XMCD). This effect states that the number of electrons emitted from the sample upon irradiation with circularly polarized X-rays depends on the magnetization direction of the

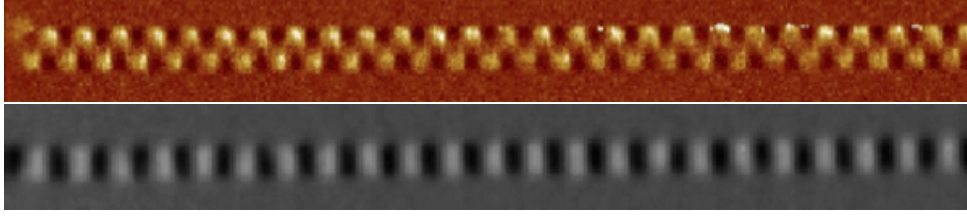


**Figure 7** – Typical MFM (top) and PEEM (bottom) image of the same chain of elliptical nanomagnets placed along their hard axes (as in the left part of Fig. 4), in their anti-ferromagnetically aligned ground state, indicating that these two techniques are sensitive to different components of the magnetic field. Dark regions correspond to low measured values, light regions to high values. Figures reproduced from Ref. [8].

surface of the sample [8]. More specifically, the measured quantity is the angle  $\theta$  between the magnetization direction  $\mathbf{M}(\mathbf{r})$  of the sample and the photon spin  $\sigma$ , which is aligned with the photon propagation direction and changes sign when the photon helicity is reversed [29]. The intensity of emitted electrons is given by

$$I_{\text{XMCD}} \propto M_{\text{sat}} \cos(\theta). \quad (1)$$

This way, the in-plane magnetization can be measured directly, which can make the results easier to interpret than an MFM image. An example of a PEEM image of a chain of nanomagnets is shown at the bottom of Fig. 7. To achieve high contrast, one can use X-rays with a frequency near an absorption edge [2].

Photoelectron Emission Microscopy (PEEM) images these secondary electrons emitted from the sample upon irradiation with X-rays. This kind of electron microscopy can achieve a high spatial resolution of less than 50 nm, with a typical probing depth in metals of about 2 nm due to the mean free path of the electrons, so PEEM is a surface sensitive technique. A slightly more detailed description of the geometry and image acquisition process of this kind of electron microscope can be found in [29].

Magnetic transmission X-ray microscopy (MTXM) is a similar technique which also relies on XMCD. However, instead of detecting the number of emitted electrons as in PEEM, it is now the transmission of X-rays through the sample that is measured. The penetration depth of 1 keV X-rays is about 100 nm [31]. MTXM can be used to image the magnetization dynamics themselves on sub-nanosecond time scales; imaging as fast as 100 ps has been reported and used in literature and techniques for probing on femtosecond time scales are under research [2, 31].

Besides the magnetization direction, also the chemical composition of the sample can be determined using the spectrum of emitted electrons or transmitted X-rays for PEEM and MTXM, respectively [29, 31]. Unfortunately, since XMCD requires circularly polarized X-rays, both imaging techniques require a synchrotron light source and corresponding equipment like helical undulators, which are only available at specialized institutes.

### 1.5.3 Magneto-Optical Kerr Effect

The Magneto-Optical Kerr Effect (MOKE) is another physical phenomenon that can be used to determine the magnetization direction. A linearly polarized laser beam is focused onto the sample, and the polarization state of the reflected light is measured in order to access the longitudinal Kerr effect [4]. This effect states that, depending on the angle between the magnetization and the incoming light, the reflected light will become elliptically polarized to a certain degree [32]. The effect is small, but the ellipticity is directly proportional to the cosine of the angle, which can then be used to derive the magnetization direction. There also exists the transversal Kerr effect, though this is not often used as it results in a change in reflectivity, which is more difficult to detect and prone to error.

Due to the diffraction limit of the laser, MOKE-based techniques have a low resolution and can only measure the average magnetization over a larger area, on the order of several  $\mu\text{m}^2$ . For structures smaller than this diffraction limit the signal strength diminishes [30]. One must take care that the focused laser beam does not excessively heat up the sample, as this could influence the magnetization itself. The temperature rise for a 2.5 mW laser focused on a 5  $\mu\text{m}$  diameter spot was however found to be negligible by Cowburn *et al.* [30].

This measurement technique can be easier or cheaper to set up than X-ray based techniques, but the low resolution does not allow the imaging of individual nanomagnets in complex structures.

### 1.5.4 Magnetoresistance

It is also possible to determine the magnetization angle of a single island by adding electrodes and employing effects from spintronics. These techniques have the drawback that they require additional features to be defined lithographically, other than just the islands themselves, which makes the manufacturing process more involved.

One option is to measure the planar Hall resistance [33]. This is done by applying a current in one direction through the island, and measuring the voltage in the direction perpendicular to this current. The measured resistance, as a function of the angle  $\phi$  between the in-plane magnetization and the current, is then proportional to  $\sin(2\phi)$ . As such, this only allows to determine the magnetization axis, because the planar Hall effect is symmetric under magnetization reversal [33].

Another option to measure the magnetization angle is to use a magnetic tunnel junction (MTJ) [22]. This consists of two ferromagnetic layers stacked on top of each other, with an insulating layer in between. When applying a voltage across both layers, a tunneling current will occur through the insulating layer, with the resistance depending on the relative magnetization angle of these two layers [34]. If the layers both have the same in-plane magnetization angle, the resistance is small. Conversely, for an anti-parallel alignment, the resistance is higher [22]. This effect is several orders of magnitude larger than the planar Hall effect [33].



## 2 Theoretical framework

*This section is based on the work in Ref. [35], where the theoretical framework of the micromagnetic theory and the origin of the different energy terms are described in an excellent and well-structured manner.*

Each atom has a discrete magnetic moment  $\mathbf{m}_i$  associated with it. The interaction of these many magnetic moments in a material can give rise to macroscopic effects. Since every magnetic moment interacts with every other magnetic moment, the underlying problem is a discrete N-body problem. Unfortunately, such a problem quickly becomes very hard if not impossible to solve analytically for even a few bodies, hence restricting analytical calculations to very small systems [35]. Due to the lack of an analytical solution, many particular problems can only be solved approximately in a numerical manner [35]. Even with numerical techniques, the computational power or time required to solve an N-body problem increases rapidly for an increasing amount of bodies, due to the number of interactions.

For this reason, a continuum theory was developed, called the **micromagnetic theory**. In this formalism, the magnetization is represented by the continuous magnetization field, denoted by  $\mathbf{M}(\mathbf{r}) = M_{\text{sat}}\mathbf{m}(\mathbf{r})$ . This is the magnetic moment per unit volume averaged over a small region of space, and has constant norm, with  $M_{\text{sat}}$  [ $\text{A m}^{-1}$ ] called the saturation magnetization [36].  $\mathbf{m}(\mathbf{r})$  is a unit vector field called the reduced magnetization, which should not be confused with the individual magnetic moments  $\mathbf{m}_i$ . The size of this small region is characterized by the exchange length  $\lambda$ , which is the smallest length scale over which the magnetization can vary. It should be much smaller than the size of a single magnetic domain, yet much larger than atomic dimensions, so on the order of several nanometres. This continuum approximation is only applicable if locally all discrete magnetic moments try to align themselves parallel to each other, i.e.

$$\mathbf{m}_i \approx \mathbf{m}_j \text{ if } |\mathbf{r}_i - \mathbf{r}_j| < \lambda, \quad (2)$$

as is for example the case in ferromagnets [35].

In situations where this approximation holds, the continuum theory can provide a significant computational improvement, because one can now use a finite difference approach with typical cell sizes on the order of  $\lambda$ . This significantly decreases the amount of variables compared to the original N-body problem, where every single atom had to be taken into account. The usual size of a simulation using micromagnetic theory is on the order of hundreds of nanometres, using millions of cells with dimensions on the order of  $\lambda$  [35].

Thus, the micromagnetic theory works well on a microscopic scale and can be solved numerically in a reasonable amount of time, which would be wholly impossible with an N-body approach.

### 2.1 Energy contributions

The energy corresponding to a static configuration of the reduced magnetization field  $\mathbf{m}(\mathbf{r})$  is the sum of several different contributions

$$E = E_{\text{exch}} + E_{\text{anis}} + E_{\text{demag}} + E_{\text{Zeeman}} + E_{\text{me}}. \quad (3)$$

The physical nature of these different terms along with small derivations to accomodate them to the continuum approximation are presented in this section.

### 2.1.1 Exchange energy

The exchange energy is of quantum mechanical origin. It tries to align neighboring spins and takes on the simple form

$$E_{i,j} = -J_{ij} \mathbf{S}_i \cdot \mathbf{S}_j. \quad (4)$$

Summing over all contributions gives

$$E = - \sum_{i,j} J_{ij} S^2 \mathbf{n}_i \cdot \mathbf{n}_j, \quad (5)$$

with  $\mathbf{S}_i = S \mathbf{n}_i$  and  $|n_i| = 1$ . The sign of  $J$  determines whether the spins align parallel ( $J > 0$ ) or anti-parallel ( $J < 0$ ). A parallel alignment results in a so-called ferromagnetic material, while an anti-parallel alignment is characteristic of an anti-ferromagnetic material.

Micromagnetic theory makes use of the magnetization field  $\mathbf{m}(\mathbf{r})$ , while Eq. (4) is discrete. An equation similar to (5), but for the continuous  $\mathbf{m}(\mathbf{r})$ , can now be written down:

$$E_{\text{exch}} = \int_{\Omega} \sum_i A_i \mathbf{m}(\mathbf{r}) \cdot \mathbf{m}(\mathbf{r} + \Delta \mathbf{r}_i). \quad (6)$$

Since two magnetic moments  $i$  and  $j$  only feel the exchange interaction when they are close to each other,  $\mathbf{m}(\mathbf{r}) \cdot \mathbf{m}(\mathbf{r} + \Delta \mathbf{r})$  can be expanded in first order [35] to

$$\begin{aligned} \mathbf{m}(\mathbf{r}) \cdot \mathbf{m}(\mathbf{r} + \Delta \mathbf{r}) &= 1 - \frac{1}{2} (\mathbf{m}(\mathbf{r}) - \mathbf{m}(\mathbf{r} + \Delta \mathbf{r}))^2 \\ &\approx 1 - \frac{1}{2} \sum_i (\Delta \mathbf{r} \cdot \nabla m_i)^2. \end{aligned}$$

This can be substituted into Eq. (6) [35, 36], finally yielding

$$E_{\text{exch}} = A_{\text{ex}} \int_{\Omega} \sum_i (\nabla m_i(\mathbf{r}))^2 d\mathbf{r}. \quad (7)$$

$A_{\text{ex}}$  is called the exchange stiffness constant [36]. The physical interpretation of this energy term is that the magnetization tries to align itself as smoothly as possible. The exchange length  $\lambda$ , which characterizes the length scale over which the magnetization can still be approximated as nearly uniform, is defined in SI units [37, 38, 39] as

$$\lambda = \sqrt{\frac{2A_{\text{ex}}}{\mu_0 M_{\text{sat}}^2}}. \quad (8)$$

It can be used as a rule of thumb for the cell size of micromagnetic simulations, which should be smaller than  $\lambda$  such that sampling at that length scale is sufficient to capture all relevant details [37].

### 2.1.2 Anisotropy energy

A material may exhibit anisotropy due to its crystal structure. This anisotropy typically exhibits the same symmetry as the crystal lattice. The most often encountered types of anisotropy are uniaxial and cubic anisotropy. Uniaxial anisotropy is common in hexagonal or tetragonal crystal structures, while cubic anisotropy is often present in FCC (face-centered cubic) or BCC (body-centered cubic) structures [35, 36].

In the uniaxial case, the energy is minimal when the magnetization lies along a certain axis  $\mathbf{u}$ . In the cubic case, there are three such axes  $\mathbf{e}_i, i = 1, \dots, 3$ , which are all equivalent. The direction of  $\mathbf{M}$  along this axis (i.e.  $\mathbf{m} = \pm\mathbf{u}$ ) does not matter, such that  $E(\mathbf{m}_{min}) = E(-\mathbf{m}_{min})$ . For this reason, only even orders in the Taylor expansion are considered [35]. For uniaxial anisotropy this gives

$$E_{anis,u} = - \int_{\Omega} (K_{u1}(\mathbf{m} \cdot \mathbf{u})^2 + K_{u2}(\mathbf{m} \cdot \mathbf{u})^4 + \dots) d\mathbf{r}. \quad (9)$$

The coefficients  $K_{ui}$  [ $\text{J m}^{-2}$ ] are called the uniaxial anisotropy constants. For cubic anisotropy, one can use a similar symmetry reasoning [35] to find

$$E_{anis,c} = \int_{\Omega} (K_{c1}(m_1^2 m_2^2 + m_2^2 m_3^2 + m_3^2 m_1^2) + K_{c2} m_1^2 m_2^2 m_3^2) d\mathbf{r}, \quad (10)$$

with  $m_i(\mathbf{r}) = \mathbf{m}(\mathbf{r}) \cdot \mathbf{e}_i, i = 1, \dots, 3$ .

### 2.1.3 Demagnetization energy

The demagnetization energy, often also called the magnetostatic energy, accounts for the dipole-dipole interaction. It is the energy arising from the interaction of every magnetic moment in a ferromagnetic material with the field of every other magnetic moment in the material [8]. In other words, it is the energy of the magnetization in the magnetic field created by itself [35]. From classical electrodynamics it is known that, in the absence of currents,

$$\nabla \cdot \mathbf{B} = 0 \quad (11)$$

$$\nabla \times \mathbf{H} = 0 \quad (12)$$

$$\mathbf{B} = \mu_0(\mathbf{H} + \mathbf{M}). \quad (13)$$

From (12) it immediately follows that  $\exists \psi(\mathbf{r}) : \mathbf{H} = -\nabla \psi$ . Substituting (13) into (11) yields

$$\nabla^2 \psi = \nabla \cdot \mathbf{M}. \quad (14)$$

The solution of this Laplace equation, for the boundary condition  $|\mathbf{r}| \rightarrow \infty \Rightarrow \psi \rightarrow 0$ , is found using Green's function and Green's theorem:

$$\begin{aligned} \psi(\mathbf{r}) &= -\frac{1}{4\pi} \int_{\Omega} \frac{\nabla' \cdot \mathbf{M}(\mathbf{r}')}{|\mathbf{r} - \mathbf{r}'|} d\mathbf{r}' + \frac{1}{4\pi} \int_{\partial\Omega} \frac{\mathbf{M}(\mathbf{r}') \cdot \mathbf{n}}{|\mathbf{r} - \mathbf{r}'|} d\mathbf{s}' \\ &= \frac{1}{4\pi} \int_{\Omega} \mathbf{M}(\mathbf{r}') \cdot \nabla' \frac{1}{|\mathbf{r} - \mathbf{r}'|} d\mathbf{r}'. \end{aligned}$$

A more rigorous derivation is given in [35]. From this explicit expression for  $\psi(\mathbf{r})$ , one can determine  $\mathbf{H}_{\text{demag}} = -\nabla\psi$ . The energy can then also be found through classical electrodynamics as

$$E_{\text{demag}} = -\frac{\mu_0}{2} \int_{\Omega} \mathbf{M} \cdot \mathbf{H}_{\text{demag}} d\mathbf{r}. \quad (15)$$

There is an additional  $\frac{1}{2}$  factor because each interaction is counted twice.

The quantity  $\nabla \cdot \mathbf{M}$  can be interpreted as a magnetic charge density, which the demagnetization energy then attempts to minimize [21]. In geometries larger than a few  $\mu\text{m}$ , this causes flux closure domains, which minimize the stray fields outside the geometry. In the small single-domain islands considered in this thesis, the demagnetization energy is not strong enough to overcome the exchange energy, so their magnetization is nearly uniform, with the demagnetization energy only causing slight deviations from this uniformity along the edge of the geometry.

#### 2.1.4 Zeeman energy

If an external field is applied, the magnetization will prefer to be aligned with this external field. This is described by an additional energy term similar to the demagnetization energy, but now without the factor  $\frac{1}{2}$  because the interaction comes from an external source:

$$E_{\text{Zeeman}} = -\mu_0 \int_{\Omega} \mathbf{M} \cdot \mathbf{H}_{\text{ext}} d\mathbf{r}. \quad (16)$$

#### 2.1.5 Other energy terms

Other energy terms still exist to describe other specific phenomena, though these will not be used in this work. One such energy term is the Dzyaloshinskii-Moriya interaction [40], which tries to orient neighboring spins perpendicular to each other, and is responsible for the stabilization of skyrmions as described in [41]. Another energy term is the magneto-elastic energy, which occurs when there are stresses present in the material [36], and can be used to propagate information through a nanomagnetic chain with a piezoelectric layer, as mentioned in the introduction.

### 2.2 Magnetization dynamics

The aforementioned energy terms express the potential energy of a static magnetization state  $\mathbf{m}(\mathbf{r})$ , but do not tell us how this magnetization evolves over time. Landau and Lifshitz [42] first described the time evolution of the magnetization field, as the sum of a precessional and a damping term [8, 35, 43]. The Landau-Lifshitz (LL) equation reads

$$\frac{\partial \mathbf{m}}{\partial t} = -\gamma'_0 \mathbf{m} \times \mathbf{H}_{\text{eff}} - \alpha' \mathbf{m} \times (\mathbf{m} \times \mathbf{H}_{\text{eff}}). \quad (17)$$

The meaning of both terms and their sum is illustrated in Fig. 8. The first term  $\mathbf{m} \times \mathbf{H}_{\text{eff}}$  describes the precession of the magnetization around the effective field and can be derived from quantum mechanical considerations. The second term  $\mathbf{m} \times (\mathbf{m} \times \mathbf{H}_{\text{eff}})$  was introduced phenomenologically, to make sure the precession does not carry on forever, and causes  $\mathbf{m}$  to



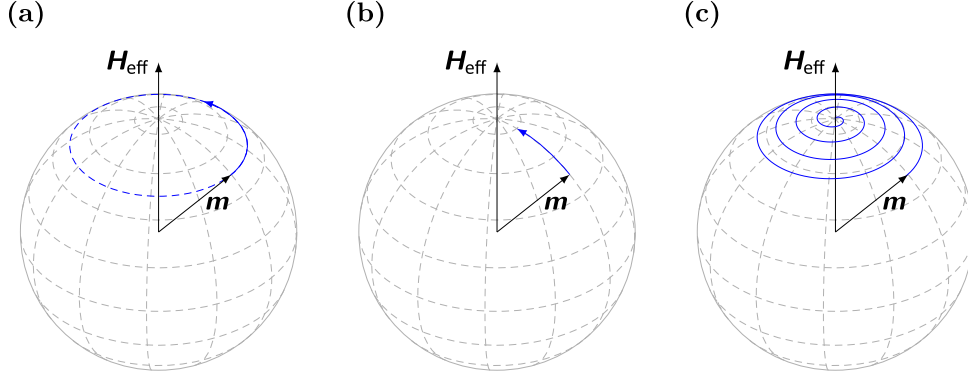


**Figure 8** – Motion of a magnetic moment as described by the LLG equation. The motion can be divided into the (a) precessional and (b) damping components. (c) resulting motion including both precession and damping. Figure reproduced from [35].

slowly damp toward the effective field vector  $\mathbf{H}_{\text{eff}}$  [8]. The effective field  $\mathbf{H}_{\text{eff}}$  is defined as

$$\mathbf{H}_{\text{eff}} = -\frac{1}{\mu_0} \frac{dE}{d\mathbf{M}}, \quad (18)$$

with the energy  $E$  the sum of several contributions as explained before [44]. Some reasons for the phenomenological damping are eddy currents, or spin-lattice coupling [43]. These are rather macroscopic explanations, which do not tell us anything about the fundamental origin of damping.

In order to obtain a physically more intuitive damping term, Gilbert [45] proposed an alternative form of the LL equation. He argued that, because  $\mathbf{m}(\mathbf{r})$  is always a unit vector, its motion can be described by that of a rotating body, thus allowing the use of a Lagrangian formalism to determine the dynamics of the system [35]. For the kinetic energy term in this Lagrangian, he proposed  $-M_{\text{sat}}/\gamma \dot{\phi} \cos(\theta)$ , with  $\phi$  and  $\theta$  spherical coordinates and the diacritic overdot denoting a time derivative, thus relating the damping to the time derivative of the magnetization [35]. This yields the Landau-Lifshitz-Gilbert (LLG) equation [43, 44, 46]

$$\frac{\partial \mathbf{m}}{\partial t} = -\gamma_0 \mathbf{m} \times \mathbf{H}_{\text{eff}} + \alpha \mathbf{m} \times \frac{\partial \mathbf{m}}{\partial t}. \quad (19)$$

Here,  $\gamma_0 = \mu_0 \gamma$  with  $\gamma$  the gyromagnetic ratio. The dimensionless  $\alpha > 0$  is called the *Gilbert damping constant*, and is for example equal to 0.01 for Permalloy. The precession frequency in absence of damping, also called the Larmor frequency, is given by  $f_L = \frac{\gamma_0}{2\pi} |\mathbf{H}_{\text{eff}}|$  [43]. It is also possible to derive the LLG equation as a limit case of a quantum mechanical description of a spin subjected to the effects corresponding to the different energy terms [35, 47].

Though the LL and LLG equations look slightly different, they can easily be transformed into each other [43, 44] using the substitutions

$$\begin{aligned} \gamma'_0 &= \frac{\gamma_0}{1 + \alpha^2} \\ \alpha' &= \alpha \frac{\gamma_0}{1 + \alpha^2}. \end{aligned}$$

By applying these substitutions, the first term in the LL equation (17) governing the precession frequency becomes dependent on the damping constant  $\alpha$ , which is the physically correct behavior [43].

Additional torques can also be taken into account, like the Zhang-Li or Slonczewski spin-transfer torques, which describe the interaction between a spin-polarized current and the magnetization [22, 39, 48]. This effect can for example be used, among many other applications, in information storage technologies like MRAM and magnetic field sensors [22].

### 2.2.1 Numerical solution

The micromagnetic theory described above makes abstraction of the individual atomic magnetic moments  $\mathbf{m}_i$  in favor of a continuum theory  $\mathbf{m}(\mathbf{r})$  to describe ferromagnetic materials. The time evolution of this theory is described by the Landau-Lifshitz equation (17), which provides an explicit form for the time derivative of the magnetization. For this reason, the LL equation is preferred over the LLG equation (19) in numerical solvers, as the latter is implicit. For most geometries, an analytical solution is very hard or even impossible to write down, so one has to resort to numerical approximations of the micromagnetic theory, like a finite difference (FD) discretization.

For this thesis, `mumax3` [39] will be used. This is a GPU-accelerated micromagnetic simulation program developed at the DyNaMat group of Ghent University. It calculates the space- and time-dependent magnetization dynamics in nano- to micro-sized ferromagnets using a finite-difference discretization, which is well suited for the problems considered in this thesis. By computing on the graphics processing unit (GPU), the finite difference scheme can be solved in parallel, significantly speeding up the calculation with respect to serial codes [49].

In order to perform a simulation, `mumax3` makes use of user-written input files, which give a lot of freedom to said user. One first defines the cell size of the finite difference grid, and the geometry  $\Omega \subset \mathbb{R}^3$  of the ferromagnetic material. Multiple regions  $\Omega_i$  can also be defined, which will prove useful when considering multiple nanomagnetic islands, as this allows for quantities to be calculated for each island separately. One can then initialize the magnetization  $\mathbf{m}(\mathbf{r})$  throughout the geometry. In this thesis, often a uniform magnetization  $\mathbf{m}(\mathbf{r}) = \mathbf{a}, \forall \mathbf{r} \in \Omega_i$  is used as the initial state. Once the magnetization has been initialized, there are two functions to allow the magnetization profile to settle to the geometry, in order to reach the local energy minimum. The first option is to `relax()` the magnetization. The function `minimize()` achieves the same, but takes larger steps and is therefore faster, but this can cause it to traverse saddle points and end up in a different local minimum. Finally, one can run the simulation for a given time in presence of thermal fluctuations, which will be discussed in the next section.

There are still many more micromagnetic features available in `mumax3`, though these are not relevant to this thesis. A more detailed description of the design of `mumax3` is available in reference [39].

### 2.2.2 Thermal fluctuations

The LLG equation only takes into account the fundamental physics of the magnetization dynamics at zero temperature. However, in our universe things exist at nonzero temperatures, and

thermal fluctuations play an important role in magnetic logic devices, for example for reverse calculations. In order to simulate nanomagnetic structures at nonzero temperatures, Brown [44] developed a theory to model thermal fluctuations in single-domain particles, by adding a stochastic thermal field  $\mathbf{H}_{\text{therm}}$  to the effective field  $\mathbf{H}_{\text{eff}}$  in the LLG equation. This thermal field has to fulfill certain statistical properties, namely

$$\langle \mathbf{H}_{\text{therm}} \rangle = 0, \quad (20)$$

$$\langle H_{\text{therm},i}(t) H_{\text{therm},j}(t') \rangle = q \delta(t - t') \delta_{ij}, \quad (21)$$

where  $q = (2k_B T \alpha) / (M_{\text{sat}} \gamma_0 \mu_0 V)$ , with  $V$  the volume of the single-domain particle [43]. The angled brackets in (20) denote a time average, while the angled brackets in (21) denote the correlation between the components of the thermal field. With these random and uncorrelated properties of the time-dependent additional field term, the LLG equation becomes a Langevin equation [44]. However, a nanomagnetic island is not a perfect single-domain particle with uniform magnetization, and different nanomagnetic islands can influence each other through magnetostatic interactions. Lyberatos [50] realized that every finite-difference cell in a numerical simulation can be seen as one such a single-domain particle, for which Brown's theory can then be applied [43]. More specifically, the thermal field was implemented in `mumax3` [39, 46] as

$$\mathbf{H}_{\text{therm}} = \mathfrak{N} \sqrt{\frac{2\alpha k_B T}{M_{\text{sat}} \gamma_0 \mu_0 V \Delta t}}, \quad (22)$$

where  $\mathfrak{N}$  is a random vector, determined from a standard normal distribution, whose value is changed after every time step. This equation is such that the thermal fluctuations are independent of the spatial and temporal discretization (volume  $V$  and time step  $\Delta t$ ) used. There are many finite-difference solvers available in `mumax3`, for example different orders of Runge-Kutta solvers, some of which benefit from the first-same-as-last (FSAL) property. In such solvers, the last torque evaluation of the current step is the same as the first evaluation of the next step, which allows an increase in efficiency because this step only has to be evaluated once. However, the stochastic thermal field is not constant, and hence these solvers can no longer benefit from the FSAL property when thermal fluctuations are present [46]. Another complication is that the time step  $\Delta t$  appears in the expression for  $\mathbf{H}_{\text{therm}}$ . Since some solvers in `mumax3` improve their efficiency by using an adaptive time step, one must take additional care that the thermal field is calculated correctly. A detailed description of the implementation of the stochastic thermal field in `mumax3` is given in [46].



### 3 Biaxial nanomagnetic island

In the first part of this thesis, the properties of a single biaxial island are investigated, as this will be the fundamental building block of more complex circuits. As thermal fluctuations play a big role in nanomagnetic logic, the energy barrier between stable states is important to investigate. The geometry of an island is one of the main factors determining this energy barrier. The geometry used throughout this thesis is the union of two identical perpendicular ellipses, as depicted in Fig. 9, where  $0^\circ$  is defined as the direction pointing to the right. When using the words ‘horizontal’, ‘vertical’ and ‘diagonal’ in the context of a biaxial island, this will always be in reference to this figure. This geometry was chosen because it should be reasonably easy to manufacture due to the lack of sharp corners, as opposed to for example a geometry made of rectangles. It has two ‘degrees of freedom’, namely the length of the long and short axis of the ellipse. As the geometry has 4 symmetry axes, for a single island it is sufficient to consider angles from  $0^\circ$  to  $45^\circ$ , though for clarity the figures will show from  $0^\circ$  to  $90^\circ$ . Throughout this thesis, the thickness of an island is always taken to be 5 nm.

We will define the *roundness*  $\rho$  as the ratio of the short over the long axis of the ellipses, and the overall *size*  $L$  as the length of the long axis. For example,  $(\rho, L) = (0.55, 100 \text{ nm})$  indicates that the long axis of each ellipse is 100 nm while the short axis is 55 nm, as in the figure.

Furthermore, the in-plane angles of several quantities will be used:  $\Theta$  denotes the instantaneous average magnetization angle, and its tilde counterpart  $\tilde{\Theta}$  the angle of the magnetization when it is relaxed to a local energy minimum. The angle of an external bias field is denoted by  $\chi$ , while its tilde counterpart  $\tilde{\chi}$  indicates a probing field. This probing field is used in the simulations to prevent the magnetization from fully relaxing to the easy axes, when quantities have to be calculated for situations where the magnetization is not in an anisotropic energy minimum. Finally,  $\Phi$  denotes the angle by which the geometry of a biaxial island was rotated, i.e. the angle between its ellipse axes and the numerical Cartesian grid of the simulation domain.

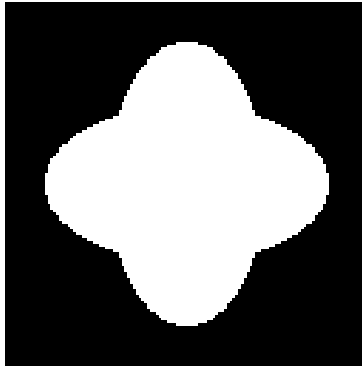


**Figure 9** – Typical geometry of the biaxial island under investigation, in this specific case for  $55 \times 100 \text{ nm}$  ellipses, i.e.  $(\rho, L) = (0.55, 100 \text{ nm})$ . White represents ferromagnetic material, black is free space.

### 3.1 Energy barrier

Due to symmetry reasons, all of  $E(\tilde{\Theta} = n45^\circ), n \in \mathbb{Z}$  are equilibria. However, not all are stable; some are energy minima while some are energy maxima. To determine the energy barrier  $E_{\text{barrier}}$  between stable states, the energy landscape as a function of magnetization angle must be calculated. Important to note is that, if one simply sets the magnetization  $\mathbf{M}$  of the entire island uniformly in one specific direction and calculates the energy, one finds that the energy is the same for all directions. Thus, if one wants to meaningfully calculate the energy landscape, the magnetization should first be relaxed to accommodate for the shape of the island. This is done using the `mumax3` command `minimize()`. However, simply doing so would result in a complete relaxation to an energy minimum, hence not yielding any useful information on the energy barrier, which is the difference between an energy minimum and maximum. To circumvent this issue, an external magnetic field is applied to keep the average magnetization  $\frac{1}{A} \int_A \mathbf{M} dA$  close to the desired direction. Practically, this *probing field*  $\mathbf{B}_{\text{ext,p}}$  is realized through the custom field functionality in `mumax3`, using `AddFieldTerm` and `AddEdensTerm`.

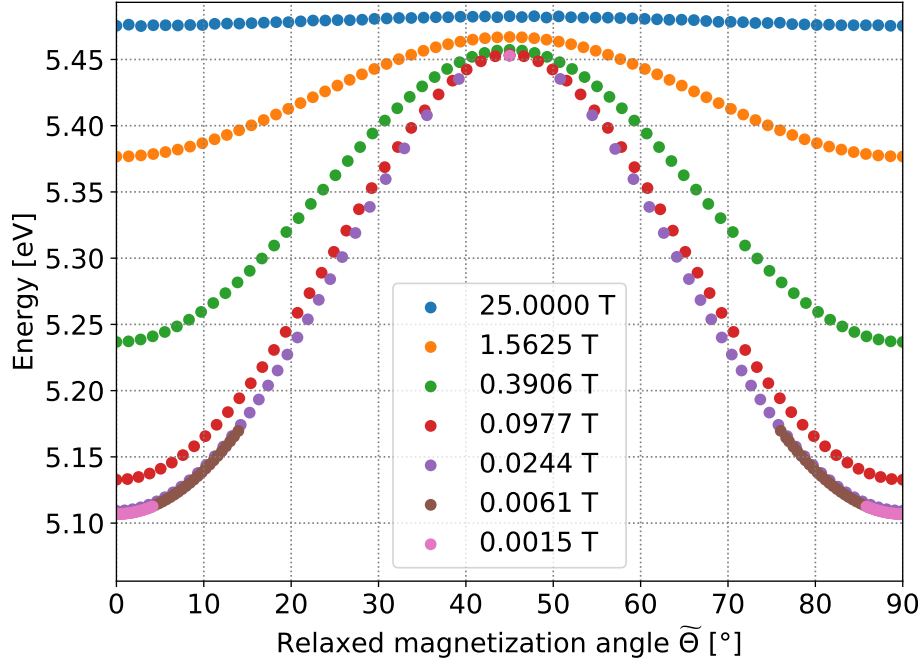
The procedure is therefore as follows. First, the magnetization of the entire island  $\mathbf{M}$  is initialized uniformly under an angle  $\Theta$ , and a probing field  $\mathbf{B}_{\text{ext,p}}$  is applied along that same direction. Then, the magnetization is relaxed using `minimize()`. The internal energy, responsible for the energy landscape, is then equal to  $E_{\text{total}} - E_{\text{Zeeman}}$ . This procedure to determine the internal energy is repeated for different angles  $\Theta$  to generate an energy landscape from which the energy barrier can be deduced.

#### 3.1.1 Optimal probing field magnitude

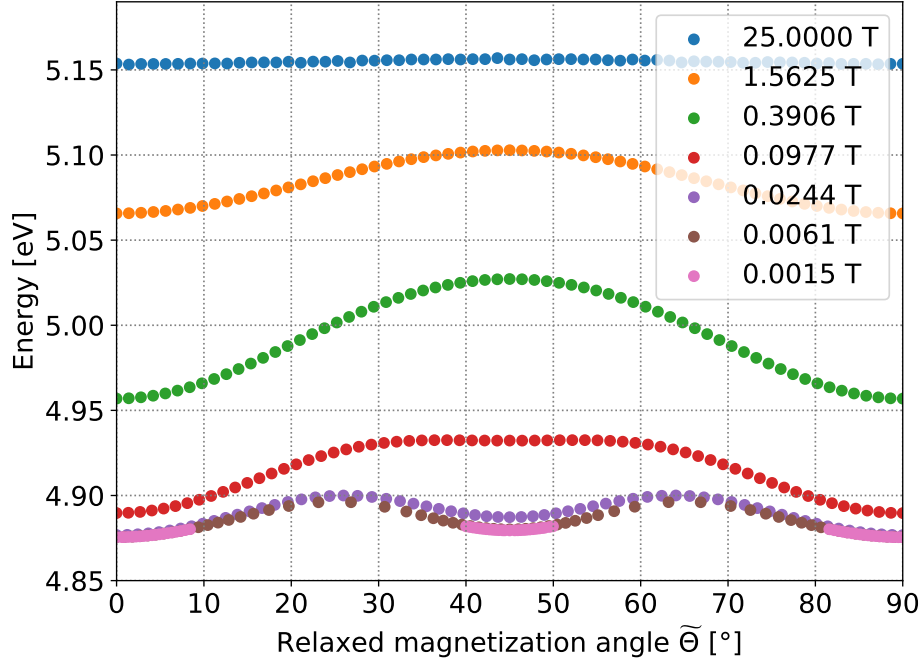
The procedure as described above makes use of a probing field. This is merely out of necessity to make sure that a magnetization initialized in an unstable maximum energy state stays there and does not relax to the energy minimum, which would prevent the determination of the height of the energy barrier. In reality, there is no such field, so this probing field should ideally be of small magnitude. To investigate the influence of this magnitude on the energy landscape, a simulation was carried out in which both the angle and the magnitude of the probing field were varied. In Fig. 10a, the magnitude of the probing field  $|\mathbf{B}_{\text{ext,p}}|$  was varied, with the angle  $\tilde{\chi}$  of this field taken at 64 equally spaced values from  $0^\circ$  to  $90^\circ$ . For each of these values, a point is plotted showing the relaxed magnetization angle  $\tilde{\Theta}$  and the corresponding energy. Note that the average relaxed magnetization angle  $\tilde{\Theta}$  is not necessarily equal to the probing field angle  $\tilde{\chi}$ , as the relaxation process will tend to more or less cant the magnetization towards the closest intrinsic energy minimum.

At very high magnetic fields, the magnetization of the entire island will be nearly uniform and will not follow the shape of the island along the edges. As mentioned before, this causes the energy to be the same for all angles, since it is the relaxation of the magnetization in a non-uniform way which causes the anisotropy [51]. This is the case in the figure for the extremely high field  $|\mathbf{B}_{\text{ext,p}}| = 25 \text{ T}$ .

The lower the magnetic field, the more the magnetization relaxes to the minimum, as can be seen from the spacing of the dots for each probing field magnitude. This is to be expected, as lower magnetic fields will have more difficulty to keep the magnetization pointed in the desired



(a)  $(\rho, L) = (0.65, 100 \text{ nm})$



(b)  $(\rho, L) = (0.482, 100 \text{ nm})$

**Figure 10** – Energy landscape for two different geometries, calculated using various probing field magnitudes  $|\mathbf{B}_{\text{ext,p}}|$  as shown in the legend. The probing field angle  $\tilde{\chi}$  was varied uniformly in 64 steps from  $0^\circ$  to  $90^\circ$ , for each magnitude, each dot corresponding to one such angle. The horizontal axis denotes the average magnetization angle  $\tilde{\Theta}$  after relaxation. Note that this is not necessarily equal to  $\tilde{\chi}$ , especially for low field magnitudes.

direction, against the shape anisotropy. This could be a problem when trying to determine the value of the energy maximum. This is however not the case, as evidenced by the single data-point at  $45^\circ$ , which stays at this unstable equilibrium even after relaxation, for all examined field magnitudes. The value of the energy maximum at  $45^\circ$  can hence be calculated, even without the need of a probing field. To be sure, however, that the magnetization truly does remain at the energy maximum when relaxing, a low probing field of 1 mT is applied anyway, as this will not significantly affect the calculated value.

If one is interested in the whole energy landscape rather than just the energy barrier, there exists a trade-off. For higher field magnitudes, the average magnetization angle  $\tilde{\Theta}$  remains close to the desired angle  $\tilde{\chi}$ , but the energy is not calculated accurately because the magnetization can not sufficiently relax to adjust to the geometry. For lower field magnitudes, the opposite is true. From the figure, it is seen that a field of about 0.1 T is an appropriate choice to balance the two aspects of this trade-off.

### 3.2 Energy landscape

We will henceforth refer to the energy difference between  $\tilde{\Theta} = 0^\circ$  and  $\tilde{\Theta} = 45^\circ$  as  $\Delta E_{45^\circ-0^\circ}$ . Due to the four-fold rotational symmetry, this is the energy difference with the highest possible degree of symmetry in the geometry under investigation. The difference between the highest and lowest points of the energy landscape, which are not necessarily located at  $0^\circ$  or  $45^\circ$ , will be called the *energy barrier*  $E_{\text{barrier}}$ .

The figure shows a nearly sinusoidal energy landscape for  $\rho = 0.65$ . As will be detailed further in the next section, the energy barrier is influenced by the roundness  $\rho$  of the ellipses constituting the island.

For  $\rho \approx 0.482$ ,  $\Delta E_{45^\circ-0^\circ}$  turns out to be approximately zero. This situation is shown in Fig. 10b, which reveals the additional anisotropy that is present in the system due to the broken symmetry caused by the magnetization settling itself to the geometry. The energy landscape is not entirely flat, even though  $\Delta E_{45^\circ-0^\circ} \approx 0$ . Instead, there is now an energy maximum in between  $0^\circ$  and  $45^\circ$ . Thus, in the case where the choice of roundness  $\rho$  causes  $\Delta E_{45^\circ-0^\circ}$  to be smaller than  $E_{\text{barrier}}$ , there are 8 local minima instead of 4, with equally many local maxima. Note that the energy landscape is still not perfectly sinusoidal; these new, smaller, energy maxima are not located at exactly  $22.5^\circ$ . One could wonder whether this is just a numerical quirk. This is certainly not the case, as will be detailed further in the section on numerical error.

#### 3.2.1 Energy barrier as function of geometry

The geometry is the most important factor determining the energy barrier. Shown in Fig. 11 is the dependence of the energy barrier on the roundness  $\rho$ , for different total sizes  $L$ . A positive value in this figure indicates that  $E(\Theta = 45^\circ) > E(\Theta = 0^\circ)$ , while for a negative value the opposite is true. This means that  $\Delta E_{45^\circ-0^\circ}$  is responsible for the sign in the plot, while it is the full energy barrier  $E_{\text{barrier}}$  that is plotted.

The behavior as a function of the roundness  $\rho$  is the clearest by only looking at the blue curve of this figure, i.e. for  $L = 128$  nm. Interesting is that the sign of  $\Delta E_{45^\circ-0^\circ}$  depends on  $\rho$ . A positive value corresponds to the long axes of the ellipses being the easy axes, while a



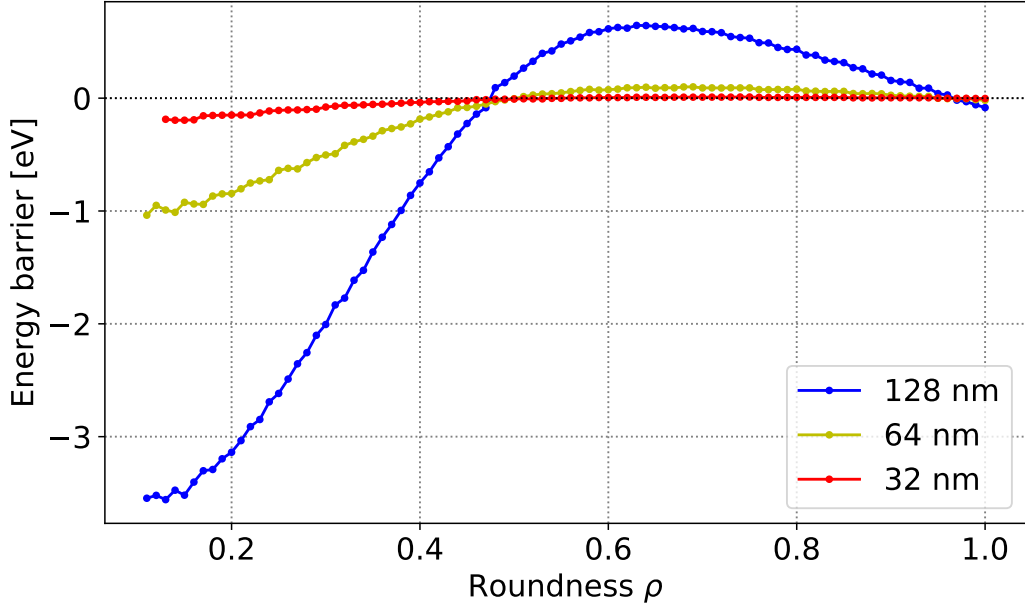


**Figure 11** – Energy barrier as a function of roundness  $\rho$ , for different total sizes  $L$  as listed in the legend. Cell size 1 nm. A positive value indicates that  $E(\Theta = 45^\circ) > E(\Theta = 0^\circ)$ , i.e. the hard axes are diagonal, while for a negative value the opposite is true.

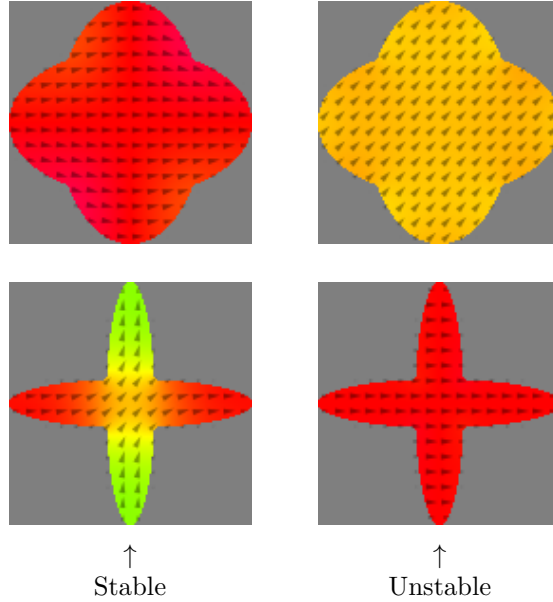


**Figure 12** – Relaxed magnetization for two different geometries with  $L = 100$  nm. The color hue represents the in-plane magnetization angle. **Top row:** roundness  $\rho = 0.6$ . **Bottom row:**  $\rho = 0.2$ . **Left column:** stable magnetization pattern. **Right column:** unstable magnetization pattern.

negative value indicates that an average diagonal magnetization at  $45^\circ$  is favored. This can be understood by looking at the detailed magnetization pattern corresponding to  $\tilde{\Theta} = 0^\circ$  and  $45^\circ$  in both regimes, as shown in Fig. 12. In general, the magnetization prefers a horizontal or vertical alignment, as these are the longest directions in the geometries. However, as the ‘arms’ get thinner for smaller  $\rho$ , it is no longer energetically favorable for the whole island to be magnetized uniformly, as this would not be along the long direction of at least two of the arms. Instead, for islands with low  $\rho$ , a domain wall is created in the center, and the magnetization is rather uniform in each of the two ellipses separately [33]. The sum of two such orthogonal magnetizations is on average diagonal, hence explaining the global behavior of the easy axes if one only observes the average magnetization angle  $\tilde{\Theta}$ . Interesting is the observation that there exists a  $\rho \neq 1$  where the energy barrier switches sign, meaning that the easy and hard axes swap. The energy landscape never becomes truly flat, which can be seen in the figure as the sudden small but sharp drop around  $\rho = 0.48$ , where the function switches sign.

From Fig. 11, it can be seen that the energy barrier depends on the total size  $L$ . When halving  $L$ , the energy barrier becomes approximately 4 times smaller. This nonlinear relationship is shown in Fig. 13, where the island size  $L$  is varied for some constant values of  $\rho$ . As the thickness of the island is constant throughout these simulations, this indicates that the energy barrier is proportional to the volume of the island, as expected from theory.

The energy barrier goes to zero for  $\rho \rightarrow 1$ , as one would expect for a perfectly round geometry. However, due to numerical error, the barrier is not calculated as exactly zero, which will be covered in the next section.

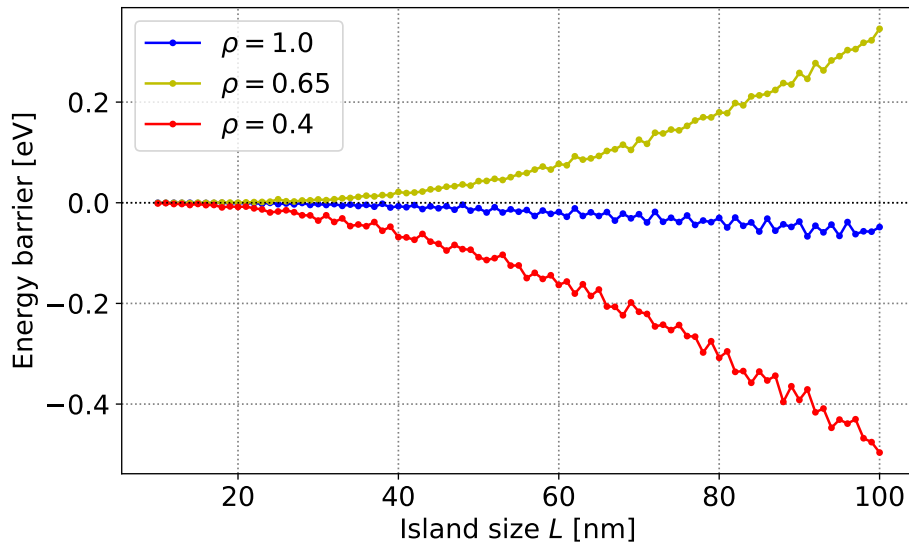


**Figure 13** – Energy barrier as a function of island size  $L$ , for 3 different roundnesses as listed in the legend. Cell size 2 nm. A positive value indicates that  $E(\Theta = 45^\circ) > E(\Theta = 0^\circ)$ , i.e. the hard axes are diagonal, while for a negative value the opposite is true.

### 3.2.2 Numerical error: influence of cell size on the energy barrier

When performing more resource-intensive simulations, it is advantageous to use as large a cell size as possible in order to minimize the total amount of cells in the simulation. Increasing the size of the cells does, however, also increase the numerical error originating from the discretization of the grid. The size of this numerical error was examined by determining the energy barrier for different shapes (varying roundness and overall size) and for different cell sizes, viz. 4 nm, 2 nm and 1 nm. The results of this calculation are shown in Fig. 14.

The figure obtained with cells of 1 nm is the smoothest, so it is justified that this size was used in the previous paragraphs. For 2 nm cells, the curve becomes rougher, but the overall shape remains similar to that of 1 nm cells. Cells of 4 nm, however, yield a very rough and almost staircase-like energy landscape, indicating that 4 nm cells are too large to get a physically accurate solution.

The global behavior as function of cell size, is that larger cells result in a lower value of the energy barrier. For nearly round geometries ( $\rho \rightarrow 1$ ), the energy barrier becomes quite large for a cell size of 4 nm (240.7 meV). In reality, a round geometry should of course not have a preferential direction. Because of the Cartesian simulation grid, however, a preferential orientation is created in the simulation. It was mentioned previously that the magnetization prefers to align itself along the longest direction of a given geometry. For a square, this is along the diagonals. When using the largest cells, the geometry most clearly consists of a bunch of squares, so the magnetization will be more inclined to align diagonally. When the hard axes

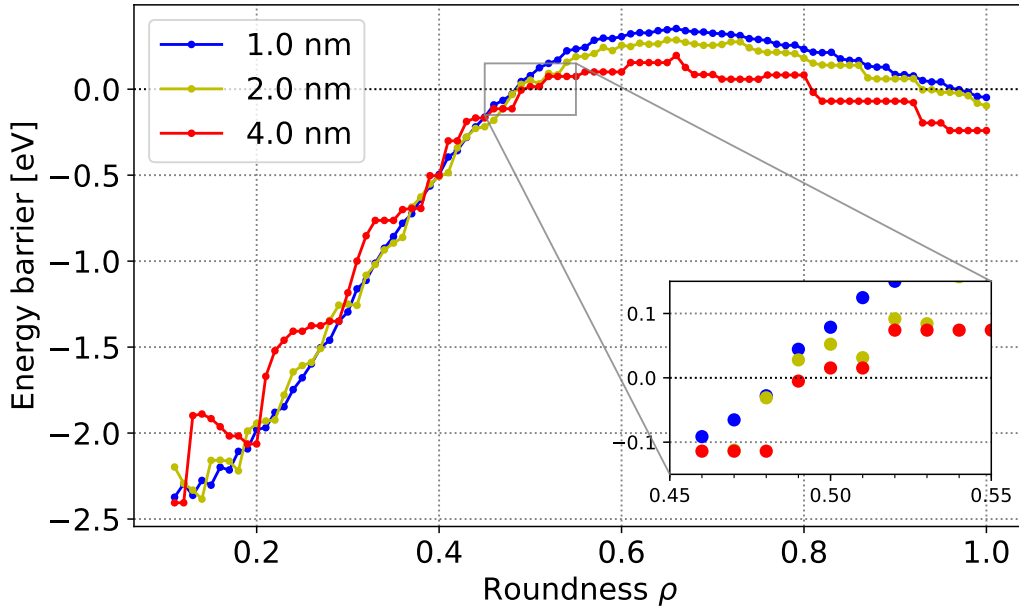


**Figure 14** – Energy barrier as a function of roundness  $\rho$ , for different cell sizes as listed in the legend. Long ellipse axis  $L = 100$  nm. A positive value indicates that  $E(\Theta = 45^\circ) > E(\Theta = 0^\circ)$ , i.e. the hard axes are diagonal, while for a negative value the opposite is true.

are diagonal and the true physical energy barrier is sufficiently large, or when the cells are sufficiently small, the numerical error is not ‘strong’ enough to swap the easy and hard axes. For small energy barriers and large cells, however, the effect is clearly noticeable, as is here the case for  $\rho \rightarrow 1$ . As the quantity plotted in Fig. 14 is positive when the easy axes are horizontal and vertical, and negative when they are diagonal, the effect of the Cartesian grid is for the lines in the figure to drop down.

From the inset in the figure, which enlarges the region around  $\rho = 0.49$ , it is observed that the energy barrier gets much closer to zero for the 4 nm cells than it does for the smaller cells. Thus, since smaller cells more closely correspond to reality, one can conclude that the earlier observation that the energy landscape is not entirely flat even when  $\Delta E_{45^\circ-0^\circ} \approx 0$ , is definitely a real phenomenon, not just some numerical artefact.

Everything taken into account, it seems that the optimal compromise between simulation speed and accuracy, is a 2 nm cell size. However, if one is solely interested in the physics corresponding to a specific value of the energy barrier, while making abstraction of other aspects like the geometry, any cell size can be used as long as the corresponding energy barrier for that discretization is known.

### 3.2.3 Energy landscape in presence of an external bias field

The sole purpose of the probing field  $\mathbf{B}_{\text{ext},p}$  used in the previous paragraphs was to make sure the magnetization remains at the energy maximum, in order to determine the value of this maximum. It is also possible to put the biaxial island in an external bias field, denoted as  $\mathbf{B}_{\text{ext}}$ . This will make the Zeeman energy term of Eq. (16) nonzero, hence adding a cosine function

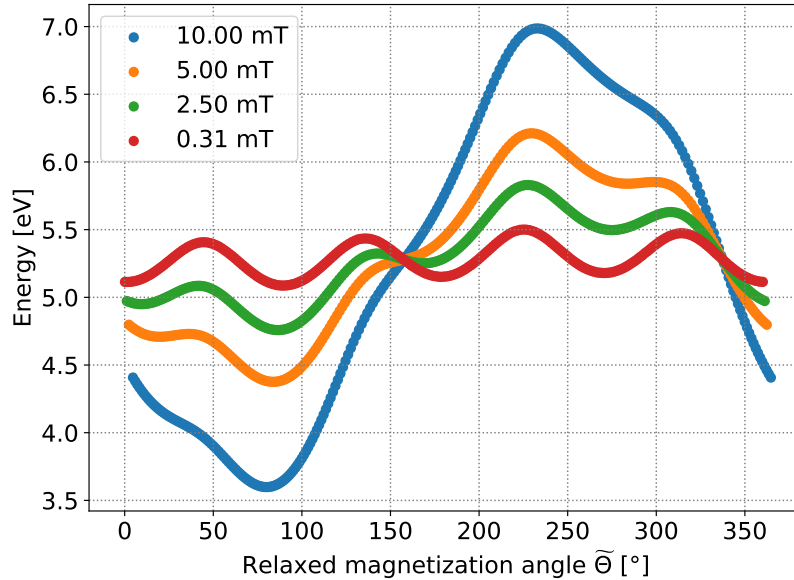


**Figure 15** – Energy landscape as function of magnetization angle after relaxation, for different external bias field magnitudes  $|\mathbf{B}_{\text{ext}}|$  as listed in the legend, with the external bias field applied at an angle  $\chi = 67.5^\circ$ . The island geometry is  $(\rho, L) = (0.65, 100 \text{ nm})$ .

to the energy landscape. In order to visualize the energy landscape, the probing field is still necessary to stabilize the magnetization in the desired direction, away from the global minimum. This can be done in `mumax`<sup>3</sup> by using a custom field for the probing field and using the normal external field functionality for the bias field, hence decoupling the calculation of their energies and allowing the probing field to be ignored afterwards when calculating the internal energy. As an example, the energy landscape for a situation where the external bias field was applied at  $\chi = 67.5^\circ$  is shown in Fig. 15, where the additional cosine is clearly visible.

### 3.3 Thermal switching

Real nanomagnets exist at nonzero temperatures. These thermal fluctuations cause the magnetization of every atom to feel an additional random torque. Over time, the sum of these fluctuations can allow the magnetization to overcome the energy barrier and switch between two stable states. One of the main topics of interest is the thermal switching frequency that accompanies a certain energy barrier.

#### 3.3.1 Theory

The random thermal switching can be modeled as being driven by a jump-noise process [52], which is a process where the magnetization experiences random jumps, at random times [53]. This process is memoryless, and can therefore be characterized in time by a scattering rate  $\Gamma$ . As such, at any given moment, the probability that the next jump occurs within a time  $\tau$  is given by

$$P(t < \tau) = 1 - \exp(-\Gamma\tau). \quad (23)$$

The random number  $\tau$  can then be computer-generated by using the equation

$$\tau = -\frac{1}{\Gamma} \ln(1 - P_i), \quad (24)$$

with  $P_i$  a uniformly distributed random number between 0 and 1 [53]. By using the principle of the ‘detailed balance’, it can be shown that the switching rate between two energy minima separated by an energy barrier  $E_{\text{barrier}}$  follows a classical Arrhenius law, as is typical for thermally activated switching phenomena [52]:

$$\Gamma \propto \exp(-E_{\text{barrier}}/k_B T). \quad (25)$$

By combining (24) and (25), the random time between two switches  $t_i$  can then be calculated as

$$t_i = -\frac{1}{f_0} \exp\left(\frac{E_{\text{barrier}}}{k_B T}\right) \ln(1 - P_i), \quad (26)$$

valid in the regime where  $E_{\text{barrier}} \gg k_B T$ . The constant  $f_0$  is called the *attempt frequency*. The average value of  $-\ln(1 - P_i)$  is then  $\ln(4)$ , which reduces (26) to

$$t_i = \frac{\ln(4)}{f_0} \exp\left(\frac{E_{\text{barrier}}}{k_B T}\right). \quad (27)$$

Conversely, if a specific switching time  $t_i$  is desired, the required energy barrier is given by

$$E_{\text{barrier}} = k_B T \ln \left( \frac{f_0 t_i}{\ln(4)} \right). \quad (28)$$

The main unknown in all previous equations is the attempt frequency  $f_0$ . As this parameter is crucial to achieve a correct estimate for the switching time, it will be determined both theoretically and through numerical simulations with the biaxial geometry.

A theoretical equation for  $f_0$  (in  $\text{rad s}^{-1}$ ) in the case of uniaxial anisotropy [39, 46, 54] is given by

$$f_0 = \gamma \frac{\alpha}{1 + \alpha^2} \sqrt{\frac{4K_{\text{u1}}^3 V}{\pi M_{\text{sat}}^2 k_B T}}, \quad (29)$$

with  $\gamma$  the previously encountered gyromagnetic ratio equal to  $1.7595 \times 10^{11} \text{ rad T}^{-1} \text{ s}^{-1}$ ,  $\alpha$  the dimensionless damping constant,  $V$  the volume of the nanomagnet, and  $K_{\text{u1}}$  and  $M_{\text{sat}}$  the uniaxial anisotropy constant and saturation magnetization as defined in Section 2. The anisotropy constant in general is equal to the energy barrier corresponding to said anisotropy, divided by the volume of the particle. Hence, (29) can be adapted to a general anisotropic situation by substituting  $K_{\text{u1}} \rightarrow E_{\text{barrier}}/V$ , yielding

$$f_0 = \gamma \frac{\alpha}{1 + \alpha^2} \frac{2}{M_{\text{sat}} V} \sqrt{\frac{E_{\text{barrier}}^3}{\pi k_B T}}. \quad (30)$$

An alternative equation is found in Ref. [55], which after simplification in the absence of an external field boils down to twice the value obtained from (30), and thus yields the same order of magnitude.

Let us now estimate  $f_0$  theoretically using Eq. (30) at 300 K for a 5 nm thick biaxial island with  $L = 100 \text{ nm}$  made of Permalloy, a material for which  $M_{\text{sat}} = 8 \times 10^5 \text{ A m}^{-1}$  [39]. The energy barrier is chosen at  $E_{\text{barrier}} = 154.7 \text{ meV}$ , as this is one of the barriers that will be used in the simulations later. Since the equations for  $f_0$  merely estimate its order of magnitude, the volume  $V$  must not precisely be known and can hence be approximated by the volume of a circular ( $\rho = 1$ ) geometry, i.e.  $V \approx 4 \times 10^{-23} \text{ m}^3$ . The damping constant is taken as  $\alpha = 0.01$ .

This yields a theoretical estimate of  $f_0 = 6 \times 10^5 \text{ s}^{-1}$ . We will compare this to the values obtained through simulations with `mumax3` in the next section.

### 3.3.2 Simulations

Given the total simulation time  $t_{\text{max}}$  and the number of switches  $N$  during this time interval, an estimate for  $f_0$  can be derived from Eq. (26) as

$$f_0 = \frac{N \ln(4)}{t_{\text{max}}} \exp \left( \frac{E_{\text{barrier}}}{k_B T} \right). \quad (31)$$

There exists some ambiguity as to how one can count the amount of switches during a time interval. The method applied here counts every monotone rotation of the magnetization over more than  $90^\circ$  in either direction as a switch. Hence, not every crossing of an energy maximum is counted as a separate switch; when the magnetization rotates through multiple energy maxima

**Table 4** – Values of the attempt frequency  $f_0$  for different energy barriers (determined by the roundness  $\rho$  and grid discretization), temperatures and values of the damping constant.  $L = 100$  nm and  $M_{\text{sat}} = 8 \times 10^5$  A m $^{-1}$  for all entries.

$\rho$	Grid [nm]	Barrier [meV]	T [K]	$\alpha$	$t_{\text{max}}$ [ns]	$N$	$f_0$ [s $^{-1}$ ]
0.49	2	27.8 <sup>a</sup>	300	0.01	100	37	$1.50 \times 10^9$
0.65	4	154.7	273	0.01	1000	13	$1.29 \times 10^{10}$
0.65	4	154.7	300	0.1	1000	12	$6.61 \times 10^9$
0.65	4	154.7	300	0.01	1000	11	$6.05 \times 10^9$
0.65	4	154.7	350	0.01	1000	41	$9.60 \times 10^9$
0.65	2	286.2	350	0.01	500	0	0
0.65	3.125	207.9	350	0.01	1000	9	$1.23 \times 10^{10}$
1	4	240.7	300	0.01	1000	0	0
1	4	240.7	350	0.01	1000	5	$2.03 \times 10^{10}$

<sup>a</sup> This energy barrier is comparable to the thermal energy  $k_B T$ . Hence, the switching rate ( $\approx 2$  ns) is on the same timescale as the LLG dynamics, which causes the estimate for  $f_0$  using Eq. (30) to be inaccurate.

in quick succession, such switches larger than  $90^\circ$  are counted as one single switch. As soon as the magnetization starts turning in the opposite direction, any subsequent  $90^\circ$  turn or larger is counted as another switch.

Several simulations were carried out for  $t_{\text{max}}$  up to 1  $\mu$ s, where the temperature  $T$ , the energy barrier and damping constant  $\alpha$  were varied. Examples of such simulations are shown in Figs. 16 to 18, and a summary of all conducted simulations is given in Table 4. For each simulation, a theoretical value for  $f_0$  was estimated using Eq. (31) as listed in the last column of the table. Nearly all simulations for which the energy barrier is significantly higher than the thermal energy yield a value around  $f_0 = 10^{10}$  s $^{-1}$ , apart from some outliers which did not switch within  $t_{\text{max}}$ . Unfortunately, this estimate is three orders of magnitude larger than the theoretical estimate determined in the previous section. This indicates that the theoretical equation (30) is not applicable. The reason for this is unclear, but we hypothesize that this is because the magnetization is not perfectly uniform in the simulation, which is one of the assumptions underlying the theoretical equation.

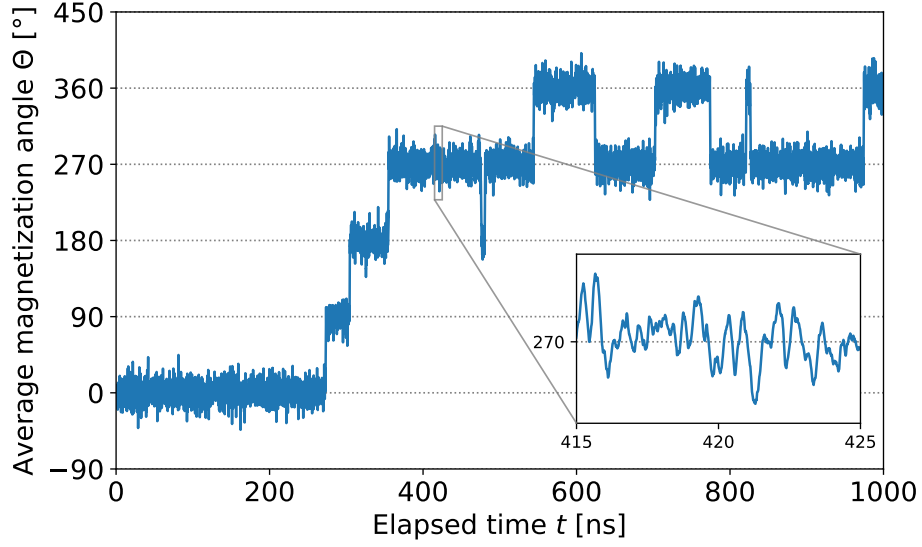
The value obtained through the simulations is, however, on the same order of magnitude as the intrinsic resonance frequency of the magnetization in the local energy landscape around the energy minima from Fig. 10. Apart from the quantitative measure for  $f_0$ , some qualitative aspects of changing the parameters will now be addressed.

### Effect of damping constant $\alpha$

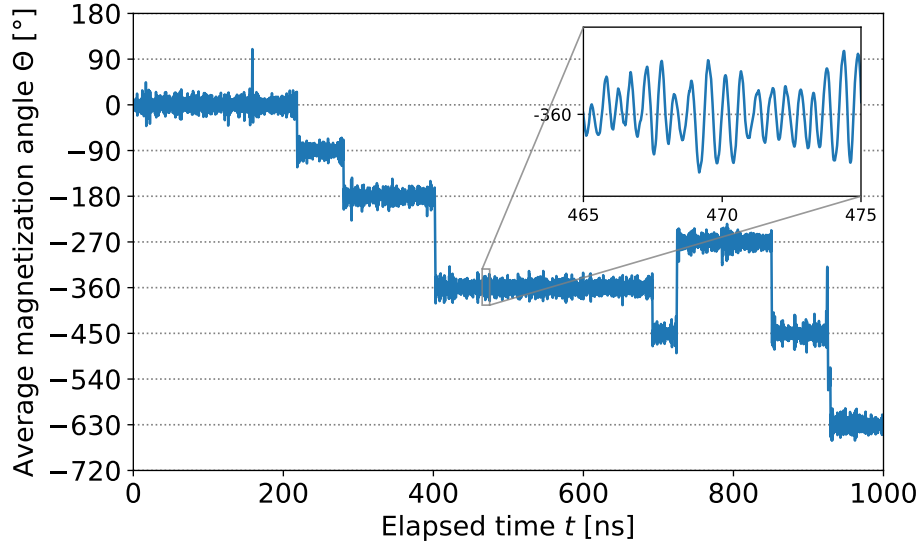
The effect of changing the damping constant  $\alpha$  is shown in Fig. 16. There is a qualitative difference between  $\alpha = 0.1$  (Fig. 16a) and  $\alpha = 0.01$  (Fig. 16b). For higher  $\alpha$ , only single switches occur, i.e.  $90^\circ$  between adjacent energy minima. For lower damping, switching may occur over more than  $90^\circ$ ; as an example, there are three switches over  $180^\circ$  visible in Fig. 16b. This is understandable since the magnetization can be seen as a rotating body as described

earlier in Section 2. Hence, less damping implies that the magnetization will more easily retain its angular velocity after overcoming the first energy maximum, and can thus overcome multiple energy barriers in quick succession.

From Eq. (22), which gives an expression for the thermal field, it is known that the magnitude of this thermal field is proportional to the square root of the damping constant. The effect of this is noticeable in the inset figures of Fig. 16. For  $\alpha = 0.01$ , the magnetization rotates in a smooth manner, oscillating quasi-harmonically in one of the four energy valleys. Because the coupling to the thermal field is weak, the thermal field only introduces randomness in the amplitude of this



(a)  $\alpha = 0.1$



(b)  $\alpha = 0.01$

**Figure 16** – Switching for two different values of the damping constant  $\alpha$ , with a grid discretization of 4 nm at 300 K, for  $(\rho, L) = (0.65, 100 \text{ nm})$ .



oscillation, and does not significantly distort the sinusoidal pattern itself. For a higher  $\alpha = 0.1$ , the rotation exhibits more jagged behavior, on the one hand due to the higher damping, on the other hand due to the larger coupling with the thermal field.

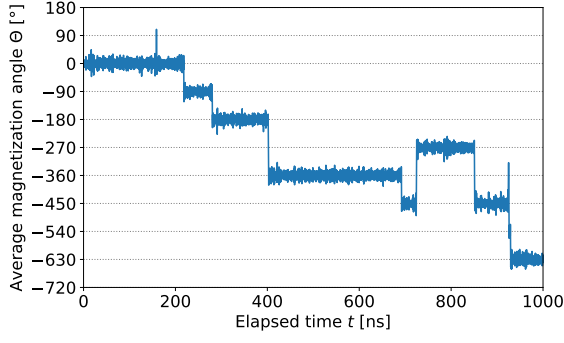
Quantitatively, the effect of  $\alpha$  on  $f_0$  can be examined by comparing rows 3 and 4 of Table 4. There does not seem to be a significant dependence on the damping constant  $\alpha$ , contrary to the inverse proportionality predicted by the theory of Eq. (30), further indicating that the theoretical equation does not apply. Note, however, that the estimate  $f_0 \approx 10^{10} \text{ s}^{-1}$  is quite close to the frequency of the intrinsic oscillation visible in the inset figures (Fig. 16b), which has a period of 0.5 ns. It is logical that  $f_0$  is related to this frequency, as one can see this oscillation as an ‘attempt’ to leave the energy minimum once every half-period.

### Effect of temperature and energy barrier

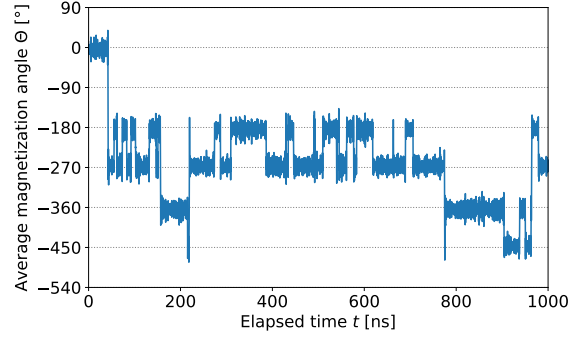
It is expected that  $f_0$  exhibits an exponential dependency on the ratio between energy barrier and temperature. To confirm this, simulations spanning 1  $\mu\text{s}$  were carried out for two different temperatures and two different energy barriers. The different energy barriers correspond to  $\rho = 0.65$  (154.7 meV) and  $\rho = 1$  (240.7 meV) geometries at a cell size of 4 nm. Such a large cell size was chosen because these simulations take a long time to run, and we are only interested in the behavior accompanying a certain energy barrier, while making abstraction of all other aspects. Note that these two geometries have opposite easy and hard axes. This is clearly visible in the figures, as the 154.7 meV case is stable around  $n90^\circ$ ,  $n \in \mathbb{Z}$ , while 240.7 meV is stable around  $45^\circ + n90^\circ$ . The exponential dependence on the temperature is qualitatively clear from the difference between Figs. 17a and 17b, where the latter switches significantly more for only a 16 % increase in temperature. The exponential dependence on the energy barrier can be seen in the difference between Figs. 17a and 17c, where the latter has not a single switch due to the 55 % higher energy barrier. The numerical value for  $f_0$  is also for these simulations close to  $10^{10} \text{ s}^{-1}$ , as listed in Table 4.

### Limit of low barrier

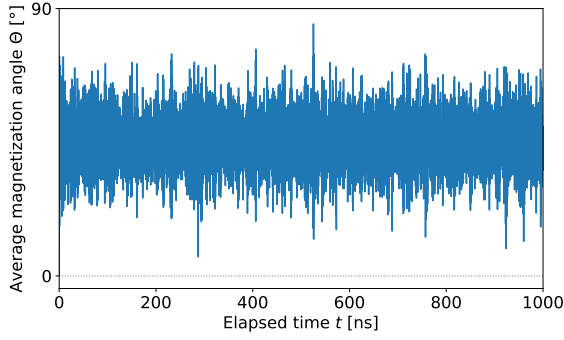
In the limit where the energy barrier is comparable to the thermal energy  $k_B T$ , the exponential law from Eq. (31) no longer holds, because that law is based on the assumption that the magnetization angle distribution is sufficiently concentrated near an energy minimum [44]. For such a low barrier, the switching rate is on the same timescale as the LLG dynamics, such that besides the energy barrier, now also these dynamics play a major role. An example of a 100 ns simulation for an energy barrier of 27.8 meV is shown in Fig. 18. As one would expect, the magnetization does not get stuck in any of the energy minima because they are too shallow. The switching frequency for such a low barrier comes close to that of the intrinsic sinusoidal pattern visible in the inset of Fig. 16b.



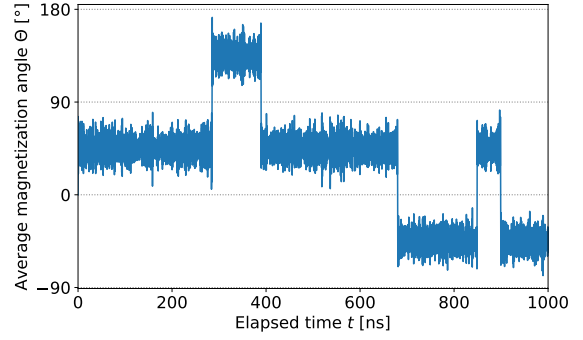
(a) 300 K, 154.7 meV



(b) 350 K, 154.7 meV



(c) 300 K, 240.7 meV



(d) 350 K, 240.7 meV

**Figure 17** – Switching for two different energy barriers and two temperatures, with a grid discretization of 4 nm and  $\alpha = 0.01$ . The energy barrier of 154.7 meV corresponds to a geometry with  $\rho = 0.65$ , and 240.7 meV to  $\rho = 1$ .

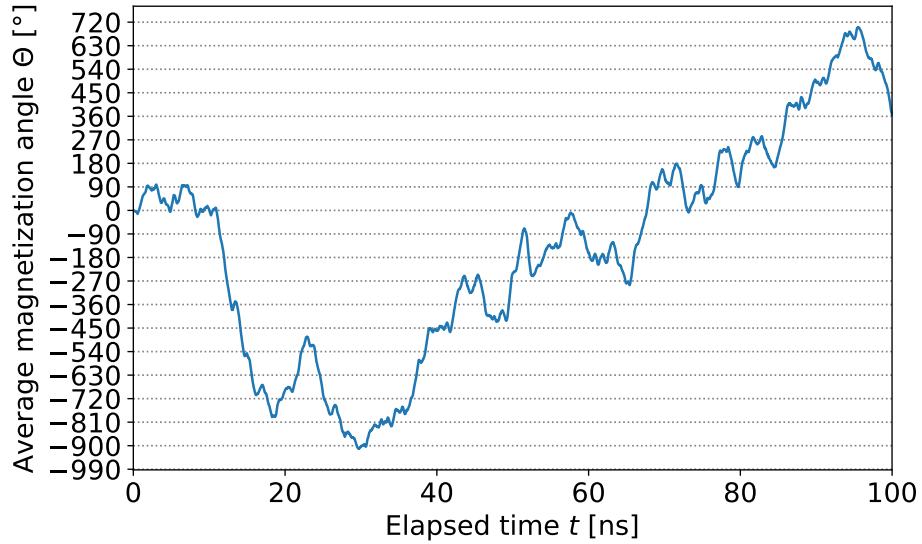


**Figure 18** – Switching for an energy barrier of 27.8 meV, corresponding to  $\rho = 0.49$  for a grid discretization of 2 nm. Temperature 300 K and  $\alpha = 0.01$ .

## 4 Interaction between two islands

The total energy of two interacting islands can be seen as the contribution of three components: the shape anisotropy of the first island, the shape anisotropy of the second island, and the interaction energy between both islands. The anisotropy of a single island has already been examined in Section 3.1, and depends on its average magnetization angle  $\Theta$ , total size  $L$ , and roundness  $\rho$ . It is expected that the interaction energy between two islands will primarily depend on the distance  $d$  between the centers of the two islands, the average magnetization angle  $\Theta_i$  of each island, and their total size  $L$ . It might also depend on the roundness  $\rho$  and orientation  $\Phi_i$  of each island with respect to their common axis, though to a lesser degree because  $\rho$  and  $\Phi_i$  do not influence the volume or distance between the two islands as significantly as  $L$  or  $d$ .

### 4.1 Interaction energy

#### 4.1.1 Without biaxial anisotropy

In order to investigate the interaction energy, and the interaction energy only, the islands should be chosen such that their anisotropy is minimal. This can be achieved by choosing the roundness  $\rho$  for which the energy barrier is closest to zero. For an island with size  $L = 100$  nm, the energy barrier is minimal for  $\rho = 0.49$ .

Fig. 19 shows the energy landscape for two adjacent  $(\rho, L) = (0.49, 100 \text{ nm})$  islands with their centers spaced  $d = 128$  nm apart, as a function of their magnetization angles. There are 4 distinct equilibria in this figure, if one makes abstraction of global rotations and symmetries:  $(\Theta_1, \Theta_2) = (0^\circ, 0^\circ), (0^\circ, 180^\circ), (90^\circ, 90^\circ)$  and  $(90^\circ, 270^\circ)$ . The lowest energy configuration is that where both islands are magnetized in the same direction along their common axis,  $(\Theta_1, \Theta_2) = (0^\circ, 0^\circ)$ . Conversely, the highest energy occurs for opposite magnetization along this common

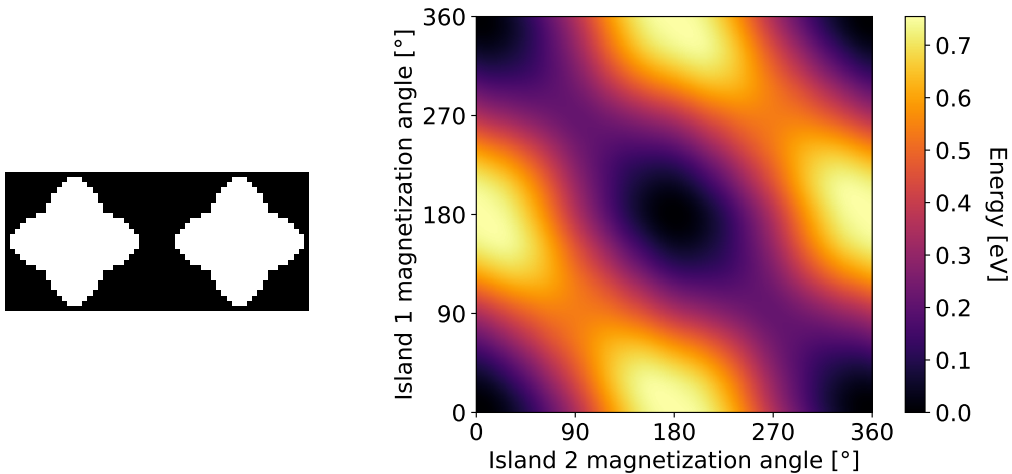


**Figure 19** – Case without biaxial anisotropy. **Left:** geometry for two  $(\rho, L) = (0.49, 100 \text{ nm})$  islands spaced 128 nm apart, with 4 nm grid. Corresponding  $E_{\text{barrier}} = 5.1 \text{ meV}$ . **Right:** interaction energy as function of the magnetization angle of each island.

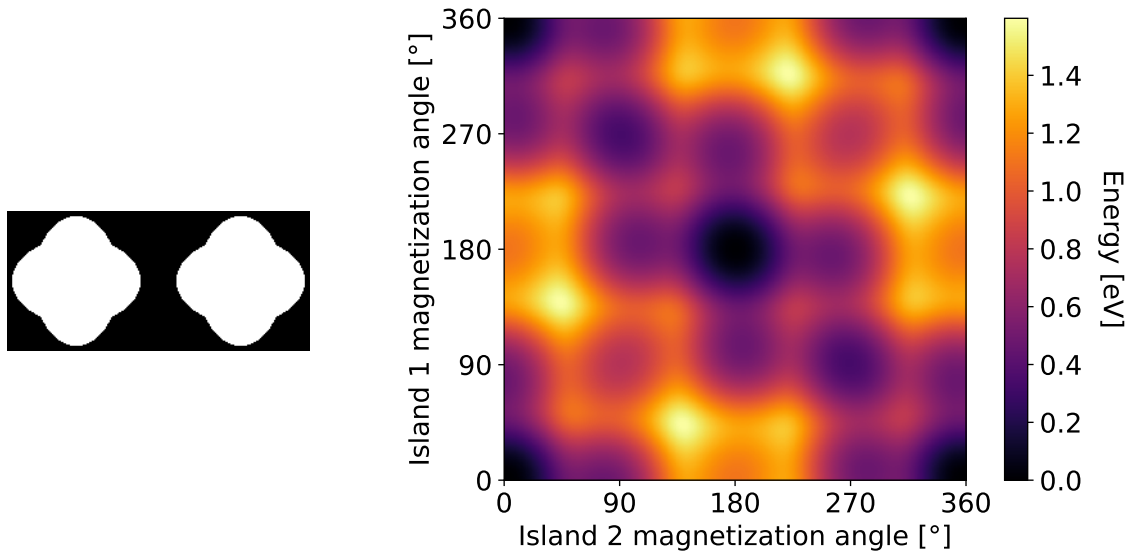
axis,  $(\Theta_1, \Theta_2) = (0^\circ, 180^\circ)$ . The two other equilibria are saddle points, corresponding to two distinct situations where both islands are magnetized perpendicularly to their common axis. The one with lowest energy of these two has the two islands oppositely magnetized,  $(\Theta_1, \Theta_2) = (90^\circ, 270^\circ)$ , while the case with parallel magnetizations  $(\Theta_1, \Theta_2) = (90^\circ, 90^\circ)$  has higher energy. On a similar note, the energy landscape teaches us that switching between global energy minima preferably occurs by simultaneously rotating the magnetization of the two islands in opposite directions.

In summary, two islands prefer a parallel magnetization along their common axis, as one would expect for two dipoles. The anti-parallel configuration perpendicular to their common axis is an unstable equilibrium with higher energy.

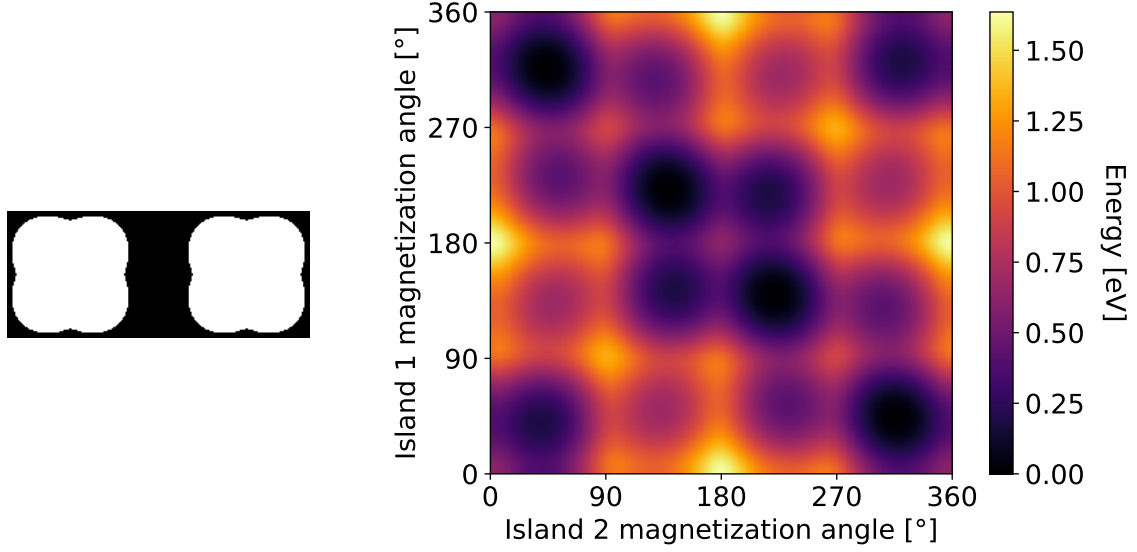
#### 4.1.2 With biaxial anisotropy

Fig. 20 shows the total energy of two interacting islands, but now with nonzero shape anisotropy. To make the contribution of this shape anisotropy to the energy landscape as clear as possible, a geometry with high barrier ( $\rho = 0.66$ ) was chosen. Numerically, a smaller grid also results in a larger energy barrier, so a cell size of 1 nm was used. As one would expect, this anisotropy superposes a sinusoidal pattern with period  $90^\circ$  in the figures, in both the vertical and horizontal directions, thus creating 16 local minima and maxima. Due to the anisotropy, the configuration with anti-parallel magnetization perpendicular to the common axis, which was previously a saddle point in the energy landscape, is now a stable local energy minimum.

As compared to the case without anisotropy, one would expect the total height of the energy landscape to at most increase by double the energy barrier for a single island, i.e. 705.2 meV, because the anisotropy of the two islands can add up at certain points in the figure. However,



**Figure 20** – Case with biaxial anisotropy. **Left:** geometry for two  $(\rho, L) = (0.66, 100 \text{ nm})$  islands spaced 128 nm apart, with 1 nm grid. Corresponding  $E_{\text{barrier}} = 352.6 \text{ meV}$ . **Right:** interaction energy as function of the magnetization angle of each island.



**Figure 21** – **Left:** geometry for two  $(\rho, L) = (0.66, 100 \text{ nm})$  islands spaced 128 nm apart, both rotated over  $\Phi = 45^\circ$ , with 1 nm grid. Corresponding  $E_{\text{barrier}} = 419.3 \text{ meV}$ . **Right:** interaction energy as function of the magnetization angle of each island.

the height of the energy landscape has increased more than this, as can be seen by comparing the colorbar on the right hand side of Figs. 19 and 20. This can be explained by the fact that, for a  $\rho = 0.66$  geometry, the volume of the islands is larger than for a  $\rho = 0.49$  geometry. The increase in energy caused by this additional volume will also be significantly larger the closer this additional volume is to the other island.

Fig. 21 shows the energy landscape of two interacting islands rotated over  $\Phi = 45^\circ$ , yielding the geometry on the left of the figure. If one rotates the islands, their anisotropy axes will rotate as well, manifesting itself in the figure as a translation of the sinusoidal pattern. These rotated islands have a different energy barrier (419.3 meV) compared to their non-rotated counterparts (352.6 meV), due to the different orientation of the numerical grid with respect to the geometry of the islands. As was already suggested in the introduction, this geometry can be used as a balanced nanomagnetic logic chain due to its high degree of symmetry. In the energy landscape, there are four identical global minima, along  $\Theta_1 + \Theta_2 = 360^\circ$ . Thus, it is energetically favorable for the magnetization of two adjacent islands to be equal to each other, but mirrored over the horizontal axis ( $\nearrow \searrow$ ,  $\nwarrow \swarrow$ ,  $\swarrow \nwarrow$ ,  $\searrow \nearrow$ ). By extending the chain, the magnetization of the first and third island will be equal, such that the geometry successfully transmits the input magnetization if the chain consists of an odd number of islands.

## 4.2 Distance dependence

When halving all dimensions of the simulation, like cell size, inter-island distance, and island size, the energies also approximately halve, as observed from Fig. 22. In this figure, the energy difference between the states  $(\Theta_1, \Theta_2) = (0^\circ, 0^\circ)$  and  $(0^\circ, 180^\circ)$  is shown as a function of the distance between the two islands, and this for two identical but scaled geometries as listed in the legend. For two magnets at a large distance from each other, it is known [56] that the force  $F \propto V^2/d^4$ , and since  $F = \partial E / \partial x$  it follows that

$$E \propto V^2/d^3. \quad (32)$$

This is exactly the behavior that is seen in the figure. When halving all dimensions, the volume  $V$  becomes 4 times smaller because the thickness of the islands is kept the same, and  $d$  halves as well. Thus, according to Eq. (32), the energy  $E$  will be halved, as is observed in the figure. For small distances, this relationship is not exactly half, because the magnetization of the smaller island has less room to settle itself to the geometry, under influence of the field of the other island, as the exchange length is the same for both situations and is thus not scaled.

For both values of  $L$ , a  $1/d^3$  fit is drawn as a dotted line, which coincides with the data at  $d/L = 4$  to ensure a correct energy scale for this fit. As the distance  $d$  is measured between the centers of the islands, a normalized distance  $d/L = 1$  corresponds to two touching islands. For such small distances, the approximation of Eq. (32) is no longer applicable, as the two islands no longer appear to each other as point particles, and the  $1/d^3$  fit significantly deviates from the true relationship. Due to the exchange energy working at very small distances, the energy for  $d/L = 1$  is significantly higher than for all higher values of  $d/L$ .

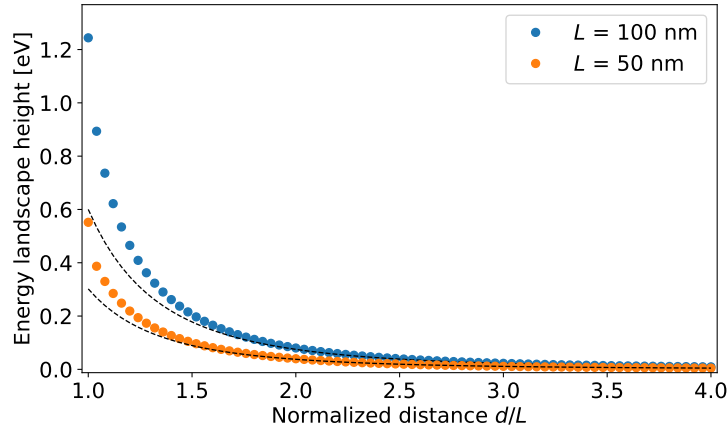


**Figure 22** – Energy difference between the states  $(\Theta_1, \Theta_2) = (0^\circ, 0^\circ)$  and  $(0^\circ, 180^\circ)$ , as a function of the normalized distance  $d/L$  between the two  $\rho = 0.49$  islands, for two different island sizes  $L$  as listed in the legend. The dotted lines indicate an ideal  $1/d^3$  relationship.

## 5 Half adder

A half adder is a logic gate which adds two binary input bits, and therefore yields two bits as output. The truth table of a binary half adder is given in the left half of Table 5. Because both input and output are represented by two bits, it could be advantageous to realize a half adder using biaxial nanomagnets, as a single biaxial island has 4 stable states and can thus represent exactly two bits of information. As such, a half adder realized with biaxial nanomagnets only has one input island and one output island. The truth table of a half adder, now in the quaternary numeral system inherent to biaxial nanomagnets, is shown in the right half of Table 5. The use of biaxial nanomagnets will require us to work with the quaternary version of the truth table from now on. In this quaternary system, the meaning of a half adder as being an ‘adder’ is no longer as clear, though this meaning is still relevant as it can easily be recovered by returning to the binary counting system.

**Table 5** – Truth table for a half adder, both in binary and quaternary numeral systems. In the binary case, the first output bit is referred to as ‘carry’, the second as ‘sum’.

Binary		Quaternary	
Input	Output	Input	Output
00	00	0	0
01	01	1	1
10	01	2	1
11	10	3	2

### 5.1 Nanomagnetic half adders

When designing a logic gate using nanomagnets, one always has to define the meaning of each magnetization direction. For biaxial nanomagnets, there are four directions which have to be assigned a number from 0 to 3. There are 24 possible ways to do this: for the first direction there are four numbers to choose from, for the second there are three, for the third only two, and for the fourth direction only one possible number remains. We will refer to such a choice as the ‘*quaternary convention*’. We will always list the quaternary convention in the form  $(0^\circ, 90^\circ, 180^\circ, 270^\circ)$ , assuming the geometry of a single island is that of Fig. 9, with the angles defined in the usual anticlockwise manner with  $0^\circ$  corresponding to a magnetization to the right. A given geometry of nanomagnets, with given input and output islands, will only behave as a half adder for at most one quaternary convention. When choosing a different input or output island, the relevant quaternary convention may be different, or even nonexistent if no half adder is possible for that particular choice of input and output islands. Thus, given a geometry of  $N$  free nanomagnetic islands, i.e. whose magnetization direction is not fixed, there are  $N$  possible choices for the input island,  $N - 1$  remaining choices for the output island, and for each combination of input and output there are 24 possible quaternary conventions to try. Only a select few, if any, of these  $24N(N - 1)$  possible combinations will correctly give the geometry the meaning of a half adder. Note that this assumes the same quaternary convention for the

input and output, which is not explicitly necessary, but eliminates unnecessary problems that will occur for larger circuits, where the output of one half adder must be passed on to the input of the next gate.

A given geometry, for a certain choice of input and output island, is said to function as a half adder if there exists a quaternary convention where, for each of the 4 possible input magnetization angles, the lowest energy state has the logically correct output magnetization angle. If this is the case, one can use the half adder for a forward calculation: when fixing the input, the lowest energy configuration will have the correct orientation of the output magnetization. Note that this is not sufficient for the gate to be usable for a reverse calculation; for this, a balanced geometry is necessary, meaning that all of these 4 ground states have equal energy, making them equally likely to occur.

Take as an example Fig. 23, which will soon be discussed in more detail, where the blue island to the left represents the input, and the red island to the right represents the output. The geometry shown there functions as a half adder according to the quaternary convention  $(0, 2, 1, 3)$ . If the input is at  $0^\circ$ , which according to the convention corresponds to the quaternary number 0, the lowest energy configuration for the output is also at  $0^\circ$ , which again represents 0. For the input at  $90^\circ$ , here representing the quaternary number 2, the output is at  $180^\circ$ , representing 1. These are the first and third lines of the truth table 5. The other two logical statements from the truth table are also fulfilled, as can be confirmed from the same figure.

Table 6 shows the magnetization directions of the input and output for the 6 quaternary conventions for which  $0^\circ$  represents 0. The 18 remaining conventions can also be recovered from this table by rotating all directions equally by a multiple of  $90^\circ$ . This table can be used to quickly verify if a certain choice of input and output island can function as a half adder, once the magnetization angles of the lowest energy states of a geometry are known. To understand this table, let us take as an example the same quaternary convention  $(0, 2, 1, 3)$  from the previous paragraph. This convention is explicitly given in the third column of the output section of the table. The convention of this column states that a magnetization angle of  $90^\circ$  corresponds to 2. Thus, the second row in this column corresponds to 2 as an input. For a quaternary half adder, the output should then be 1. For the convention of this column, 1 should be represented by an angle of  $180^\circ$ , which is indeed the output direction shown in the second row of the  $(0, 2, 1, 3)$ -column.

**Table 6** – Magnetization directions corresponding to quaternary conventions for which  $0^\circ$  represents 0. The other conventions can be recovered by rotating all directions equally by a multiple of  $90^\circ$ .

Input	Output for quaternary convention					
	$(0, 1, 2, 3)$	$(0, 1, 3, 2)$	$(0, 2, 1, 3)$	$(0, 2, 3, 1)$	$(0, 3, 1, 2)$	$(0, 3, 2, 1)$
$\rightarrow$	$\rightarrow$	$\rightarrow$	$\rightarrow$	$\rightarrow$	$\rightarrow$	$\rightarrow$
$\uparrow$	$\uparrow$	$\uparrow$	$\leftarrow$	$\downarrow$	$\downarrow$	$\leftarrow$
$\leftarrow$	$\uparrow$	$\downarrow$	$\leftarrow$	$\uparrow$	$\leftarrow$	$\downarrow$
$\downarrow$	$\leftarrow$	$\uparrow$	$\uparrow$	$\downarrow$	$\leftarrow$	$\downarrow$



Also, it is necessary to include at least one island whose magnetization direction is permanently fixed, in order to break the symmetry. This is because a nanomagnetic system is invariant under a global magnetization reversal [6]; the energy associated with a certain magnetization configuration is exactly equal to the energy of that same configuration but with all magnetizations reversed. If one would not include a fixed island, the half adder would be ill-defined and would allow for multiple quaternary conventions for the same in- and output islands.

## 5.2 Gate design

In order to gain a more intuitive understanding of the states of a half adder and what they mean for the magnetization direction, to conceive a simple geometry that can be interpreted as a half adder, it is instructive to reformulate the half adder truth table 5 into three basic rules:

1. There must be exactly two inputs for which input and output are equal. In the truth table this is  $0 \rightarrow 0$  and  $1 \rightarrow 1$ .
2. Exactly two inputs must both yield the same output. For one of these, the input must also be equal to the output, as in rule 1. In the truth table this is  $1 \rightarrow 1$  and  $2 \rightarrow 1$ .
3. For the final remaining input, the input and output must be different and unique, i.e. not encountered in the previous rules. In the truth table this is  $3 \rightarrow 2$ .

The first and second rules are quite straightforward, and form the basis for the reasoning behind the simplest biaxial half adder which will be discussed in this section. The third rule is quite

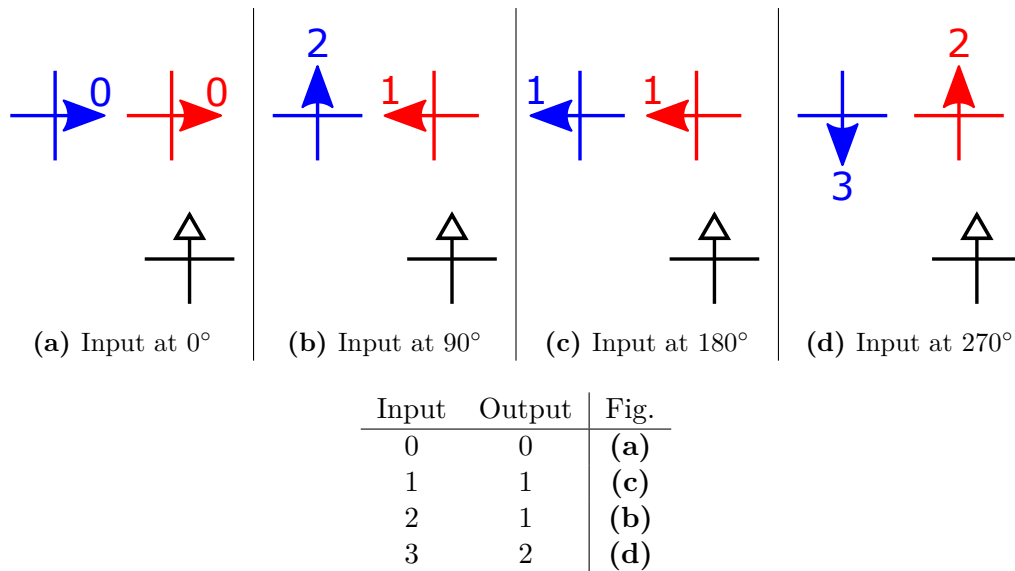


**Figure 23** – Lowest energy configurations for all four possible input magnetizations, after relaxation to a local energy minimum. This functions as a half adder with quaternary convention (0, 2, 1, 3). Islands with a filled arrowhead can move their magnetization freely to achieve the lowest energy. Islands with an open arrowhead have their magnetization permanently fixed in the direction of the arrow. The blue island is the input island, the red island functions as the output.

complicated, and is thus not easily used when one tries to design a half adder geometry. It should rather be used to confirm the functioning of a half adder geometry once such a geometry seems promising.

From the discussion in Section 4.1 about the interaction between two islands, we know that two islands aligned along their hard axes preferably orient their magnetizations in the same direction along their common axis (cfr. the energy landscape from Fig. 20). This property can be exploited to fulfill the first rule of a half adder, i.e. there must be exactly two inputs for which the input and output lay in the same direction. So, two axis-aligned free islands form the basis of the half adder geometry. In the following, we will always place these two islands with their centers 128 nm apart, such that there is 28 nm of free space between them. One of these two islands will be considered the input, the other the output. The first rule has already shown that it is instructive to define  $0^\circ$  as 0 and  $180^\circ$  as 1, or vice versa. For the other two possible inputs, namely those perpendicular to the islands' common axis, the output preferably orients itself in the opposite direction as the input, such that indeed there are exactly only two inputs for which input and output lay in the same direction. Thus, the first rule of the half adder is fulfilled.

What is left to do now, is to break the symmetry to fulfill the second and third rules, by placing a fixed island near the two free islands. Practically, a fixed island can be manufactured by making use of exchange bias as described in Section 1.3. What we want, is that for one of the remaining inputs, which are perpendicular to the two islands' common axis, the output is parallel to this common axis, to fulfill rule 2 which states that exactly two situations must have the same output direction. This can be achieved by placing the fixed island perpendicular to the free islands' common axis, facing towards the output island, as shown schematically in Fig. 23. This prevents the output island from having its magnetization pointing down, and will hence preferably point horizontally. To make the magnetization consistently choose either left or right, the fixed island is placed slightly off-center from the output's vertical axis. For example, in the figure the fixed island was placed slightly off to the right, such that the output slightly prefers a left magnetization over a right magnetization.

The third rule states that the output for the final remaining input must not be in the same direction as its input, and must also not be in any of the previous output directions, so not horizontal. As such, in this case it is allowed and even useful for this to be perpendicular to the free islands' common axis, because the magnetizations will align anti-parallel. The fixed island does not impede this whatsoever, on the contrary, the output is even encouraged into this correct orientation, such that also this third rule is readily satisfied. The lowest energy configuration for each of the 4 possible inputs is shown in the schematic representation of Fig. 23.

The typical geometry of this kind of half adder is shown in Fig. 24. The definition of the parameters  $s$  and  $d$  is also given in this figure:  $s$  is the horizontal displacement of the fixed island, while  $d$  is the vertical distance between the center of the fixed island and the center of the rightmost free island. The sign of  $s$  and  $d$  is defined in the usual mathematical manner, e.g. both  $s$  and  $d$  are negative when the fixed island is to the lower left of the rightmost free island.

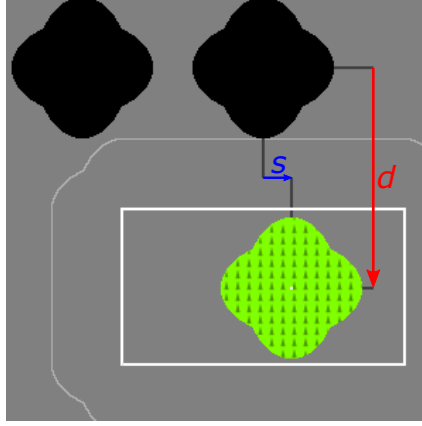


**Figure 24** – Typical geometry of the half adder under discussion, with  $(\rho, L) = (0.66, 100 \text{ nm})$  islands. The magnetization of the green island is permanently fixed at  $90^\circ$ . The black islands are free. The white rectangle indicates the range of the center of the green island, as examined in Fig. 25 and 26. The thin grey line shows the farthest outline of the fixed island when moving its center throughout the white rectangle. The definition of  $s$  and  $d$  is also given.

### 5.3 Simulation methods

Once a geometry has been found, it has to be validated using a numerical solver like `mumax3` to confirm that it can actually function as a half adder. In the simplest case, all islands are assumed to have the same roundness  $\rho$ , size  $L$ , and orientation  $\Phi_i$ , where each island is defined by its position  $(x, y)$  and saturation magnetization  $M_{\text{sat}}$ , and whether its magnetization is fixed or not. Each island has four stable magnetization angles, and a general geometry contains  $N$  free islands, such that there are in total  $4^N$  possible configurations of the magnetization of all islands together.

The `mumax3` simulation procedure then proceeds as follows. Each island is initialized with its magnetization in one of its four stable directions. Then, the whole geometry is relaxed through the `relax()` command to a local energy minimum. The result of this relaxation is then the information  $(\{\widetilde{\Theta}_i, \forall i = 1 \dots N\}, E)$ , giving the relaxed magnetization angle of all islands, and the total energy of that relaxed configuration. This is performed for all  $4^N$  possible combinations of initial magnetization directions. It is important that the relaxed magnetization angles are recorded, and not the initial ones, because it is possible that the magnetization of an island rotates significantly during the relaxation process, for example when neighboring islands are initialized in different directions.

The data is then searched for a half adder. For this, each island is once considered as a possible input island. For each of the 4 stable magnetization angles of the input island, the lowest energy configuration of the other islands is determined from the data. Each other island is then checked if it can represent the output for any of the 24 possible quaternary conventions. If at least one combined choice of input island, output island, and quaternary convention gives a logically correct behavior, a functioning half adder has been found.

When assessing the balancedness of a half adder, the symbol  $E_{\alpha,i}$  will be used. This rep-

resents the  $i$ -th lowest energy for which the input magnetization is at an angle  $\alpha$ , out of all possible magnetization configurations of the other islands. The four ground state energies that can be used for a forward calculation are thus symbolically represented as  $E_{\alpha,0}$  where  $\alpha \in \{0^\circ, 90^\circ, 180^\circ, 270^\circ\}$ , if the easy axes of the input island are horizontal and vertical.

## 5.4 Varying fixed island parameters

The position  $(s, d)$  of the fixed island will now be varied, as well as its saturation magnetization  $M_{\text{sat}}$ , to determine regions where the geometry correctly functions as a half adder, and to then find a position where the geometry is as balanced as possible. First,  $s$  and  $d$  will be varied in the region below the free islands as illustrated by the white rectangle in Fig. 24. This range holds true to the initial reasoning presented earlier, and will reveal some symmetries. Later on, a similar treatment will be given for the region near the common axis of the free islands, as in Fig. 30, which will yield more balanced half adders capable of reverse calculation, but less suited for forward calculation.

### 5.4.1 Fixed island far from the common axis

The results of varying  $s$  from  $-100$  nm to  $100$  nm and  $d$  from  $-100$  nm to  $-210$  nm are shown in Figs. 25 and 26. This range is indicated as the white rectangle in Fig. 24. We will first explain the different colors in these figures, and only later discuss the brightness of these colors. The colored regions in these figures, surrounded by black contours, are the regions where the position of the fixed island is such, that the geometry correctly functions as a half adder. The different colors, viz. blue, red, yellow and green, indicate what the correct quaternary convention is for that specific set of  $s$  and  $d$ , as well as which of the two free islands is chosen as the input island; ‘In L’ indicates that the leftmost free island is considered the input island, and ‘In R’ for the rightmost free island. Note that there exists a region where both the red and yellow conventions are correct.

### Regions with different quaternary conventions

The blue region corresponds to the quaternary convention and choice of input island as it was conceived initially, which was shown schematically before in Fig. 23.

A first observation can be made by comparing the conventions of the red and blue regions. They both define the leftmost island as the input, and their quaternary conventions are nearly equal, the only difference being that their definition of 0 and 1 is opposite. This is because the definition of 1 is determined by which of the two horizontal directions is preferred by the output island when the input is 2, which for both conventions is at  $90^\circ$ . This depends on the horizontal position of the fixed island. If the fixed island is placed more to the left, the magnetization of the rightmost free island will be more inclined to point to the right. This explains why the red and blue regions are nearly identical, and separated near the  $s = 0$  line.

The blue region does, however, extend a bit to the left of the  $s = 0$  line. This is because the fixed island is to the bottom right of the leftmost free island, such that the magnetization of the leftmost island has a slight tendency to point to the left, due to the dipolar field interaction with the fixed island. As such, if the fixed island is placed directly underneath the rightmost free

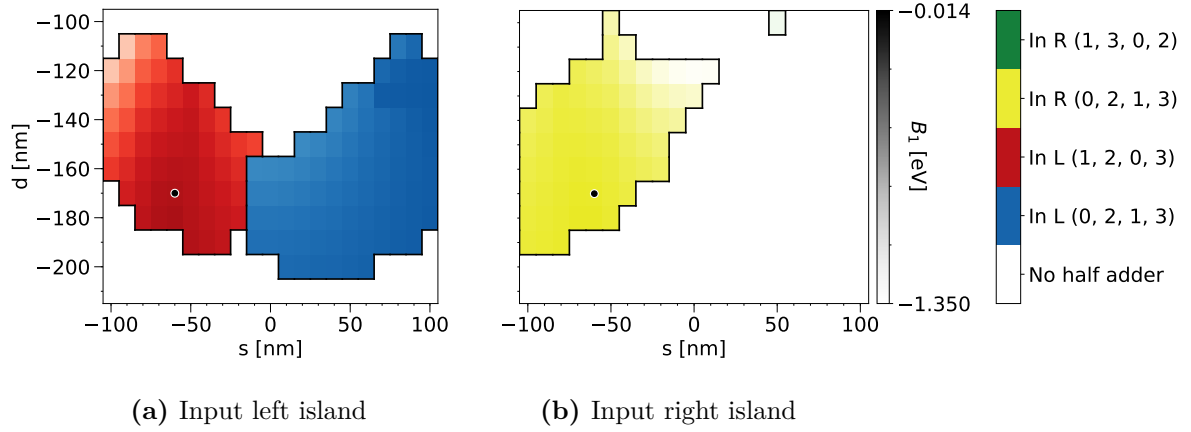


**Figure 25** – Regions where the geometry, with the fixed island at position  $(s, d)$  with respect to the rightmost island, functions as a half adder according to the quaternary conventions indicated by the color.  $M_{\text{sat}} = 800 \text{ kA m}^{-1}$  for all islands. The brightness represents the balancedness metric  $B_1 = \min_{\alpha}(E_{\alpha,1}) - \max_{\alpha}(E_{\alpha,0})$  (darker is better). The black dot indicates the position of the fixed island for Figs. 27 and 28.

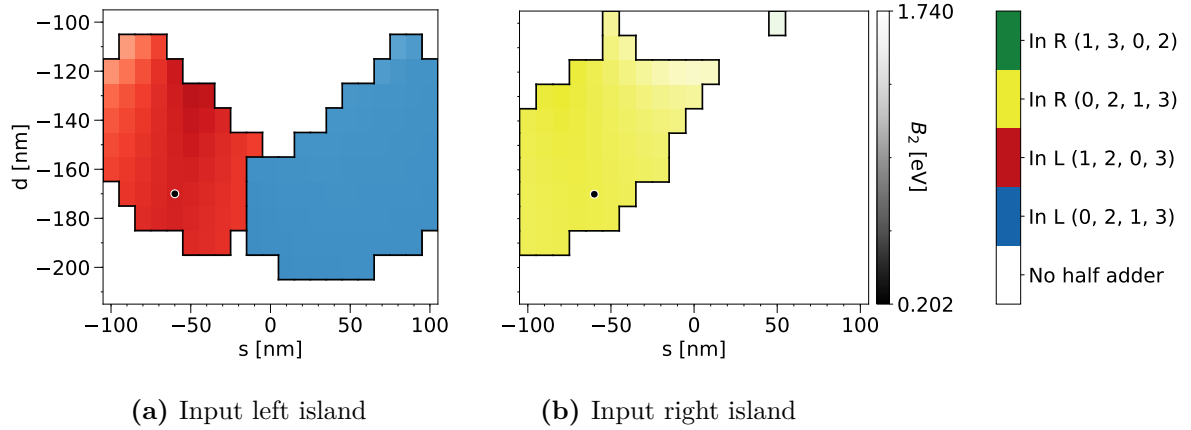


**Figure 26** – Regions where the geometry, with the fixed island at position  $(s, d)$  with respect to the rightmost island, functions as a half adder according to the quaternary conventions indicated by the color.  $M_{\text{sat}} = 800 \text{ kA m}^{-1}$  for all islands. The brightness represents the balancedness metric  $B_2 = \max_{\alpha}(E_{\alpha,0}) - \min_{\alpha}(E_{\alpha,0})$  (darker is better). The black dot indicates the position of the fixed island for Figs. 27 and 28.

island, this rightmost island will still have a preference for its magnetization to point to the left. This explains why the blue region extends to negative  $s$ -values, before transitioning to the red region. If the leftmost free island would not exist, and the fixed island would be placed directly below the rightmost free island, the free island would not have a preference for its magnetization to point left or right.

For both the red and blue region, there is an upper and lower limit for  $d$ . For  $d > 200$  nm, the fixed island is too far away for the geometry to function as a half adder. The entire functioning of the half adder, as it was initially conceived, rests on the fixed island preventing the rightmost island from having an average magnetization angle near  $270^\circ$ , but rather horizontal at  $0^\circ$  or  $180^\circ$ . As it turns out, for  $(\rho, L) = (0.66, 100$  nm) islands with a saturation magnetization  $M_{\text{sat}}$  of  $800 \text{ kA m}^{-1}$ , the center of the fixed island should not lay further than 200 nm away from the common axis of the two free islands. Conversely, there also exists a lower limit: the fixed island must not lay too close to the free islands, because then even a horizontal magnetization becomes unfavorable.

When comparing the yellow and red regions, a symmetry can be observed. In the yellow region, the rightmost island is considered the input island, which is opposite to the definition in the red region. Taking a look at their quaternary conventions, it is clear that they are each other's horizontally mirrored counterpart: the definitions of 0 and 1, corresponding to the horizontal directions  $0^\circ$  and  $180^\circ$ , are oppositely defined between the yellow and red conventions. This is because the entire geometry is symmetrical when the fixed island is placed at  $s = -64$  nm, because the centers of the two free islands are spaced 128 nm apart. The reason why Fig. 25 is not perfectly symmetrical about the  $s = -64$  nm axis, is because this figure was calculated for a range of  $s$  with steps of 10 nm. It is reasonable to assume that there will then also exist a mirrored counterpart for the blue region at even lower values for  $s$ . All these regions will also have a vertically mirrored counterpart for positive values of  $d$ .

### Balancedness as a function of fixed island position

We will now turn our attention to the brightness of the colors in the figures. Both in Fig. 25 and Fig. 26, there is a greyscale colorbar, representing a different quantity for either figure. These quantities are different metrics to assess the balancedness of a half adder, based on the different energy levels of different input magnetizations. The first metric that can be used to assess the balancedness, is the energy difference between the highest ground state and the lowest first excited state, given by  $B_1 = \min_{\alpha}(E_{\alpha,1}) - \max_{\alpha}(E_{\alpha,0})$ . The meaning of  $E_{\alpha,i}$  was already given: it is the  $i$ -th lowest energy level for which the input magnetization is at or near an angle  $\alpha$ . If one wants to use the half adder for a reverse calculation,  $B_1$  should be positive. This would mean that the energies of all the correct ground states are lower than the energies  $E_{\alpha,i \neq 0}$  of all the incorrect states. As such, when operating the half adder thermally, the correct states will have a higher probability of occurring than the incorrect ones, which allows to discriminate between correct and incorrect states in a purely statistical manner.

Ideally, for a perfectly balanced logic gate, the ground state energies for each of the 4 possible magnetization angles of the input island should be equal. The degree to which this condition is fulfilled is represented by the second metric  $B_2 = \max_{\alpha}(E_{\alpha,0}) - \min_{\alpha}(E_{\alpha,0})$ : the energy difference

between the highest and lowest of the 4 ground states, which is always positive. If this is zero, the half adder is perfectly balanced. The higher  $B_2$ , the less balanced the half adder is. Hence, in the greyscales of the figures, the most balanced half adders are the darkest, and the least balanced ones the brightest. When searching for a half adder suitable for reverse calculation, the most important metric at first is  $B_1$ . Once  $B_1$  is positive, one can assess  $B_2$ , which should be minimal.

Fig. 25 shows the first metric  $B_1$ . Unfortunately, the first metric is always negative in the examined range where the fixed island is placed far from the common axis of the free islands, such that none of these half adders can be used for a reverse calculation. The optimal values do come close to zero, though, especially near  $s = -60$  nm and  $d = -170$  nm, for the red half adder with the leftmost island as input. For these values, the fixed island is to the bottom left of the output island. The energy levels corresponding to the red half adder at these coordinates are explicitly shown in Fig. 27. In this figure, the energy levels are grouped by input. The angle in the text box of each energy level represents the output magnetization responsible for that energy level. This figure can make the meaning of balancedness a bit more clear. The highest ground state in this case is for a  $270^\circ$  input, while the lowest first excited state  $E_{180^\circ,1}$  is the one for a  $180^\circ$  input with  $90^\circ$  output. This incorrect output has a lower energy than the correct output for the  $270^\circ$  input, as clarified by the dotted lines extending horizontally.

Some other observations can also be made from these energy levels. Firstly, the energy levels for the input at  $90^\circ$  are much more closely spaced than for other inputs. This is because the entire functioning of the half adder rests on the fixed island preventing this input from having its output pointing down. This means the geometry can not relax as it normally would, such that the energies are all pushed together. If the fixed island would be placed even further, the  $270^\circ$  level would fall below the  $0^\circ$  level, and the geometry would no longer function as a half adder. This was already remarked from the extent of the red and blue regions in Fig. 25. Secondly,  $E_{0^\circ,2}$  corresponding to an output at  $180^\circ$ , has a higher energy than  $E_{180^\circ,3}$  corresponding to an output at  $0^\circ$ . This is for the same reason which has been brought up a few times already; the island prefers a magnetization away from the fixed island. Finally, it can be remarked that there are some inputs which have less than four energy levels. This is because the combination of magnetization angles corresponding to the absent energy levels is not stable. During the relaxation, the magnetization of an island can rotate over more than  $90^\circ$  to reach an energy minimum. As such, multiple initial configurations can reach the same energy minimum, reducing the total number of energy levels in the figure.

We now return to Fig. 26, which shows the second metric  $B_2$  in its greyscale. Since the first metric is negative everywhere in the  $(s, d)$ -region of the figure, these half adders can not be used for reverse calculation. Forward calculation is still possible for any of the colored regions, and the second metric shows how well-suited a certain choice of  $s$  and  $d$  is for this purpose. This is because, if one of the ground states is lower in energy than another, there is a chance that this particular logical state will be favored when multiple half adders are put in series. The global input of such a larger circuit will be fixed, but the half adders deeper in this circuit will take the outputs of other half adders as input. As such, if a certain input has a much lower ground state energy than another, this input will be favored, and due to the two-way flow of information this

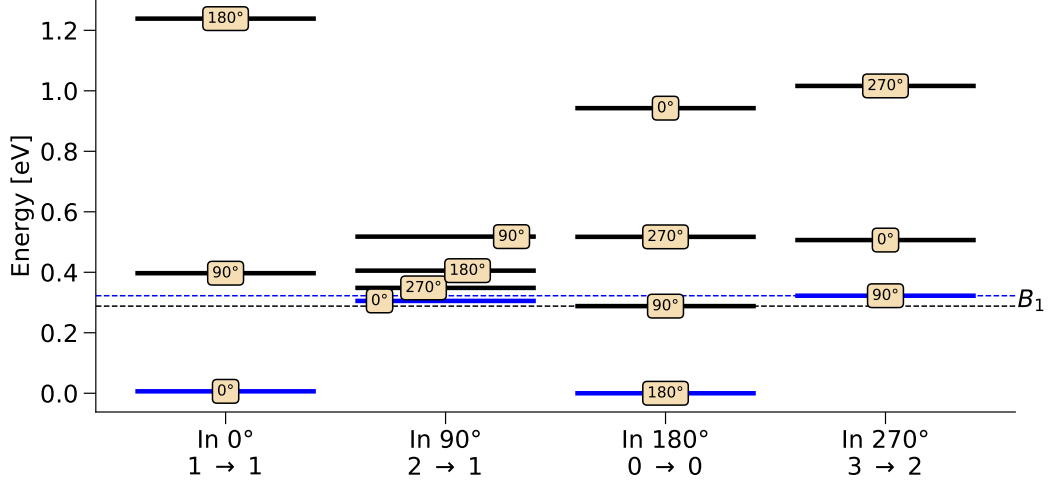


**Figure 27** – Energies of different stable magnetization configurations, grouped by input magnetization angle, for a half adder with  $d = -170$  nm and  $s = -60$  nm, the leftmost island as input, and  $M_{\text{sat}} = 800 \text{ kA m}^{-1}$  for all islands. The orientation of the output island is shown in the text box for each energy level. The lowest energy level for each input is indicated in blue. The quaternary convention, dictated by these energy levels, is given at the bottom: the number before the arrow gives the input for that column, the number after the arrow the output for the lowest energy level of that column.

preference will affect the likelihood of the outputs of earlier gates in the circuit. So, the closer all the ground state energies of a single half adder are, the more gates can be put in series.

Hence,  $B_2$  is preferably as close to zero as possible. The best values are therefore near  $s = -50$  nm and  $d = -130$  nm, so it is best to use those values for a forward-calculating half adder of this type. The blue region does not show a lot of variation and has a rather high value of  $B_2$  everywhere, and can thus be disregarded for forward calculation.

In the figures, there is also the green half adder with quaternary convention  $(1, 3, 0, 2)$ , which is the small region at  $(s, d) = (50, -100)$  nm. It is clearly not suited at all as it scores bad for both  $B_1$  and  $B_2$ . This region is also very small, which could make it difficult to reliably manufacture the corresponding geometry. Therefore, this region was not investigated further.

## Circuits

It can be insightful to consider a situation where multiple half adders are chained together to perform a larger forward calculation. A simple example is given in Fig. 28, where the half adders are represented in binary form. In binary form, a half adder takes two input bits and two output bits. In the schematic representation of the circuit in Fig. 28, each half adder therefore has a top and bottom in- and output bit. The quaternary interpretation of these is as follows: calling the top bit  $A$ , and the bottom bit  $B$ , the quaternary number they represent is  $A + 2B$ . This holds for each individual half adder in the circuit. For example, the leftmost half adder in the circuit from Fig. 28 performs the operation  $A_1 + 2A_2$ .



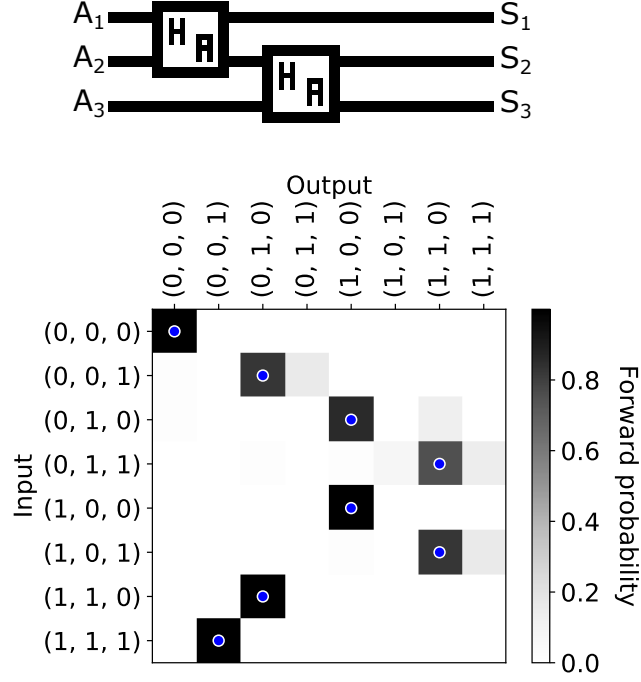


**Figure 28 – Top:** schematic representation of the logic circuit. **Bottom:** probability of each input/output combination occurring at 298 K, when fixing the input. Hence, each row adds up to a total of 1. Blue dots indicate correct combinations. Inputs are in  $(A_1, A_2, A_3)$  format, outputs  $(S_1, S_2, S_3)$ .

The bottom figure then shows the probability of each output occurring when fixing the input, at room temperature ( $k_B T = 25.8 \text{ meV}$ ). When increasing the temperature, or equivalently if one scales down the geometry causing the associated energies to decrease, the probability of getting an incorrect output becomes higher.

Let us now take the  $(A_1, A_2, A_3) = (0, 0, 1)$  input as an example. The most probable  $(S_1, S_2, S_3)$  output is then  $(0, 1, 0)$ , which is binarily correct, but  $(0, 1, 1)$  also has an appreciable probability. This can be understood from the energy levels in Fig. 27. The first half adder takes the input  $A_1 + 2A_2 = 0 + 2 \cdot 0 = 0$ . As the half adder functions with the quaternary convention  $(1, 2, 0, 3)$ , the number 0 corresponds to an angle of  $180^\circ$ . For this input angle, the output with by far the lowest energy is at  $180^\circ$ , representing 0. Thus,  $S_1$  will most likely be 0, and the second half adder will almost certainly receive the input  $0 + 2 \cdot A_3 = 0 + 2 \cdot 1 = 2$ , which is at  $90^\circ$ . For an input at  $90^\circ$ , this particular half adder geometry has closely spaced energy levels, the lowest of which has the output at  $0^\circ$  (quaternary 1), closely followed by  $270^\circ$  (quaternary 3). As such, the output of the second half adder  $S_3 S_2$  is most likely 01, but also 11 has an appreciable probability because their energy levels are quite close together. As such, for the input  $(0, 0, 1)$ , the most probable global output  $(S_1, S_2, S_3)$  is  $(0, 1, 0)$ , with the second most probable outcome being  $(0, 1, 1)$ , as is confirmed by the figure showing the probabilities. Nonetheless, the most probable outcome for each input is the binarily correct output, such that two half adders of this geometry could theoretically be used in the circuit of Fig. 28.

### Varying saturation magnetization of the fixed island

Another parameter sweep was also conducted, as shown in Fig. 29, where the saturation magnetization  $M_{\text{sat}}$  and the vertical position  $d$  were varied. What is immediately apparent from this figure is that the region with functioning half adders is quite linear: the further away the fixed island is, the larger its saturation magnetization must be to remain influential enough for the gate to behave as a half adder. The red and blue regions have identical quaternary conventions, but different input islands. The blue region corresponds to the half adder as it was initially conceived. The red and blue regions start to overlap for higher  $d$ . This is understandable, because the further away the fixed island is, the more similar its field at either of the free islands. In the limit  $d \rightarrow \infty$ , both free islands are equivalent. Hence, both the red and blue conventions are valid for large  $d$ .

The sweeping of  $M_{\text{sat}}$  shows that placing the fixed island further away causes  $B_1$  to decrease. This is logical, as increasing this distance decreases the interaction between the fixed island and the free islands. In the absence of the fixed island, the two free islands have a lot of symmetry, such that there are some magnetization configurations with equal energy, meaning that  $B_1 = 0$  if the fixed island is absent. One might interpret this as the logic gate being more balanced, but this is not true, because adjusting  $M_{\text{sat}}$  of the fixed island affects all energy levels similarly. As the limit value is  $B_1 = 0$ ,  $B_1$  can not become positive, so this will not improve the balancedness.

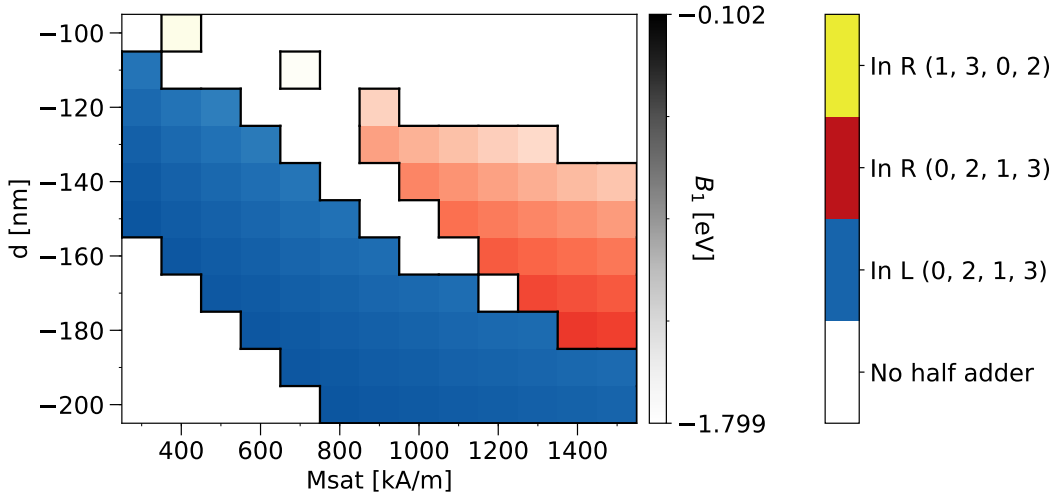


**Figure 29** – Regions where the geometry, with the fixed island at position  $(s = 20 \text{ nm}, d)$  with respect to the rightmost island, functions as a half adder according to the quaternary conventions indicated by the color. The saturation magnetization of the fixed island is changed, while for the free islands it remains at  $M_{\text{sat}} = 800 \text{ kA m}^{-1}$ . The brightness represents the first balancedness metric:  $B_1 = \min_{\alpha}(E_{\alpha,1}) - \max_{\alpha}(E_{\alpha,0})$  (darker is better).

#### 5.4.2 Fixed island near the common axis

The standard reasoning behind this type of geometry, as given in the previous section, apparently does not work for even a single reverse calculation. The question is now, whether there exists a combination of  $s$  and  $d$  for which  $B_1$  is positive. For this, a different range of  $s$  and  $d$  was examined, which places the fixed island near the common axis of the free islands. This is illustrated in Fig. 30, with the examined range  $s = 110 \text{ nm}$  to  $180 \text{ nm}$  and  $d = 0 \text{ nm}$  to  $-100 \text{ nm}$  indicated as the white rectangle.

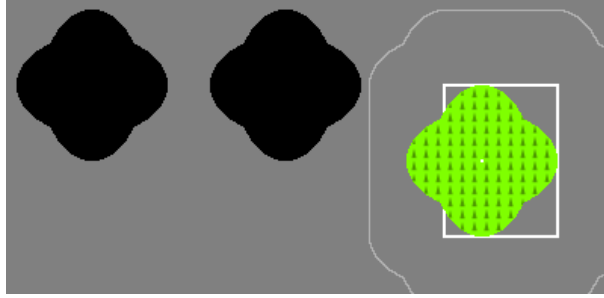


**Figure 30** – Typical geometry of the half adder with the fixed island near the common axis, with  $(\rho, L) = (0.66, 100 \text{ nm})$  islands. The magnetization of the green island is permanently fixed at  $90^\circ$ . The black islands are free. The white rectangle indicates the range of the center of the fixed island, as examined in Fig. 31 and 33. The thin grey line shows the farthest outline of the fixed island when moving its center throughout the white rectangle.

The quaternary regions inside this range are shown in Fig. 31. Note that the colors of these regions have no connection whatsoever to the quaternary conventions from the previous paragraph; the conventions observed here have not been encountered before.

For  $d = 0 \text{ nm}$ , the geometry is perfectly symmetric, such that the horizontally mirrored counterpart of the blue region, i.e. the red region, shows up at  $d \geq 0$ . The red region is the mirrored counterpart of the blue region about the  $d = 0$  line. At first sight, it might not be immediately clear why these two regions are equivalent, as the magnetization direction of the fixed island is ‘up’ for both, so they are not each other’s mirror image. However, their energy levels are the same, because the energy is invariant under a global magnetization reversal. The quaternary convention of the red region is identical to that of the blue region, but flipped horizontally. This is because a point-symmetry (the magnetization reversal) is equivalent to one vertical and one horizontal mirroring, and additionally, the red and blue geometries are each other’s vertical mirror image. The vertical mirroring therefore occurs twice, which cancels out, leaving only the horizontal mirroring which is observed in the quaternary convention.

The quaternary convention  $(0, 3, 1, 2)$  encountered here is explicitly shown in Fig. 32. It is the vertically mirrored counterpart of the previous blue region from Fig. 25, which had  $(0, 2, 1, 3)$ . This can be understood from the dipolar field of the fixed island. Previously, near the free islands, this dipolar field mainly pointed up, because the fixed island was placed below them. Now, the fixed island is more to the side, so because the dipolar field curls back on itself, the field near the free islands now points down. Hence, the quaternary convention is flipped vertically.

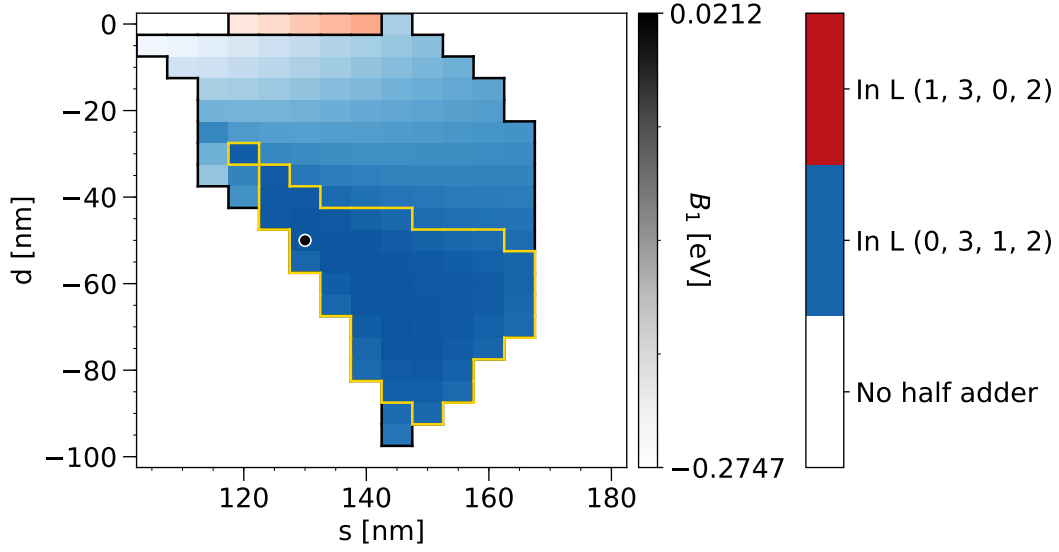


**Figure 31** – Regions where the geometry, with the fixed island at position  $(s, d)$  with respect to the rightmost island, functions as a half adder according to the quaternary conventions indicated by the color. The brightness represents the first balancedness metric:  $B_1 = \min_{\alpha}(E_{\alpha,1}) - \max_{\alpha}(E_{\alpha,0})$  (darker is better). Inside the yellow outline,  $B_1$  is positive. The black dot indicates the position of the fixed island for Figs. 34 and 35.

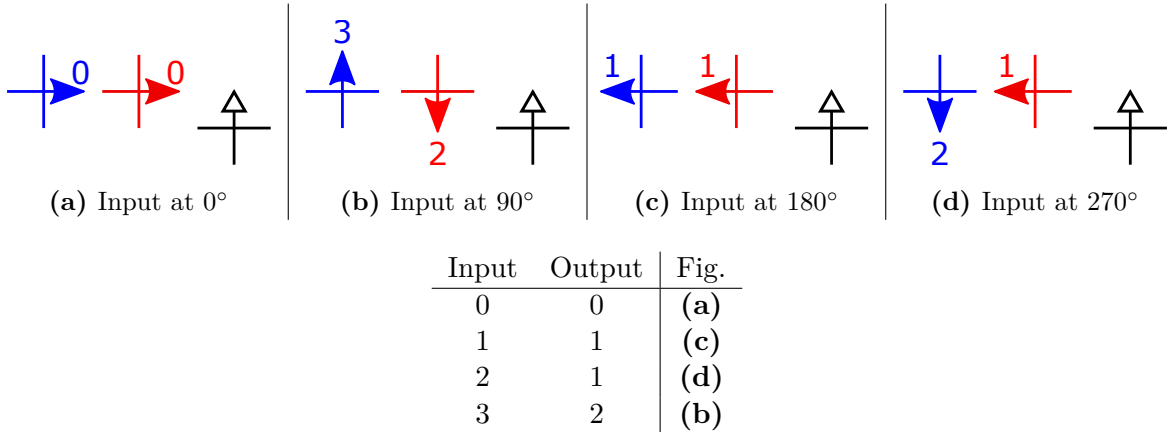


**Figure 32** – Lowest energy configurations for all four possible input magnetizations. This functions as a half adder with quaternary convention (0, 3, 1, 2). Islands with a filled arrowhead are free, island with an open arrowhead is fixed. The blue island is the input island, the red island functions as the output.

### Balancedness as a function of fixed island position

In contrast to the half adders from the previous section, there are now some values of  $(s, d)$  for which the first balancedness metric  $B_1 = \min_{\alpha}(E_{\alpha,1}) - \max_{\alpha}(E_{\alpha,0})$  is positive. This means that the gate can be used for at least one reverse calculation. The region in the  $(s, d)$ -plane where the metric is positive is also quite large, leaving a decent manufacturing error margin. One must note, however, that the maximal value for  $B_1$  here is only 21.2 meV, which is lower than room temperature  $k_B T = 25.8$  meV, so the population difference between these states will only be small.

The second balancedness metric  $B_2$  is shown in Fig. 33, and is a measure for how suitable the geometry is for a forward calculation: the lower  $B_2$ , the better. Unfortunately, the minimal value of this second metric is 0.447 eV throughout this region. For the geometries in the previous section, with the fixed island far from the common axis, this second metric could be as low as 0.205 eV. The second metric increases only slightly for decreasing  $s$  and  $d$ , with a sharp increase near the line  $3s + d = 330$  nm. Below this line, the geometry no longer functions as a half adder. So, as long as  $s$  and  $d$  are well above this line, the second metric does not vary significantly.

The optimal value of these two metrics is thus located near  $(s, d) = (130 \text{ nm}, -50 \text{ nm})$ . The energy levels for that choice of  $s$  and  $d$  are shown in Fig. 34. As the first balancedness metric is now positive, the highest ground state is below the lowest first excited state, as is observed in the figure. The margin is quite small, though, which is not ideal. Because the fixed island is located to the bottom right of the free islands, all energy levels for an output at  $0^\circ$  are shifted up, while those for  $180^\circ$  are shifted down. The shift of energy levels is greatest for an input at

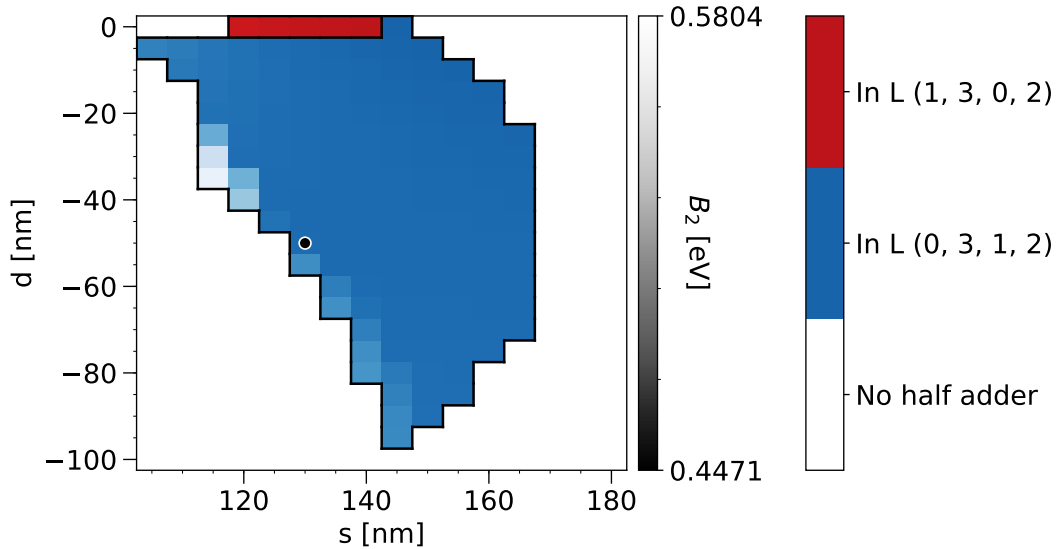


**Figure 33** – Regions where the geometry, with the fixed island at position  $(s, d)$  with respect to the rightmost island, functions as a half adder according to the quaternary conventions indicated by the color. The brightness represents the second balancedness metric:  $B_2 = \max_{\alpha}(E_{\alpha,0}) - \min_{\alpha}(E_{\alpha,0})$  (darker is better). The black dot indicates the position of the fixed island for Figs. 34 and 35.

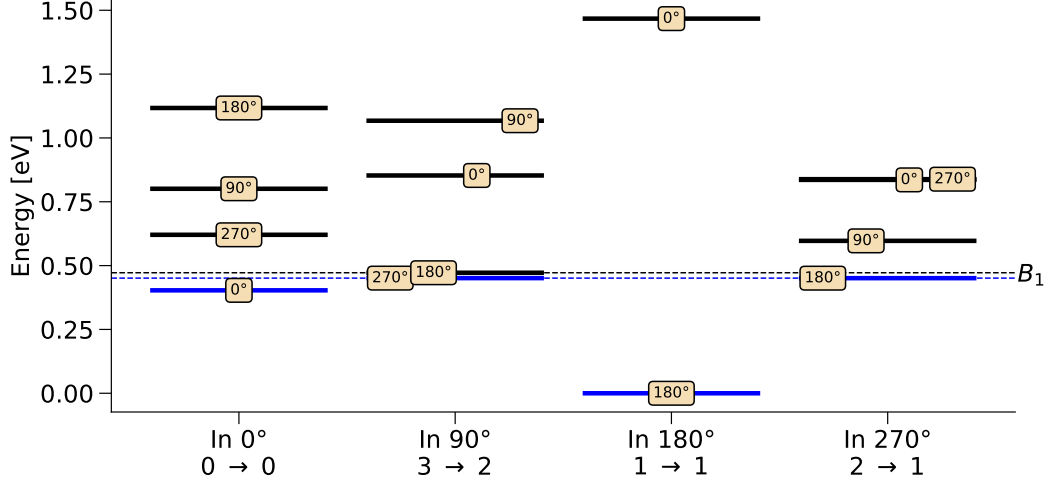


**Figure 34** – Energies of different magnetization configurations, grouped by input magnetization angle, for a half adder with  $d = -50$  nm and  $s = 130$  nm, and  $M_{\text{sat}} = 800 \text{ kA m}^{-1}$  for all islands. The orientation of the output island is shown in the text box for each energy level. The lowest energy level for each input is indicated in blue. The quaternary convention, dictated by these energy levels, is given at the bottom: the number before the arrow gives the input for that column, the number after the arrow the output for the lowest energy level of that column.

180°; there is not even a stable energy minimum for the output near 90° or 270°. It could be useful to add an additional fixed island to decrease the energy difference between the ground states.

By comparing the energy levels to those of the half adder from the previous section, where the fixed island was placed far away from the common axis, one may notice that  $\min_{\alpha}(E_{\alpha,1} - E_{\alpha,0})$  is smaller in Fig. 34. This is the minimal energy difference between a ground state and its respective first excited state, and is also a measure for how well suited the geometry is for forward calculation. The higher this value, the better, because then the thermal population of incorrect states will be lower. For this half adder, this is only 21.1 eV, while for the previous geometry this was 43.1 eV.

A reverse calculation is possible because all ground states have lower energy than any of the logically incorrect states. However, the size of such a reverse calculation is very limited. When applying an output of 1, corresponding to 180°, there should ideally be an equal probability for the input to be 1 or 2. From the energy levels, it can be seen that an input of 1 is strongly preferred, since the energy level for 1 → 1 is much lower than 2 → 1. Furthermore, the energy level for input 90° (quaternary 3) and output 180° has only slightly higher energy than the 2 → 1 state, such that distinguishing them in a purely statistical manner becomes difficult.

In conclusion, the half adder from this section is worse at forward calculation than the one from the previous section, but it is capable of 1 reverse calculation under ideal circumstances while the one from the previous section can not perform a reverse calculation at all.

## Circuits

We can now compare this half adder with the one from the previous section, in a forward calculation. This is shown in Fig. 35. It is immediately clear that this geometry does not yield correct results. This can be understood from the energy levels in Fig. 34, where it can be seen that the configuration with both islands at  $180^\circ$  has a much lower energy than any other configuration. As such, each half adder will strongly favor this state. Take the  $(0, 0, 0)$  input as an example, which yields the incorrect output  $(0, 1, 0)$  with very high probability. The first half adder takes the input 0, which corresponds to an angle of  $0^\circ$  since the half adder functions with the quaternary convention  $(0, 3, 1, 2)$ . For this input angle, the output with the lowest energy is at  $0^\circ$ , representing 0. As such, the second half adder should get the input  $0 + 2 \cdot 0 = 0$ , once again at  $0^\circ$ . The global incorrect output  $(0, 1, 0)$  indicates that the second half adder prefers to give 1 as output, which is at  $180^\circ$ . If paired with an input at  $180^\circ$ , this will be a very low energy configuration. In order for its input to be at  $180^\circ$ , the first half adder should output 2 or 3. The output 3 corresponds to  $270^\circ$ , which is the second lowest energy for an input at  $0^\circ$ , as is the case here for the first island, as the global input is fixed. The energy difference between an output at  $270^\circ$  or  $0^\circ$  is smaller than the energy that can be gained by allowing the second half adder to be in the  $(180^\circ, 180^\circ)$  state, and therefore the most probable solution is the incorrect one. As such, the high value of  $B_2$  is the limiting factor here.

The main advantage of this type of half adder is thus that it can in theory be used for a

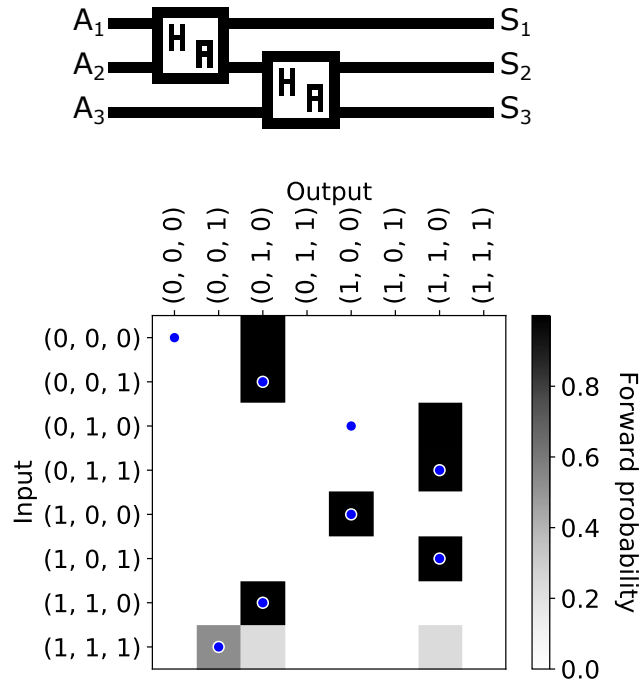


**Figure 35** – **Top:** schematic representation of the logic circuit. **Bottom:** probability of each input/output combination occurring at 298 K, when fixing the input. Hence, each row adds up to a total of 1. Blue dots indicate correct combinations. Inputs are in  $(A_1, A_2, A_3)$  format, outputs  $(S_1, S_2, S_3)$ .

reverse calculation, which the previously discussed type could not. On the other hand, for this geometry the  $(180^\circ, 180^\circ)$  configuration has a very low energy, which causes it to give the wrong solution when chaining multiple of these together, whereas the previous geometry functioned correctly.

As a final remark, for the previous half adders with the fixed island far from the common axis, it was possible to add nanomagnetic chains to the input and output. Unfortunately, because the fixed island is now much closer to the common axis, adding a nanomagnetic chain to the output island has become nontrivial.

## 5.5 Additional considerations

### 5.5.1 Other geometries

As is clear from the geometries that were previously discussed, having two islands in a ‘++’ configuration does not impede the functioning of the half adder. Having more than two islands in line does, however, create a strong preference for the magnetization to align along that axis, which can cause the energy levels to shift significantly away from being balanced. As such, one should refrain from including more than two islands in line with their easy axes in a ‘++’ configuration. Using the balanced ‘ $\times\times$ ’ chain does not prefer any of the four directions, and can thus be useful to include when designing a balanced half adder. The reason the ‘ $\times\times$ ’ configuration was not used here, is because its inherent inversion did not allow it to implement the core functionality of a half adder, since it does not yield exactly two outputs equal to their respective input. However, the ‘ $\times\times$ ’ chain is balanced, so it can definitely be used as a part of an as of yet unknown balanced half adder geometry.

In the previous discussion, the position and saturation magnetization of the fixed island were varied to find their optimal values. Other parameters can also be adjusted, like the angle of this fixed island, or the rotation  $\Phi_i$  of the free islands. Additional islands can also be added to create even more degrees of freedom to improve the balancedness.

In an attempt to find a half adder which is balanced, some more symmetrical geometries were examined in addition to the geometry discussed previously, but unfortunately no well-balanced half adder was found. Some examples of the attempted geometries are shown in Fig. 36. The most promising shape with higher symmetry is shown in the left of the figure. It has four biaxial islands in a rhombic shape, with alternating  $45^\circ$  rotation. This geometry contains a degenerate half adder if one defines the top or bottom island as input and the left or right island as output. Somehow, one should include a fixed island into this geometry to unambiguously define the correct half adder convention, but no sufficiently symmetrical placement was found which does not disturb the energy levels in a disadvantageous manner. The two geometries in the middle of Fig. 36 are examples for which no logically correct quaternary convention exists. The two rightmost geometries in Fig. 36 can function as a half adder, when using the correct quaternary convention.

It can also be advantageous to choose the input and output nanomagnets at the outer edge of the group of nanomagnets that make up the half adder, to easily connect nanomagnetic chains to the input and output. The biaxial nanomagnets comprising these chains should be placed diagonally in an ‘ $\times\times$ ’-pattern, as was already mentioned in the introduction. One must



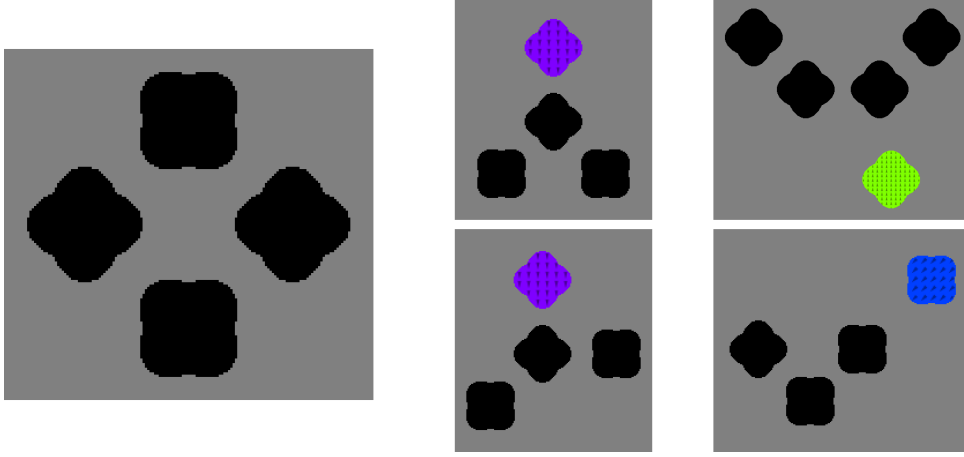


**Figure 36** – A selection of attempted half adder geometries. The colored islands are fixed, with their fixation direction indicated by the color hue and the arrows.

take care, however, that the addition of such a chain does not significantly influence the inner nanomagnets, as this could impede the correct behavior of the logic gate. One way to minimize this interaction, is to define the input and output nanomagnets already at the end of short chains themselves, and including these in the micromagnetic simulation. As such, extending these chains will not significantly influence the inner working of the logic gate.

### 5.5.2 Quaternary convention

#### Decomposition of a biaxial chain into two uniaxial chains

The only quaternary conventions found throughout the different examined geometries are all variations on  $(0, 2, 1, 3)$ , reversed and/or cyclically permuted. A better convention would be  $(0, 1, 3, 2)$ , as the binary representation of this is  $(00, 01, 11, 10)$ , thus flipping exactly one bit at a time. This convention can allow the decomposition of a biaxial chain into two uniaxial chains, by placing two uniaxial chains going away from the output island, one along each hard axis of this island, as shown in Fig. 37. The binary representation of the convention is shown at each corner of the biaxial island, clearly showing that each bit corresponds to a diagonal. Let us take as an example the first bit. When the island has a magnetization angle of  $0^\circ$ , the first bit is 0 and the first uniaxial island from the bottom chain will preferably have a magnetization of  $225^\circ$ . For an input magnetization angle of  $90^\circ$ , the same is true. The second uniaxial island from the bottom chain will then preferably have a magnetization of  $45^\circ$ , corresponding to bit 0, in agreement with the first bit encoded by the magnetization of the biaxial island. For the other two input magnetizations, the first bit is 1, and the lowest energy configuration of the bottom uniaxial chain will have the second uniaxial island at a  $225^\circ$  magnetization angle, corresponding to 1, such that indeed the bottom uniaxial chain extracts the first bit. A similar reasoning can be held for the upper uniaxial chain, which extracts the second bit.

Extracting each individual bit is necessary if one wants to add larger numbers. For example, to add two two-bit numbers, three half adders are needed, the third of which takes the carry from one of the other half adders, and the sum from the other. However, more often than not,

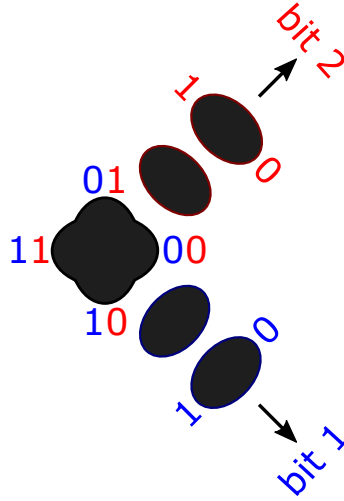


**Figure 37** – Concept for extracting each bit out of a biaxial island with convention (0, 1, 3, 2) (binary (00, 01, 11, 10)).

the geometry of the half adder itself will impose which convention(s) can be used, and one will have to make do with whatever convention the geometry allows. A clean way of magnetically extracting each bit for other conventions was not yet found.

By correctly choosing the angle at which the uniaxial chains leave the biaxial island, it is likely possible to perform this biaxial-to-uniaxial decomposition in a balanced manner, due to the vertical symmetry.

### Different quaternary convention for input and output

In the discussion above, a geometry was only considered as a half adder if it could be defined in such a way that the input and output follow the same quaternary convention. This is a sensible way of assigning conventions, but it is not strictly necessary. Choosing different conventions for the input and output will result in a whole range of possible half adders which were otherwise excluded, and thus increase the chance of finding a balanced half adder, but such a double convention would be very confusing and could lead to a whole range of additional problems. It would be like changing the voltage definition of 0 and 1 in a conventional computer in the middle of a transistor, which would be highly illogical.

A possible exception to this, is the use of a rotated convention for the output as compared to the input. As such, one would only need a bent chain to connect the output to the next half adder, which is certainly more sensible than using vastly different conventions. This might allow for more compact designs, depending on the circuit the half adder is used in. Furthermore, if one were to find two similar geometries, one of which functions with a rotated convention while the other does not, there would be even more freedom to optimize the circuit design using these different variants.

## 6 Conclusion and outlook

In order to gain an understanding of the behavior of a single biaxial island, the energy landscape and thermal switching were examined. A first major remark was that relaxation is necessary for anisotropy to occur. If the island has a perfectly uniform magnetization pointing in-plane in a certain direction, the energy is equal for all these directions. As such, it was necessary to `relax()` the magnetization profile in order to gain useful information about the energy barrier.

It was found that the energy barrier between stable states depends significantly on the roundness  $\rho$  of the biaxial island. As a function of the roundness, different axes take the role of easy axes. For large  $\rho$ , the easy axes are the longest dimensions of the geometry, i.e. horizontal and vertical. For small  $\rho$ , the geometry resembles a ‘plus’-shape, such that each arm of this shape has its own preferred direction. The combination of such vertical and horizontal directions is on average diagonal, with a domain wall in between, hence the average magnetization appears to be diagonal. For this reason, one must take care when using a biaxial island with low roundness, as the magnetization in the different arms can differ significantly. In between these two regimes, there exists a roundness  $\rho \approx 0.49$  for which the energy barrier is very low, with 8 stable states instead of 4, due to the asymmetry in the relaxation of the magnetization.

The thermal switching of different biaxial islands and for different temperatures and damping constants was also examined. No agreement between theoretical and simulated values for the attempt frequency  $f_0$  was found. It was hypothesized that this is because the magnetization of the islands is not perfectly uniform, which is one of the assumptions underlying the theory. The theoretically obtained value  $f_0 = 6 \times 10^5 \text{ s}^{-1}$  is very small compared to the switching frequency, indicating that the theoretical equations are not applicable here. The value obtained through simulations is approximately  $f_0 = 10^{10} \text{ s}^{-1}$ , which is the same order of magnitude as the intrinsic resonance frequency of the magnetization in the local minima of the energy landscape.

A balanced biaxial chain was proposed, which can be used to transmit biaxial information between different logic gates. The easy axes in such a chain are aligned in an ‘ $\times \times$ ’ pattern, such that a rotation or mirror symmetry leaves the system invariant. As a single biaxial island can represent two bits of information, it can be useful to extract these two bits individually. This is for example needed to add two numbers together which consist of more than 1 bit each. A solution was proposed to read the two bits magnetically in the (0, 1, 3, 2) quaternary convention. For other quaternary conventions, it should be possible to read these components out electronically, but an elegant way to do this magnetically has not yet been found. This can be the topic of future work, along with assessing the balancedness of this conversion, and investigating how a biaxial chain can be optimized for signal propagation when bends are required.

The two half adders detailed in Section 5 can both function in a forward calculation. The best of these, i.e. with the fixed island near the free islands’ common axis, has all ground state energies below any of the first excited states, which ensures a correct functioning for a single reverse calculation under ideal circumstances. Unfortunately, in order to chain multiple gates together for a larger reverse calculation, all the ground state energies must be equal, i.e. the gate must be perfectly balanced, which is not the case.

The other type of half adder, with the fixed island relatively far away from the common axis, can not function in reverse at all, as it has excited states with lower energies than some ground

states. This type of half adder does, however, have more spacing in between its energy levels, such that it is better suited for forward calculation. It also has the advantage that it should be relatively straightforward to add some nanomagnetic chains to the input and output, as the fixed island is placed far away from their common axis.

Any half adder following the same concept of using two in-line biaxial islands will never have the ideal quaternary convention  $(0, 1, 3, 2)$ , because a central part of the reasoning behind this concept requires 0 and 1 to have opposite direction. Thus, if one aims to use the biaxial-to-uniaxial chain decomposition proposed for this convention, a different reasoning is needed. The prospect of connecting nanomagnetic chains presents an additional challenge when designing a geometry, as this requires easy access to the input and output islands, without causing a significant disturbance of the energy levels.

In future work, to find a more balanced biaxial half adder, different geometries still have to be examined. One option is to place additional islands near the geometries proposed above, since this increases the degrees of freedom to adjust the energy levels in a way that improves the balancedness. Another option is to consider more symmetrical geometries, like the rhombic layout which was briefly mentioned. This has the advantage that some states will readily have equal energy. The asymmetry in the quaternary truth table might, however, prevent a truly mathematically balanced biaxial half adder using the methods presented in this thesis. Overcoming this challenge remains the topic of future work.

## Bibliography

- [1] B. Cullity and C. Graham. *Introduction to Magnetic Materials*. Wiley, 2009.
- [2] Z. Gu, M. E. Nowakowski, D. B. Carlton, R. Storz, M.-Y. Im, J. Hong, W. Chao, B. Lambson, P. Bennett, M. T. Alam, M. A. Marcus, A. Doran, A. Young, A. Scholl, P. Fischer, and J. Bokor. Sub-nanosecond signal propagation in anisotropy-engineered nanomagnetic logic chains. *Nature Communications*, 6(1):6466, 2015.
- [3] N. D’Souza, J. Atulasimha, and S. Bandyopadhyay. Four-state nanomagnetic logic using multiferroics. *Journal of Physics D: Applied Physics*, 44(26):265001, 2011.
- [4] R. P. Cowburn and M. E. Welland. Room temperature magnetic quantum cellular automata. *Science*, 287(5457):1466–1468, 2000.
- [5] F. L. Traversa and M. Di Ventra. Polynomial-time solution of prime factorization and np-complete problems with digital memcomputing machines. *Chaos: An Interdisciplinary Journal of Nonlinear Science*, 27(2):023107, 2017.
- [6] P. Gypens, J. Leliaert, and B. Van Waeyenberge. Balanced magnetic logic gates in a kagome spin ice. *Physical Review Applied*, 9:034004, 2018.
- [7] P. Gypens, J. Leliaert, M. D. Ventra, B. V. Waeyenberge, and D. Pinna. Nanomagnetic self-organizing logic gates, 2020. arXiv:2012.12721.
- [8] D. Carlton. *Nanomagnetic Logic*. PhD thesis, EECS Department, University of California, Berkeley, 2012.
- [9] J. Leliaert, M. Dvornik, J. Mulkers, J. D. Clercq, M. V. Milošević, and B. V. Waeyenberge. Fast micromagnetic simulations on GPU—recent advances made with mumax<sup>3</sup>. *Journal of Physics D: Applied Physics*, 51(12):123002, 2018.
- [10] W. Heisenberg. Zur theorie des ferromagnetismus. *Zeitschrift für Physik*, 49(9-10):619–636, 1928.
- [11] R. L. Stamps. Mechanisms for exchange bias. *Journal of Physics D: Applied Physics*, 33(23):R247–R268, 2000.
- [12] J. Nogués, J. Sort, V. Langlais, V. Skumryev, S. Suriñach, J. Muñoz, and M. Baró. Exchange bias in nanostructures. *Physics Reports*, 422(3):65 – 117, 2005.
- [13] J. Nogués and I. K. Schuller. Exchange bias. *Journal of Magnetism and Magnetic Materials*, 192(2):203 – 232, 1999.
- [14] A. Imre, G. Csaba, L. Ji, A. Orlov, G. H. Bernstein, and W. Porod. Majority logic gate for magnetic quantum-dot cellular automata. *Science*, 311(5758):205–208, 2006.
- [15] N. D’Souza, A. Biswas, H. Ahmad, M. S. Fashami, M. M. Al-Rashid, V. Sampath, D. Bhattacharya, M. A. Abeed, J. Atulasimha, and S. Bandyopadhyay. Energy-efficient switching

- of nanomagnets for computing: straintronics and other methodologies. *Nanotechnology*, 29(44):442001, 2018.
- [16] N. D’Souza, J. Atulasimha, and S. Bandyopadhyay. An ultrafast image recovery and recognition system implemented with nanomagnets possessing biaxial magnetocrystalline anisotropy. *IEEE Transactions on Nanotechnology*, 11(5):896–901, 2012.
  - [17] J. V. Neumann and A. W. Burks. *Theory of Self-Reproducing Automata*. University of Illinois Press, USA, 1966.
  - [18] P. Arrighi and J. Grattage. A quantum game of life, 2010. arXiv:1010.3120.
  - [19] J. C. Lusth and B. Dixon. A characterization of important algorithms for quantum-dot cellular automata. *Information Sciences*, 113(3):193 – 204, 1999.
  - [20] I. Amlani, A. O. Orlov, G. Toth, G. H. Bernstein, C. S. Lent, and G. L. Snider. Digital logic gate using quantum-dot cellular automata. *Science*, 284(5412):289–291, 1999.
  - [21] A. Aharoni et al. *Introduction to the Theory of Ferromagnetism*, volume 109. Clarendon Press, 2000.
  - [22] F. Strubbe and D. V. Thourhout. *Physics of Advanced Electronic and Photonic Devices*. Ghent University, course for the Master of Science in Engineering Physics 2020-2021.
  - [23] A. Korkin and F. Rosei. *Nanoelectronics and Photonics: From Atoms to Materials, Devices, and Architectures*. Springer Science & Business Media, 2008.
  - [24] E. W. Weisstein. Random walk–1-dimensional. From MathWorld–A Wolfram Web Resource. Available: <https://mathworld.wolfram.com/RandomWalk1-Dimensional.html>, 2000. Visited on 24/12/2020.
  - [25] B. Lambson, Z. Gu, M. Monroe, S. Dhuey, A. Scholl, and J. Bokor. Concave nanomagnets: investigation of anisotropy properties and applications to nanomagnetic logic. *Applied Physics A*, 111(2):413–421, 2013.
  - [26] R. Allenspach. Spin-polarized scanning electron microscopy. *IBM Journal of Research and Development*, 44(4):553–570, 2000.
  - [27] K. Kirk, J. Chapman, and C. Wilkinson. Switching fields and magnetostatic interactions of thin film magnetic nanoelements. *Applied Physics Letters*, 71(4):539–541, 1997.
  - [28] D. W. Abraham, C. C. Williams, and H. Wickramasinghe. Measurement of in-plane magnetization by force microscopy. *Applied Physics Letters*, 53(15):1446–1448, 1988.
  - [29] A. Scholl, H. Ohldag, F. Nolting, J. Stöhr, and H. A. Padmore. X-ray photoemission electron microscopy, a tool for the investigation of complex magnetic structures. *Review of Scientific Instruments*, 73(3):1362–1366, 2002.
  - [30] R. Cowburn, D. Koltsov, A. Adeyeye, and M. Welland. Probing submicron nanomagnets by magneto-optics. *Applied Physics Letters*, 73:3947–3949, 1998.

- [31] P. Fischer. Magnetic soft x-ray transmission microscopy. *Current Opinion in Solid State and Materials Science*, 7(2):173–179, 2003.
- [32] M. Faraday, J. Kerr, and P. Zeeman. *The Effects of a Magnetic Field on Radiation: Memoirs by Faraday, Kerr, and Zeeman*, volume 8. American Book Company, 1900.
- [33] S. Das, A. Zaig, M. Schultz, and L. Klein. Stabilization of exponential number of discrete remanent states with localized spin–orbit torques. *Applied Physics Letters*, 116(26):262405, 2020.
- [34] B. Liu, L. Cai, J. Zhu, Q. Kang, M. Zhang, and X. Chen. On-chip readout circuit for nanomagnetic logic. *IET Circuits, Devices & Systems*, 8(1):65–72, 2014.
- [35] C. Abert and M. Hinze. *Discrete Mathematical Concepts in Micromagnetic Computations*. PhD thesis, University of Hamburg, 2013.
- [36] T. L. Gilbert. *Formulation, Foundations and Applications of the Phenomenological Theory of Ferromagnetism*. PhD thesis, Illinois Institute of Technology, 1956.
- [37] G. S. Abo, Y. Hong, J. Park, J. Lee, W. Lee, and B. Choi. Definition of magnetic exchange length. *IEEE Transactions on Magnetics*, 49(8):4937–4939, 2013.
- [38] H. Kronmüller. Mikromagnetische berechnung der magnetisierung in der umgebung unmagnetischer einschüsse in ferromagnetika. *Zeitschrift für Physik*, 168(5):478–494, 1962.
- [39] A. Vansteenkiste, J. Leliaert, M. Dvornik, M. Helsen, F. Garcia-Sanchez, and B. Van Waeyenberge. The design and verification of Mumax3. *AIP Advances*, 4(10):107133, 2014.
- [40] T. Moriya. Anisotropic Superexchange Interaction and Weak Ferromagnetism. *Physical Review*, 120:91–98, 1960.
- [41] N. Nagaosa and Y. Tokura. Topological properties and dynamics of magnetic skyrmions. *Nature Nanotechnology*, 8(12):899–911, 2013.
- [42] L. Landau and E. Lifshitz. Theory of the dispersion of magnetic permeability in ferromagnetic bodies. *Physikalische Zeitschrift Sowjetunion*, 8:153, 1935.
- [43] J. Leliaert. *Magnetic disorder and thermal fluctuations in domain wall motion and nanoparticle dynamics*. PhD thesis, Ghent University, 2016.
- [44] W. F. Brown. Thermal fluctuations of a single-domain particle. *Physical Review*, 130:1677–1686, 1963.
- [45] T. L. Gilbert. A lagrangian formulation of the gyromagnetic equation of the magnetization field. *Physical Review D*, 100:1243, 1955.
- [46] J. Leliaert, J. Mulkers, J. De Clercq, A. Coene, M. Dvornik, and B. Van Waeyenberge. Adaptively time stepping the stochastic landau-lifshitz-gilbert equation at nonzero temperature: Implementation and validation in mumax<sup>3</sup>. *AIP Advances*, 7(12):125010, 2017.

- [47] N. Bode, L. Arrachea, G. S. Lozano, T. S. Nunner, and F. Von Oppen. Current-induced switching in transport through anisotropic magnetic molecules. *Physical Review B*, 85(11):115440, 2012.
- [48] S. Zhang and Z. Li. Roles of nonequilibrium conduction electrons on the magnetization dynamics of ferromagnets. *Physical Review Letters*, 93:127204, 2004.
- [49] L. Lopez-Diaz, D. Aurelio, L. Torres, E. Martinez, M. A. Hernandez-Lopez, J. Gomez, O. Alejos, M. Carpentieri, G. Finocchio, and G. Consolo. Micromagnetic simulations using graphics processing units. *Journal of Physics D: Applied Physics*, 45(32):323001, 2012.
- [50] A. Lyberatos, D. V. Berkov, and R. W. Chantrell. A method for the numerical simulation of the thermal magnetization fluctuations in micromagnetics. *Journal of Physics: Condensed Matter*, 5(47):8911–8920, 1993.
- [51] N. Kani, A. Naeemi, and S. Rakheja. Non-monotonic probability of thermal reversal in thin-film biaxial nanomagnets with small energy barriers. *AIP Advances*, 7(5):056006, 2017.
- [52] I. Mayergoyz, G. Bertotti, and C. Serpico. Magnetization dynamics driven by a jump-noise process. *Physical Review B*, 83, 2011.
- [53] A. Lee, Z. Liu, G. Bertotti, C. Serpico, and I. Mayergoyz. Analysis of random magnetization switching using monte carlo simulations. *Physica B: Condensed Matter*, 435:100 – 104, 2014. 9th International Symposium on Hysteresis Modeling and Micromagnetics (HMM 2013).
- [54] L. Breth, D. Suess, C. Vogler, B. Bergmair, M. Fuger, R. Heer, and H. Brueckl. Thermal switching field distribution of a single domain particle for field-dependent attempt frequency. *Journal of Applied Physics*, 112(2):023903, 2012.
- [55] B. Ouari and Y. P. Kalmykov. Dynamics of the magnetization of single domain particles having triaxial anisotropy subjected to a uniform dc magnetic field. *Journal of Applied Physics*, 100(12):123912, 2006.
- [56] D. Vokoun, M. Beleggia, L. Heller, and P. Šittner. Magnetostatic interactions and forces between cylindrical permanent magnets. *Journal of Magnetism and Magnetic Materials*, 321(22):3758–3763, 2009.





# Biaxial nanomagnets as building block for balanced half-adders

Jonathan Maes

Student number: 01605865

Supervisors: Prof. dr. Bartel Van Waeyenberge, Dr. Jonathan Leliaert  
Counsellors: Pieter Gypens, Dr. Jonathan Leliaert

Master's dissertation submitted in order to obtain the academic degree of  
Master of Science in Engineering Physics

Academic year 2020-2021